Fall 2010

Aerosol extinction measurements with a new multipass aerosol differential optical absorption spectrometer (A-DOAS): Laboratory validation and initial ambient measurements

Ryan T. Chartier
University of New Hampshire, Durham

AEROSOL EXTINCTION MEASUREMENTS WITH A NEW MULTIPASS AEROSOL
DIFFERENTIAL OPTICAL ABSORPTION SPECTROMETER (A-DOAS):
LABORATORY VALIDATION AND INITIAL AMBIENT MEASUREMENTS

BY

RYAN T. CHARTIER
Bachelor of Arts, Assumption College, 2004

THESIS

Submitted to the University of New Hampshire
in Partial Fulfillment of
the Requirements for the Degree of

Master of Science
in
Chemistry

September, 2010

UMI Number: 1486978

UMI®

Dissertation Publishing
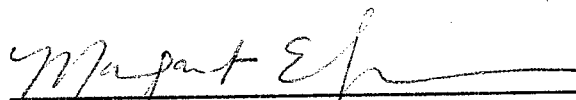
ProQuest®

This thesis has been examined and approved.
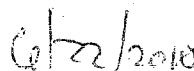
Thesis Director, Dr. Margaret E. Greenslade,
Assistant Professor of Chemistry

Dr. Christopher F. Bauer,
Professor of Chemistry

Dr. Howard R. Mayne,
Professor of Chemistry

6/22/2010

Date

ACKNOWLEDGEMENTS

TABLE OF CONTENTS

CHAPTER   PAGE

LIST OF TABLES

LIST OF FIGURES

ABSTRACT

AEROSOL EXTINCTION MEASUREMENTS WITH A NEW MULTIPASS AEROSOL
DIFFERENTIAL OPTICAL ABSORPTION SPECTROMETER (A-DOAS):
LABORATORY VALIDATION AND INITIAL AMBIENT MEASUREMENTS

by

Ryan T. Chartier

University of New Hampshire, September, 2010

Atmospheric aerosols directly affect climate by scattering and absorbing incident solar radiation. The magnitude of the impact is dependent upon the wavelength of incoming light, but is typically approximated near 550 nm. As a result, climate models can have large uncertainties for aerosol contributions when considering the solar spectrum. An aerosol differential optical absorption spectrometer (A-DOAS) has been developed to address to measure aerosol extinction from mid-ultraviolet to near infrared. The instrument consists of a closed UV-Vis spectrometer coupled to a White-type multi-pass gas cell with an adjustable path length of up to 20 meters. Laboratory extinction measurements of polystyrene latex spheres, nigrosin dye, and carbon black are compared with theory to validate the new instrument. Further, the lower limit of detection for the A-DOAS is shown to be less than 1×10^{-7} cm^{-1}. Finally, ambient aerosols under a variety of conditions were monitored and future work suggestions are made.

CHAPTER 1

INTRODUCTION TO ATMOSPHERIC AEROSOLS

Aerosol Background

The Intergovernmental Panel on Climate Change (IPCC) has deemed it "exceptionally unlikely" that recent changes in natural processes (e.g. solar irradiance + volcanic aerosol) have had a comparable warming effect on the climate to that of human activities (IPCC, 2007). Anthropogenic factors such as greenhouse gases and aerosols contribute to climate change by influencing the radiative forcing (Wm^{-2}) of the earth-atmosphere system. These perturbations alter the energy balance between incoming solar radiation and outgoing infrared radiation, leading to heating or cooling of the atmosphere. Positive radiative forcing values correspond to heating of the atmosphere, while negative radiative forcing is associated with cooling.

The effects that greenhouse gases, such as carbon dioxide and methane, have on the climate are well characterized. These gases are well-mixed and remain in the atmosphere for a long time, leading to similar worldwide atmospheric concentrations. This, along with decades of research to characterize the properties of these gases, makes predicting their overall effect on the climate fairly straightforward, with low uncertainty (IPCC 2007). Aerosols do not remain in the atmosphere as long as greenhouse gases, but are capable of having considerable impact on climate change (Twomey 1991; Charlson, Schwartz et al. 1992; Horvath 1993). The concentration and chemical/physical properties of aerosols vary widely over the globe. This contributes to large uncertainties when trying to quantify the effect aerosols have on global climate.

1

Aerosols are liquid or solid particles suspended in a gas, and when present in the atmosphere they directly and indirectly affect the radiative balance of the earth-atmosphere system. The direct forcing effect of aerosols is associated with scattering and absorption of electromagnetic radiation, while indirect forcing is due to changes in cloud number and albedo resulting from the presence of aerosols (Kuang and Yung 2000). Indirect forcing is not the focus of this work. The chemical and physical properties of an aerosol determine how it interacts with light, and the term "optical properties" is used throughout this work as a generic term to describe the particle-light interaction of an aerosol. The majority of solar radiation reaching the lower atmosphere falls within the wavelength range of 300-1400 nm. These wavelengths efficiently interact with typical aerosol particles that have diameters on the same order. The specifics of this interaction are discussed in greater detail in Chapter 3.

Aerosol Sizes

Aerosols are ubiquitous in the atmosphere and can range in size from approximately 2-3 nm to greater than hundreds of microns. This large variation in size, 5-7 orders of magnitude, makes it convenient for aerosols to be classified into different size categories: coarse mode, fine mode, and various subcategories. In general, particles in the two size modes are created via different processes, which are discussed below. The different sources for coarse and fine mode aerosols lead to different physical and chemical properties, removal processes, and number concentrations. The efficiency of aerosol removal processes is largely size dependent, therefore particular aerosol sizes dominate the physical properties of an aerosol sample. In general, the smallest aerosols are present at the highest concentrations, while the majority of the total aerosol mass, even with lower number concentrations, is due to the largest aerosols (Table 1.1).

Table 1.1. Comparison of the size dependent distribution of the physical properties of an arbitrary theoretical aerosol sample. The smallest aerosols account for the vast majority of particle number. However, the total aerosol mass and surface area are often largely due to the biggest particles. Highlighting is added in each column to emphasize the largest value.

Aerosol Size Classification	Example Diameter in microns (μm)	Estimated Number concentration (particle/cm^3)	Surface Area (μm^2)	Volume (μm^3)	Mass (picograms) assuming ρ = 1.30 g/cm^3
Coarse Mode	5.00	10	785	654	850
Accumulation	0.50	1000	785	6.54	85.0
Aitken	0.05	10000	78.5	0.654	0.850
Nucleation	0.005	100000	7.85	0.00654	0.00850

Coarse mode aerosols are defined as particles with a diameter greater than 2.5 μm. These large particles enter the atmosphere through mechanical processes such as seaspray and wind-blown dust. The majority of aerosol mass in any given atmospheric sample is due to coarse mode particles. However, large particles tend to gravitationally settle quickly (minutes to days), and unless lofted upward by air currents, they will be quickly removed from an air mass before long-range transport can occur. The short lifetime of coarse mode aerosols, relative to smaller particles, will shift the mass distribution peak of an aged air mass to smaller particles sizes.

Fine mode aerosols have a diameter of less than 2.5 μm. Due to inefficient removal processes these aerosols have much longer residence times in the atmosphere (days to weeks) compared with coarse mode particles. Fine mode aerosols account for most of the total aerosol number, surface area, and a large fraction of aerosol mass in the atmosphere (Finlayson-Pitts 2000). The fine mode can be broken down further into three subcategories: nucleation mode, Aitken mode, and accumulation mode.

Nucleation mode consists of the smallest aerosols, with diameters of less than 10 nm. These particles are formed in the atmosphere through gas-to-particle conversion processes, such as appropriately named nucleation events, where gas phase species with low vapor pressures condense to form particles. An example of this phenomenon is the oxidation of sulfur dioxide to sulfuric acid. The low vapor pressure of sulfuric acid

allows it to nucleate by condensing to form new particles at a rate that is proportional to the gas phase concentration (Kulmala, Vehkamäki et al. 2004). However, the details of this process are not fully understood. Nucleation mode aerosols are removed from the atmosphere by coagulation with or condensation onto other existing particles. This results in an aggregate aerosol with a diameter larger than 10 nm, moving these aerosols into larger size classifications such as the Aitken mode.

The Aitken size mode encompasses aerosols with diameters ranging from approximately 10-100 nm. As can be seen in Table 1.1, particles in the nucleation and Aitken mode account for the majority of the total number of aerosols in the atmosphere, but only a small portion of available aerosol surface area and mass. Aerosols in this size range are removed through the same condensation and coagulation processes as nucleation mode aerosols, increasing the diameter to that of accumulation mode aerosols.

Accumulation mode particles range from approximately 100 nm to 2.5 μm. Particles in this size range are not typically emitted directly, but are grown through the processes mentioned previously. Accumulation mode is aptly named because the removal of these aerosols is slow, allowing them to accumulate in the atmosphere. Aerosols in this size range account for a large fraction of the available total aerosol surface area and mass. Wet deposition, such as the scavenging of aerosol by water droplets in clouds or fog, followed by deposition to the earth's surface is a major removal process for accumulation mode particles, but it is not rapid. The growth and removal processes of atmospheric aerosols can be seen in Figure 1.1. The long residence time (days to weeks) of accumulation mode aerosols in the atmosphere allows aging processes to occur, which alter the physical and chemical properties of the particles.

Aerosol oxidation can occur from exposure to oxidants such as ozone and hydroxyl radicals. This will change both the surface chemistry of the aerosol and how it

4

interacts with light. Oxidation can "brown" organic aerosol particles, increasing their ability to absorb UV and visible radiation (Sun, Biedermann et al. 2007). The oxidation of hydrophobic aerosols to hydrophilic aerosols increases the likelihood of surface uptake of water vapor (Kotzick, Panne et al. 1997). This can change both the size and overall chemistry of the particle (Jacob 2000). Ultimately changes in size and chemistry will affect the particle-light interaction (Grieshop, Logue et al. 2009; Jimenez, Canagaratna et al. 2009).
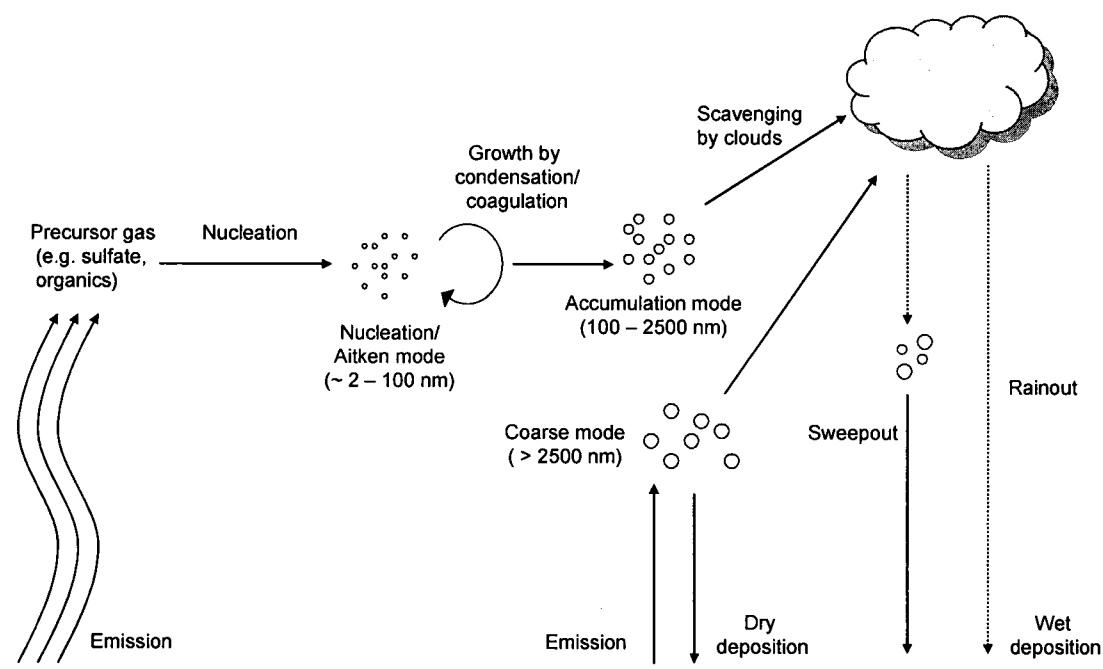
Figure 1.1. This diagram of the atmospheric cycling of aerosols shows the introduction and removal processes for the various aerosol size categories. The smallest particles, nucleation and Aitken mode aerosols, are removed via condensation and coagulation processes, which increase the size of these particles to that of accumulation mode aerosols. Accumulation mode aerosols are removed by cloud scavenging followed by wet deposition to the surface. Coarse mode aerosols are removed by gravitationally settling out of the atmosphere, or by cloud/fog scavenging followed by wet deposition to the surface.

The particle size range that is relevant for the remainder of this work is the fine mode. Aitken and accumulation mode aerosols are the most important when considering particle-light interactions at solar wavelengths, as particles of this size contribute the majority of aerosol surface area and efficiently interact with solar radiation.

Aerosol Sources

Primary aerosols are normally mechanically derived via natural processes, leading to large particles (> 1 μm). Natural primary aerosols mainly consist of wind-generated mineral dust (estimated mass: 1490 Tg/year) (Zender, Bian et al. 2003), and seasalt aerosol which is formed during sea spray and bubble bursting processes (estimated mass: 10100 Tg/year) (Gong, Barrie et al. 2002). Smaller inputs of naturally occurring primary aerosol include volcanic dust (30 Tg/year) and biological material (e.g. pollen, plant and animal material, fungal spores) (Kiehl and Rodhe, 1995). Global emissions of primary biological aerosol particles is uncertain and estimates range from approximately 50 Tg/year (Penner, Hegg et al. 2001) to upwards of 1000 Tg/year (Jaenicke 2005).

Approximately 1-2% (Seinfeld and Pandis, Table 2.20) of primary aerosol emissions are associated with anthropogenic sources. These sources include black carbon emissions during combustion, dust resulting from industrial processes, and primary organic aerosol emissions from domestic and agricultural fires. These anthropogenic emissions (~ 200 Tg/year) are small compared to natural primary emissions, but can significantly affect local and regional air quality and climate (Seinfeld and Pandis 1998).

Secondary aerosols are particles that are not directly emitted, but formed when gas phase species react and condense to form particles in the atmosphere. An important and more specific category is secondary organic aerosol (SOA) (Kanakidou, Seinfeld et al. 2005). Atmospheric oxidation of organic compounds by ozone, hydroxyl radical, nitrate radical, and other oxidants can decrease the vapor pressure of these gas phase species allowing them condense into the particle phase (Sempere and Kawamura 2003; Rompp, Winterhalter et al. 2006).

Aerosol Interaction with Radiation

The magnitude and sign of climate forcing by aerosols is controlled by the scattering and absorption of light by the aerosol, as well as the underlying surface albedo, which is depicted in Figure 1.2. The regional and global quantification of these forcing effects is more complex than that of greenhouse gases. The high spatial and temporal variation of aerosol emission sources results in complex aging and mixing processes that are difficult to quantify globally (Turpin, Saxena et al. 2000). Greenhouse gases are long-lived and well mixed by comparison.
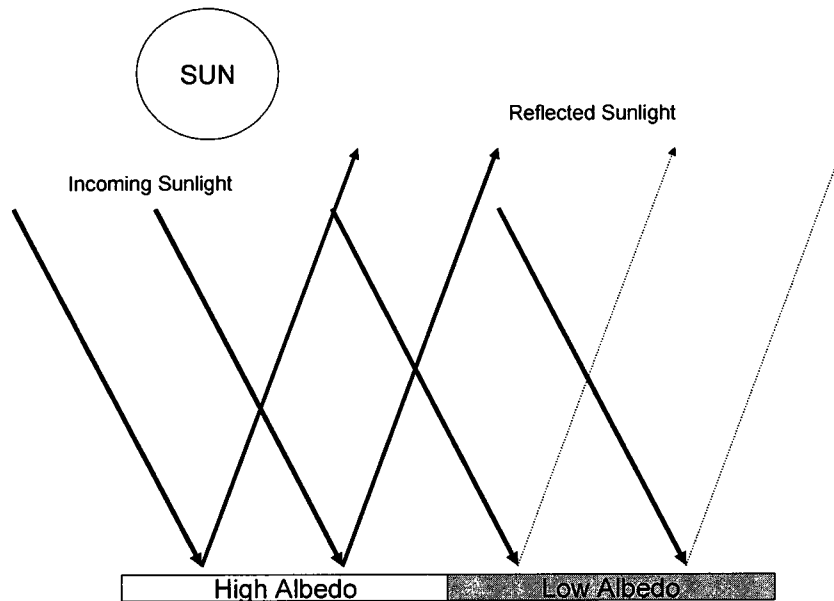
Figure 1.2. Surface albedo is a measure of the reflectivity of the earth's surface. It is defined by the total intensity of reflected light divided by the intensity of the incident light. Highly reflective surfaces, such as snow, have a high albedo, while a dark surface, such as bare soil, will have a low albedo.

Aerosols scatter incoming light in all directions (b_{scatt}, where b is in units of inverse length). This occurs when an aerosol interacts with light and changes the direction of propagation of the beam, via the geometrical optics processes shown in Figure 1.3. Incoming solar radiation is partially scattered back into space. This reduces the intensity of light that is available to be converted to heat by absorption processes at the earth's surface, and often leads to negative climate forcing. Scattering is the reason

7

the sand at the beach is much cooler on a cloudy day; the sunlight is scattered back into

space by cloud droplets before it can be absorbed by the sand and converted to heat.
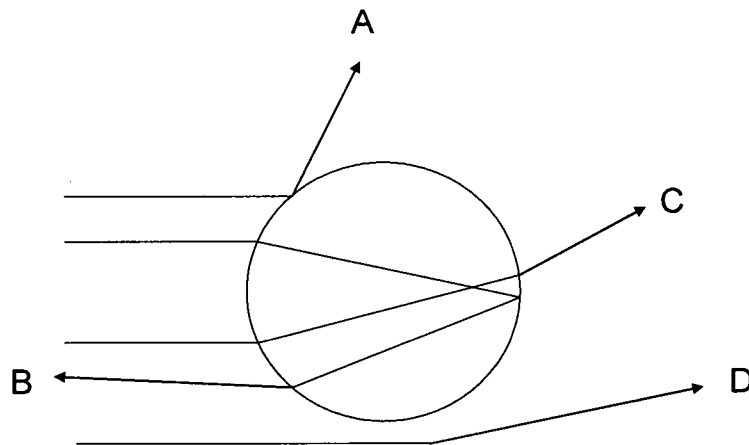
Figure 1.3. The direction of incident light can be altered through various interactions with an aerosol particle. Shown here are (A) reflection, (B) refraction and internal reflection, (C) internal refraction, and (D) diffraction. These interactions lead to the incident light being scattered in all directions by a spherical aerosol particle. This figure was adapted from the Bohren and Huffman (1983) Figure 7.1.

Some aerosols can absorb incoming light (b_{abs}) as well as scatter it. The

absorbed radiation is internally converted to thermal energy. Similar to greenhouse

gases, an aerosol that absorbs light re-radiates the thermal energy in all directions,

warming the atmosphere around it, as shown in Figure 1.4. While the absorption of

solar radiation by aerosols can lead to cooling at ground level due to decreased

intensity, the resulting atmospheric heating around the aerosol layer can alter convection

patterns, and can affect atmospheric processes (Mallet, Tulet et al. 2009; Jayaraman,

Ratnam et al. 2010). The inclusion of absorbing aerosols into cloud droplets can change

cloud properties by locally heating the atmosphere and affecting condensation rates

(Nenes, Conant et al. 2002; Fan, Zhang et al. 2008). Likewise, absorbing aerosols

mixed with snow or ice can increase the rate of melting by converting incoming solar

radiation to heat. This reduces snow/ice cover, which decreases the surface albedo and

therefore complicates the radiative balance of the earth-atmosphere system

(Ramanathan and Carmichael 2008).
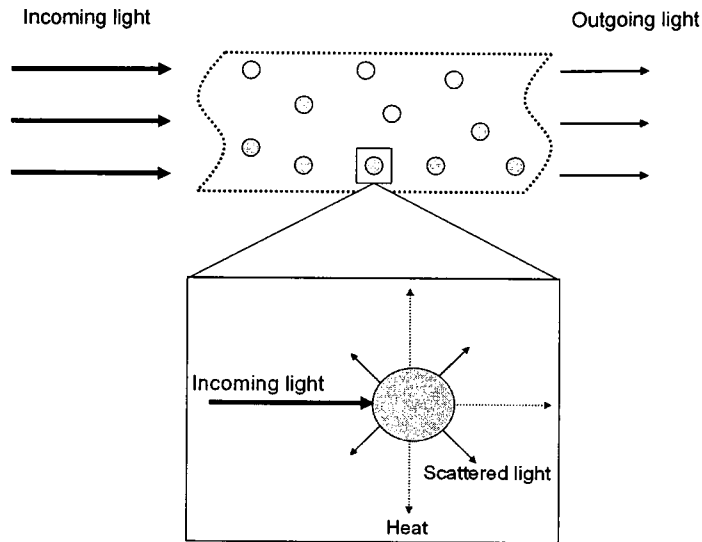
Figure 1.4. The intensity of incident light in the forward direction is reduced as it propagates through air containing aerosols. The reduction in light intensity is due to the combined effect of scattering and absorption. The incoming light interacts with a particle (inset) and some is scattered in all directions. It is also possible for some of the light to be absorbed and re-emitted as heat, again in all directions.

A parameter used to determine aerosol climate forcing is single scattering albedo (SSA). SSA is the ratio between b_{scatt} and the total attenuation of the incident light (extinction, $b_{ext} = b_{scatt} + b_{abs}$). As aerosol absorption increases, SSA values decrease from purely scattering (SSA=1) to a critical point of approximately 0.85 - 0.91; at this critical point, climate forcing can change from cooling to heating (Haywood and Shine 1995; Hansen, Sato et al. 1997). However, the critical point changes with the underlying surface albedo. An absorbing aerosol will have a greater positive forcing effect when over a high albedo surface such as ice or snow. The light absorbed and reradiated as heat would have been reflected back into space had it reached the surface.

The Bouguer-Lambert law is commonly used to experimentally determine the extinction of an aerosol sample and is given by

$$I = I_0 e^{-\beta_{ext} L} \qquad (1.1)$$

where I_0 is the measured intensity of the incident light, I is the measured intensity of light after it passes through a sample, L is the sample path length, and β_{ext} is the extinction of

the sample in units of length^{-1}. Aerosol extinction can also be given as b_{ext}, b_{ep}, σ_{ext}, or σ_{ep}, but all have the same meaning and identical units. These symbols are also used for scattering and absorption, but with their respective subscripts. To avoid confusion, experimental extinction is given as Ext (cm^{-1}) in this work. Gas phase absorption cross sections are commonly given as σ with units of area/molecule, and this convention will be followed in this work. However, aerosol extinction cross sections are commonly given as both σ_{ext} and C_{ext} with units of area/particle. To avoid possible confusion between σ_{ext} (length^{-1}) and σ_{ext} (area/particle), C_{ext} is used to denote aerosol extinction cross section in this work.

Aerosol Optical Property Measurement Techniques

The most common technique used to measure aerosol scattering is a nephelometer. Integrating nephelometers are used to measure the scattering intensity at different angles from an aerosol sample. Therefore, if an aerosol does not absorb light the sum of the scattering over all angles corresponds to the total extinction of the aerosol. The instrumental design of a typical nephelometer allows for measurement of scattering intensity from approximately 7-173 degrees. Near-backward or near-forward scattering measurements (0-7° and 173-180°) cannot be made without blocking the light source or the detector. This is overcome by using truncation error corrections to predict the scattering at these shallow angles. This method has been shown to work well for accumulation mode particles (< 10% uncertainty), but rapidly deteriorates for coarse mode particles (20-50% uncertainty) (Anderson, Covert et al. 1996). Recently, diffraction theory has been used to calculate the truncation error for large non-absorbing particles, and has been shown to be accurate (Moosmuller and Arnott 2003). However, as the absorption of particles increases, these corrections become less effective (Massoli, Murphy et al. 2009).

Aerosol absorption is difficult to quantify in ambient samples due to its small magnitude in comparison to scattering. The difficulty in isolating the absorption from the scattering component of total extinction makes past and current techniques somewhat inaccurate. One method used to quantify absorption is the difference method, where both scattering and extinction are measured and the difference between these two numbers is attributed to absorption. This method uses the difference between two large numbers to calculate a small number ($b_{ext} - b_{scatt} = b_{abs}$), therefore any uncertainty in scattering or extinction is magnified in the calculated absorption. The magnitude of the uncertainty of this method can be larger than the magnitude of absorption. Scattering measurements are typically made with a nephelometer. New extinction measurement techniques, such as cavity ring down aerosol extinction spectroscopy (CRD-AES), have significantly reduced the uncertainty associated with measuring extinction, thus improving the overall validity of the difference calculations (Pettersson, Lovejoy et al. 2004).

Particle soot absorption photometers (PSAP) have been used to quantify absorption. This is a filter based technique where ambient aerosols are deposited onto a filter and Beer's Law is used to calculate absorption due to the aerosol sample. This technique is simple and can be automatically programmed for remote operation. However, this system exhibits a response to non-absorbing aerosols, adsorbed gas phase species, and changes in relative humidity, leading to the overestimation of absorption by approximately 20-30% (Bond, Anderson et al. 1999; Cappa, Lack et al. 2008).

Recently, photoacoustic absorption spectroscopy (PAS) has been used to accurately quantify both gas phase and aerosol absorption (Bennett and Forman 1977; Moosmuller, Arnott et al. 1998; Arnott, Moosmuller et al. 1999; Arnott, Moosmuller et al. 2003). This technique measures the sound waves produced by aerosols following light

absorption. PAS directly measures aerosol absorption and avoids many of the issues previously mentioned for PSAP and difference method measurements (Moosmuller, Chakrabarty et al. 2009). However, this technique can only be used to measure dry aerosols. The heating and cooling of humidified aerosols when exposed to the laser can cause the evaporation of water from the particle, which can give an erroneous photoacoustic signal (Murphy 2009).

Aerosol extinction has been quantified with a number of techniques, including CRD-AES, which was briefly mentioned above (Smith and Atkinson 2001; Strawa, Castaneda et al. 2003; Sheridan, Arnott et al. 2005; Baynard, Lovejoy et al. 2007; Slowik, Cross et al. 2007; Dinar, Riziq et al. 2008). This technique uses a monochromatic laser light source and highly reflective mirrors (R > 99.997%) to achieve long sample path lengths (on the order of km) in a closed system. This allows the determination of optical properties of lab generated particles with extinction detection limits as low as approximately 10^{-9} cm^{-1} (Pettersson, Lovejoy et al. 2004). In contrast, ambient aerosol extinction measurements in polluted urban environments commonly yield values higher than 10^{-5} cm^{-1} (Andreae, Schmid et al. 2008).

Differential optical absorption spectroscopy (DOAS) has also been used to measure aerosol extinction (Notholt, Hjorth et al. 1992; McMurry 2000; Honninger, von Friedeburg et al. 2004; Volkamer, Molina et al. 2005; Takashima, Irie et al. 2009; Si, Xie et al. 2010). This technique uses a broadband light source and long path lengths to determine the differential absorption spectra of a sample. It is most commonly used to determine the concentration of trace gas species in the atmosphere, but it has also been used to measure aerosol extinction. With its long path length a DOAS system can yield low detection limits. However, these instruments are usually limited to measuring the optical properties of a bulk aerosol sample (Platt and Stutz 2008) and therefore cannot

be used to differentiate between aerosol type and the specific optical properties of that aerosol.

A limited number of laboratory instruments similar to DOAS are capable of measuring aerosol extinction over the majority of the solar spectrum, at some atmospherically relevant particle concentrations. (Virkkula, Ahlquist et al. 2005) used an optical extinction cell (OES) to measure extinction at three wavelengths (467, 530, 660 nm). The sample path length obtained with the OES was 330.2 cm, which is makes this instrument sensitive enough to only measure very concentrated aerosol samples. This instrument does not provide measurements of extinction in the near UV wavelengths (300-400 nm), which are of particular importance when measuring the extinction of certain types of aerosols (Dinar, Riziq et al. 2008; Moosmuller, Chakrabarty et al. 2009; Yang, Howell et al. 2009; Park, Kim et al. 2010).

(Mogili, Yang et al. 2007) used an Ocean Optics UV-Vis spectrometer coupled to an environmental chamber to measure the extinction of mineral dust over the wavelength range from 250-800 nm. The incident light was transmitted through quartz windows, which provided a sample path length of 66.5 ± 0.5 cm. This short path length is limited to studies with very high particle concentrations.

(Schnaiter, Horvath et al. 2003; Schnaiter, Schmid et al. 2005) used a dual-beam long path extinction spectrometer (LOPES) to measure aerosol extinction from 200-1100 nm with a 2.5 nm spectral resolution. The LOPES system consists of a long cell (5 m) with a corner cube mirror at one end, providing a path length that is twice the length of the cell. The 10 m LOPES instrument is able to accurately measure extinction over the entire wavelength range with a lower detection limit of 2.0×10^{-7} cm^{-1}, which is adequate for measuring extinction in polluted urban areas where total extinction can reach levels of upwards of 1.0×10^{-5} cm^{-1} (Andreae, Schmid et al. 2008).

Global climate models (GCMs) are often used to predict the impact atmospheric species will have on the earth's climate. GCMs must often use estimates of the optical properties associated with an aerosol sample. Bulk measurements cannot always accurately assign optical properties to individual aerosol types in a mixed aerosol sample, while single wavelength measurements do not measure the wavelength dependence of particle-light interactions. This work examines the extinction of laboratory generated aerosols at wavelengths corresponding to the solar spectrum. The control afforded by laboratory research allows measured optical properties to be attributed to aerosols of known composition. To achieve this goal, an instrument with a broadband spectrophotometer and closed sampling system were designed in consultation with a commercial vendor, and will be discussed in detail in Chapter 2 along with operating instructions. The results from experiments using highly scattering and highly absorbing aerosol proxies will be discussed in Chapters 3 and 4 respectively, while Chapter 5 will focus on the results of ambient air measurements and suggestions for future work.

CHAPTER 2

AEROSOL DIFFERENTIAL OPTICAL ABSORPTION SPECTROMETER
(A-DOAS)

Absorption Spectroscopy

For over a century, gas phase absorption spectroscopy has been used to quantify reactive atmospheric trace gases in-situ. In 1879, Marie Cornu measured the solar spectrum by breaking sunlight down into its component wavelengths, and observed a sharp decrease in intensity in the ultraviolet region (Platt and Stutz 2008). Hartley 1880, later determined that the absorption of UV light was due to electronic transitions of atmospheric ozone (Platt and Stutz 2008). When a given molecule absorbs photons at certain wavelengths it can undergo rotational (A), vibrational (B), and/or electronic transitions (C), specific to that molecule (see Figure 2.1).

Rotational energy level transitions, shown with arrows in Figure 2.1 (A), correspond to the absorption of microwave radiation (on the order of 10 J/mol). Rotational spectroscopy is widely used to determine bond lengths within a gas phase molecule with a dipole moment. There are many rotational energy states within a single vibrational energy state, but the selection rules state that the molecule can only be excited to the J+1 state unless an electronic or vibrational transition occurs at the same time. If a concurrent vibrational transition occurs the rotational selection rules are $\Delta J = \pm 1$. A transition of $\Delta J = 0$ is possible when an electronic transition occurs.
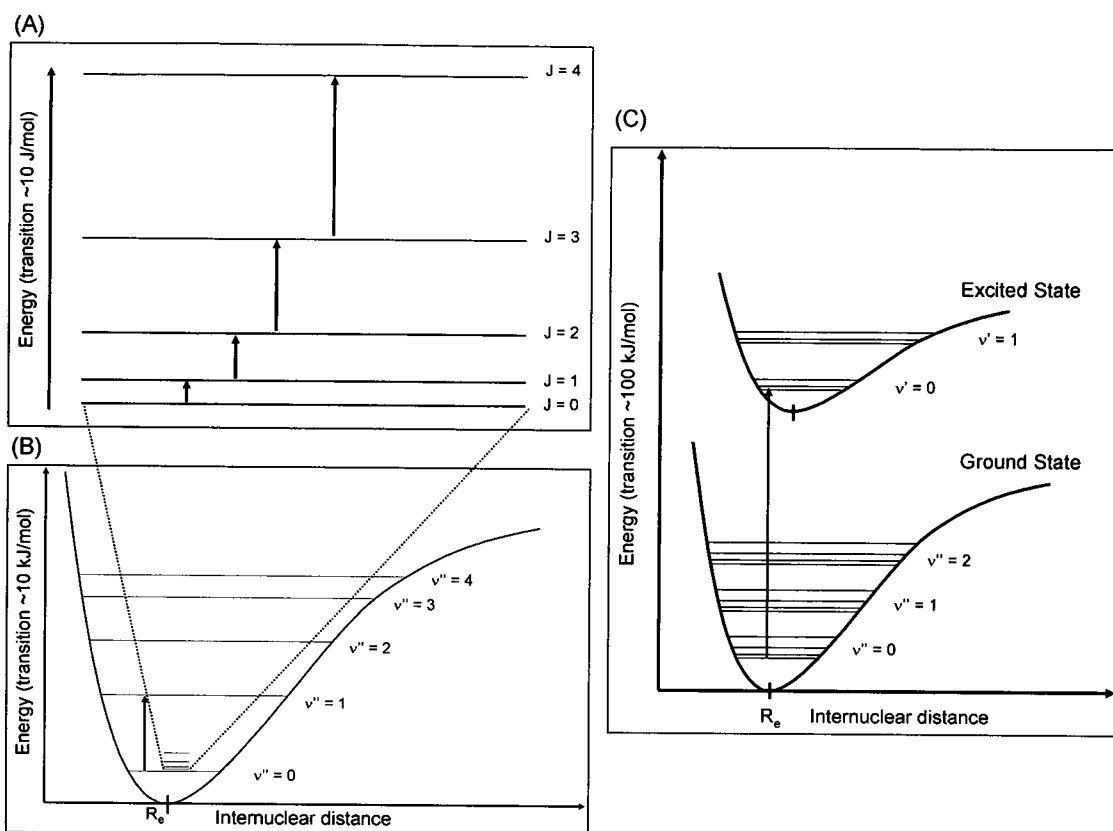
Figure 2.1. (A) Absorption of microwave radiation can excite a molecule into a higher rotational energy level (J). (B) Certain molecules absorb infrared radiation, which can excite the molecule into a higher vibrational state (v). Electronic transitions (C) occur when a molecule absorbs a photon of energy corresponding to UV and visible radiation. Please note the difference in energies on the y-axes. The dotted lines in (B) indicate that (A) is an expansion. The rotational energy levels in (B) and vibrational energy levels in (C) are not drawn to scale for clarity. Figures adapted from Platt and Stutz 2008, and Finlayson-Pitts and Pitts 1999.

Vibrational transitions occur at energies corresponding to infrared wavelengths (~0.5 - 170 kJ/mol). However, the useful wavelength range for vibrational spectroscopic measurements is typically confined to 2.5-16 μm (~7-50 kJ/mol) for common transitions, which encompass the bending and stretching vibrational frequencies of most covalent bonds of interest. This technique provides information about the specific functional groups associated with a molecule by measuring the energy of the vibrational transitions (Figure 2.1 (B)) of the molecule. Covalent bonds with a dipole moment that varies over time can absorb infrared radiation, specifically radiation that oscillates at the same frequency as dipole. Different types of bonds, and the motions of these bonds, can be

16

identified by the energy of infrared radiation they absorb. Therefore, the infrared spectrum of a molecule acts as a fingerprint identifying the specific functional groups contained in that molecule. At room temperature, this transition is dominated by the excitation of molecules from their vibrational ground state (v=0) to the first excited state (v=1). The selection rule for vibrational energy level transitions is $\Delta v = \pm 1$.

The energy of the radiation used in both rotational and vibrational spectroscopy is less than the energy of light used in this work. Molecules can undergo both rotational and vibrational transitions in conjunction with the electronic transitions accessed. Rotational transitions cannot be observed at the resolution of the instruments used in this work, and will not be discussed in further detail. The absorption of higher energy photons at UV-Vis wavelengths ($\sim$190 – 700 nm, $\sim$170 – 630 kJ/mol), which correspond to the majority of incoming solar radiation and are most applicable to this work, can induce vibrational as well as electronic transitions. There are no selection rules for vibrational energy level transitions when moving from one electronic state to another, which can lead to discrete lines in the UV-Vis spectrum of a molecule. For example, the sharp peaks in the spectra of SO_2 shown in Figure 2.2 correspond to the absorption of photons to promote the molecule from its ground electronic state to an excited state, including specific vibrational transitions. It is the vibrational steps on top of the electronic transitions that cause the sharp features in Figure 2.2.
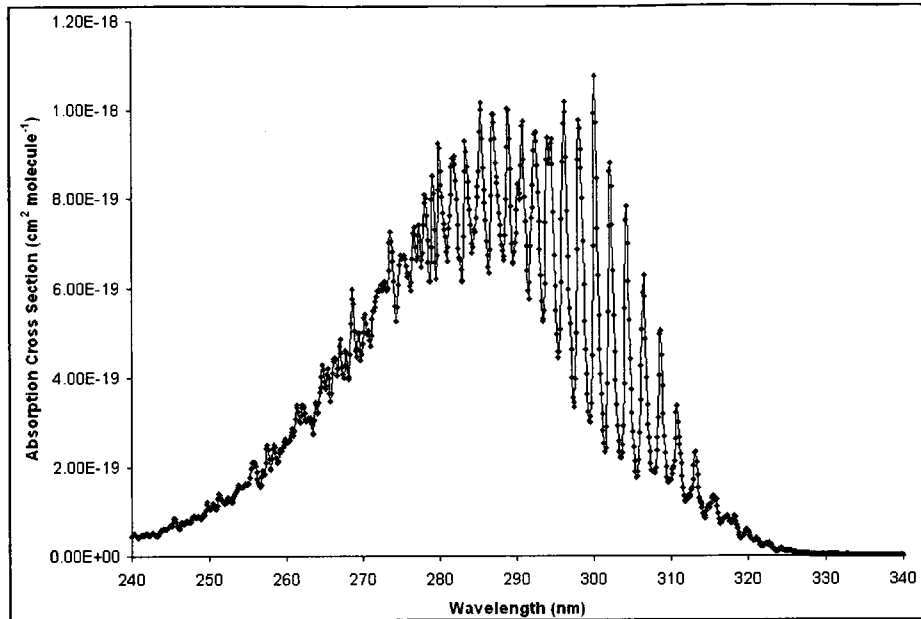
Figure 2.2. The UV-Vis spectrum of SO_2 is shown (Bogumil, Orphal et al. 2003). The sharp peaks are due to the absorption of photons with energies that correspond to an electronic transition from the ground state to an excited state, coupled with particular vibrational transitions (e.g. $v'' = 0 \rightarrow v' = 0$, $v'' = 0 \rightarrow v' = 1$...).

The intensity difference of light before and after interacting with a gas sample can be attributed to absorption of photons by the gas phase species. The concentration of a specific gas can be determined via the Beer-Lambert law (Equation 2.1), as the absorption of photons is proportional to the concentration and the strength of the absorption at that wavelength for that species,

$$A = \ln\left(\frac{I}{I_0}\right) = \sigma N L \qquad (2.1)$$

where A is absorbance, I_0 is the intensity in the absence of species of interest, I is the measured light intensity after traveling through the sample, σ is the absorption cross section (cm^2/molecule), N is the concentration (molecules/cm^3), and L is the path length. An example of this would be light passing through a column of air containing SO_2. The concentration of SO_2 in the sample column could be calculated using σ, which is given in Figure 2.2, the path length of light through the sample, and measurement of the light

18

intensity (at a wavelength SO_2 absorbs) at the light source and after the light travels through the sample.

<u>Differential Optical Absorption Spectroscopy</u>

As broadband light passes through the atmosphere its intensity is reduced by a variety of extinction processes, such as scattering by gases and aerosols, as well as absorption by trace gas species as was just discussed, and absorption by aerosols. Atmospheric scattering is dominated by Rayleigh and Mie scattering. Rayleigh scattering is the process by which gas molecules scatter light, and this has a strong wavelength dependence. Gas molecules in the atmosphere efficiently scatter shorter wavelengths of light (blue and UV light) in all directions, resulting in the appearance of a blue sky when the sun is overhead. Mie scattering defines the scattering properties of larger spherical particles, which are made up of many molecules in the solid or liquid phase. Mie scattering does not have strong wavelength dependence, and is the reason clouds appear white; all wavelengths are scattered equally by the cloud water droplets. Light scattering by atmospheric particles will be discussed in more detail in Chapter 3.

To determine the concentration of one particular gas phase species, all other factors affecting the light intensity have to be quantified. This is not practical for an atmospheric sample. Instead, the differential optical absorption spectroscopy (DOAS) technique utilizes the narrow absorption band structures of trace gases, such as the sharp peaks in the SO_2 spectrum, to measure their individual concentrations. The narrowband structures are separated from interpolated broad absorption structures, allowing the determination of differential absorption, denoted as D, using Equation 2.2. An example of this method is shown in Figure 2.3. The differential absorption can be used to calculate concentration with Equation 2: (Platt and Hausmann 1994; Smith, Plane et al. 1995),

$$D = \ln\left(\frac{I_0^{x'}}{I_x}\right) = \sigma' NL \qquad (2.2)$$

where $I_0^{x'}$ is the interpolated intensity without species X present, and I_x is the measured

intensity of the sample including species X, σ' is the cross section of the differential

optical absorption band, N is the concentration of X, and L is the path length through the

sample (Platt and Stutz, 2008). Figure 2.3 shows how the interpolated incident intensity

is used instead of the actual incident intensity. Different gas species can absorb at the

same wavelengths, so calibration spectra are needed for the species of interest. For

example, the differential spectrum of SO_2, such as in Figure 2.2, at a known

concentration is needed to determine intensity of the fine absorption features at specific

wavelengths. Computer algorithms use the fine absorption structure of trace gas

species over a range of wavelengths to determine the concentration by fitting them to

the observed total absorption. This technique is used to differentiate the absorption of

ambient trace gases and will not be used in this work.
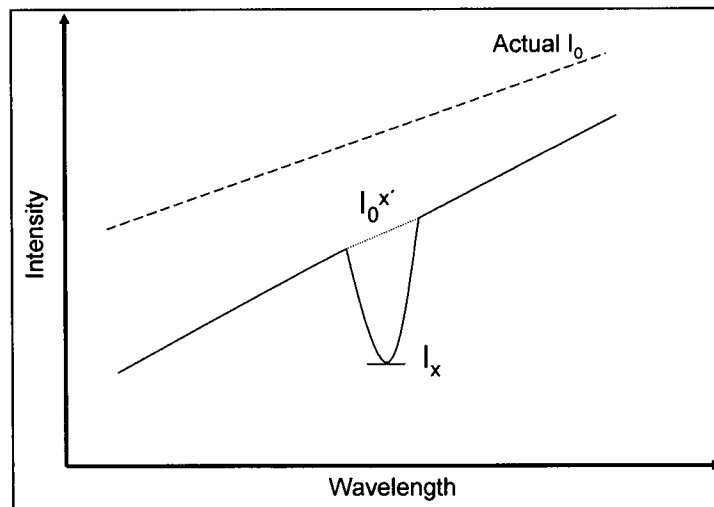
Figure 2.3. The intensity change at a specific wavelength species X is known to absorb can be used to determine the concentration of species X in a sample containing other constituents. I_0 is the intensity of the light source and is measured before the light passes through the sample. The loss of light through an atmospheric sample caused by aerosols will be broad, with no sharp features. Therefore if a sharp drop in light intensity is observed at a wavelength where species X absorbs (I_x), the intensity without species X present can be interpolated ($I_0^{x'}$) and the concentration of X determined with Equation 2.2. This figure was adapted from Finlayson-Pitts 1999 and Platt and Stutz 2008.

There are two main types of DOAS instruments, active and passive. Active DOAS instruments use an active (man-made) light source to make measurements. The light source is usually a Xe lamp, broadband laser, or an incandescent quartz-iodine lamp (Armerding, Spiekermann et al. 1992; Brauers, Aschmutat et al. 1996; Peters, Pechtl et al. 2005). The light is collimated before being sent through the sample, and is then collected with a telescope and analyzed by a detector. To achieve atmospherically relevant detection limits for trace gas species, a long path length is necessary. This can be achieved by placing the light source very far from the detector (e.g. on a nearby island with the detector on the shore) or by folding the path of the light through the sample by using arrays of retroreflectors. The path of the light through the sample can be folded once, or many times, increasing the effective path length to the large distances needed (Brauers, Aschmutat et al. 1996; Saiz-Lopez, Plane et al. 2004).

Passive DOAS systems use natural light sources such as the sun, moon, or stars. The most common passive DOAS system is multi-axis DOAS (MAX-DOAS), which measures the attenuation of sunlight through the atmosphere (Wagner, Dix et al. 2004; Frins, Bobrowski et al. 2006; Li, Brauers et al. 2010) as a function of solar zenith angle (SZA) as shown in Figure 2.4. The sample path length through the atmosphere is changed by altering the view angle of the collection telescope. Measurements at large SZAs provide long atmospheric path lengths (100s km), and enable the measurement of low concentrations of trace species (Platt and Stutz, 2008).
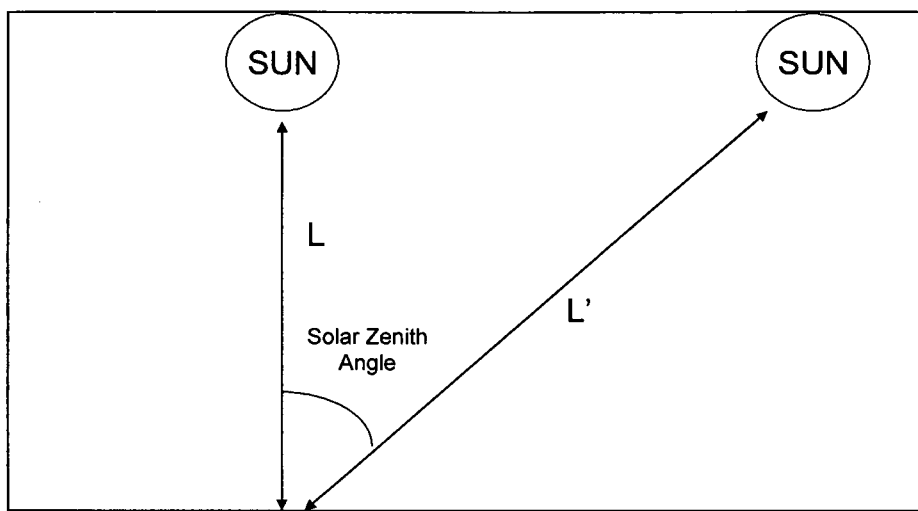
Figure 2.4. As the SZA increases (SZA = 0° when the sun is directly overhead) the path length through the atmosphere (L) increases. For example, if SZA = 30° then L' > L. This allows detection of trace species at low concentrations. However, sample measurements are integrated over the entire path length, which may include multiple air masses, leading to uncertainty in concentration calculations at specific points in the atmosphere.

Active and passive DOAS instruments use the same type of detectors, usually a photodiode array (PDA) or a charge-coupled device (CCD) to measure all wavelengths of light simultaneously. The resolution of DOAS instruments varies based on need. For example, an instrument designed to measure only one species may have a very high resolution in a small wavelength range of interest (0.07 nm), while an instrument used to measure multiple species over a wider range of wavelengths will have lower resolution (> 0.5nm) (Wagner et al., 2004). The raw data is processed by computer algorithms that differentiate the absorption cross sections of the trace gases of interest from the background based on the known absorption spectra of the species (Frankenberg, Platt et al. 2005).

DOAS instruments have been used to measure the concentration of trace gas species for years (Swietlicki, Puri et al. 1996; Platt 1999; Buchwitz, Rozanov et al. 2000; Honninger, von Friedeburg et al. 2004), but more recently they have also been used to measure atmospheric aerosol extinction (Wagner, Dix et al. 2004; Li, Brauers et al. 2010). Initially the transition from gas phase to aerosol extinction measurements was

investigated with MAX-DOAS. MAX-DOAS systems have used the differential

absorption of the molecular oxygen dimer (O_4) at 335 to 365 nm to quantify atmospheric

aerosols. Under normal atmospheric conditions, the distribution of O_4 throughout the

atmosphere is well characterized and stable with higher concentrations closer to the

ground (Volkamer, Etzkorn et al. 1998; Pfeilsticker, Bosch et al. 2001; Wagner, Dix et al.

2004). The interaction of sunlight with aerosols modifies the path the light takes to the

detector, and therefore modifies the exposure of the light to O_4. The line of sight of the

MAX-DOAS decreases as the light is scattered by atmospheric aerosols. As this occurs,

the light is exposed to less O_4 than it would have been if no aerosols were present,

decreasing the measured O_4 absorption at the detector (Figure 2.5). The decreased O_4

absorption versus the predicted values (no aerosol present) can be used to calculate the

aerosol concentration and estimate aerosol optical properties (Wagner, Dix et al. 2004;

Li, Brauers et al. 2010).
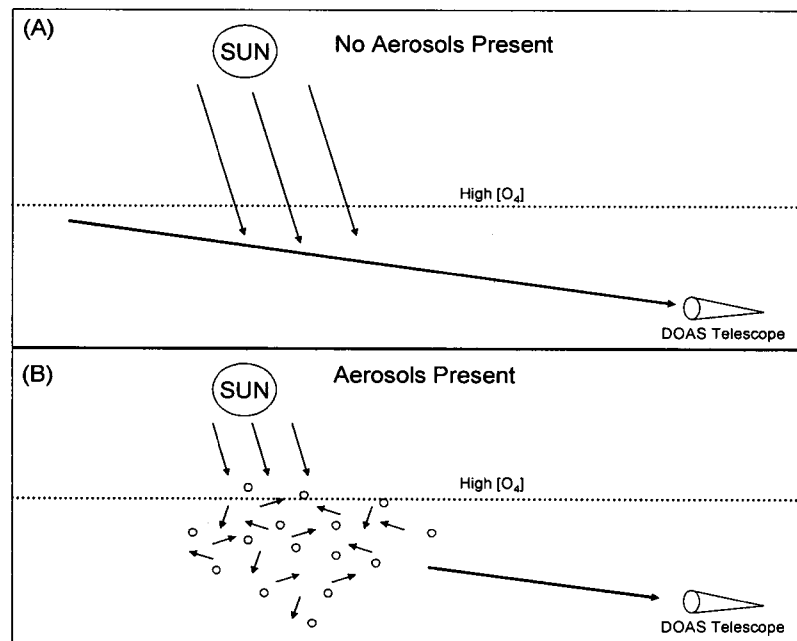
Figure 2.5. (A) When no aerosols are present in the atmosphere the direct line of sight (shown as a bold arrow) of the MAX-DOAS is long, and the light collected by the telescope has a long path length through the lower atmosphere where the concentration of O_4 is highest. (B) The presence of scattering aerosols decreases the direct line of sight of the MAX-DOAS, decreasing the path length of the light through the lower atmosphere, which decreases the measured O_4 absorption. Figure was adapted from Wagner et al. 2004.

Active DOAS instruments have also been used to measure aerosol extinction in the wavelength range of 270-1000 nm. This instrument measures the total attenuation of light over a certain path length. The total extinction of light is due to absorption from gases and aerosols, as well as scattering from gases and aerosols. Corrections can be made for major absorbing gas phase species such as water vapor, ozone, sulfur dioxide, and nitrogen dioxide, based on the observed sharp features in differential absorption spectra and their known absorption cross sections. Rayleigh scattering is dependent on wavelength, temperature, and pressure, and can be calculated. The remaining attenuation of the incident light is attributed to aerosols (Muller, Muller et al. 2005).

Active DOAS systems with short path lengths have been used in laboratory experiments with high concentrations of absorbing gaseous species, particularly in simulation chamber studies (Doussin, Ritz et al. 1997; Wangberg, Etzkorn et al. 1997; Heland, Kleffmann et al. 2001; Volkamer, Platt et al. 2001). The UV-Vis extinction of mineral dust aerosols has been measured using a DOAS system with a path length of 66.5 cm, requiring high concentrations of dust that are greater than 10^6 particles/cm^3 versus atmospheric concentrations that are typically on the order of 10^2-10^4 particles/cm^3 (Mogili et al., 2007). Increased sample path lengths are needed to measure aerosol extinction at particle concentrations closer to those found in the ambient atmosphere.

In this work, the use of a laboratory DOAS system to measured aerosol extinction is advanced. Here, a novel self-contained instrument with a UV-Vis light source was manufactured for the purpose of measuring broadband extinction of aerosols. The laboratory work presented in this text was carried out during the initial characterization of this instrument. Initial experiments with ambient aerosols were conducted from the laboratory, but future work will likely involve ambient atmospheric

measurements at a field site and other studies, which will be explained in detail in Chapter 5.

<u>Aerosol Differential Optical Absorption Spectrometer Description</u>

A bench-top aerosol differential optical absorption spectrometer (A-DOAS) was custom manufactured to our specifications by Cerex Monitoring Solutions, LLC. (CMS UV-5000). This system consists of a 100 watt continuous duty xenon lamp, fiber-optically coupled to a White-type multi-pass gas cell, and then to a single beam UV-Vis spectrometer. The White-type multiple reflection system is made using three separate concave mirrors, each having the same radius of curvature. The distance between the mirrors is twice the focal length in order to clearly reproduce the image of the light source on the mirrors (White, 1942). The xenon lamp and mirrors provide spectral coverage ranging from the mid-ultraviolet to near infrared (approximately 220-1050 nm) at a resolution of better than 0.5 nm (Figure 2.6).
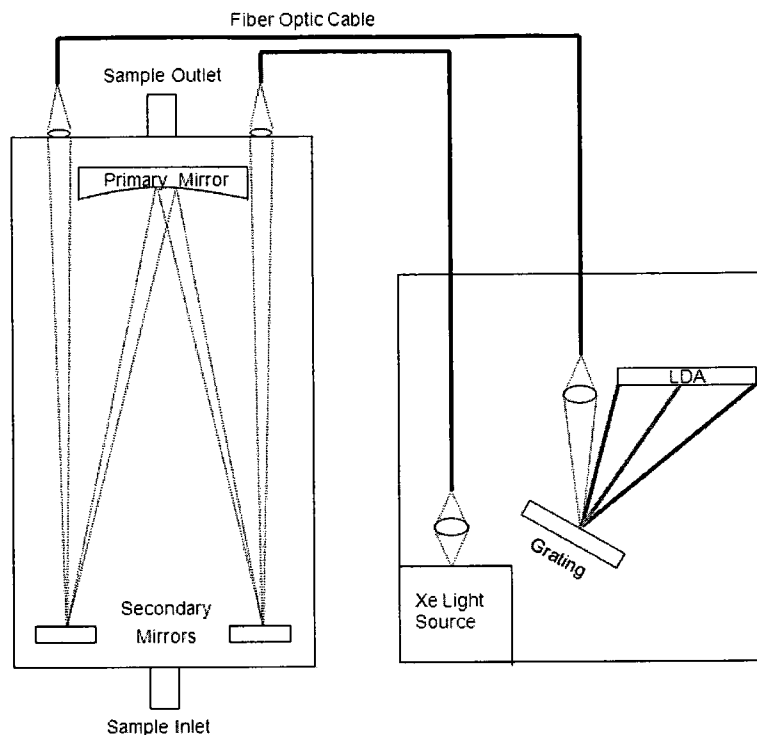
Figure 2.6. Shown is a schematic of the benchtop A-DOAS system. Light from the Xe lamp is focused onto a fiber optic cable and radiated into the multi-pass gas cell (shown on the left). Mirrors reflect the beam of light multiple times through the sample cell before it is focused onto a second fiber optic cable and detected by the spectrometer (shown on the right). The spectrometer consists of a grating and a 3078 element linear diode array.

The stainless steel multi-pass gas cell (left-half of Figure 2.6) has outer dimensions of 73.0 cm x 19.2 cm x 7.5 cm and an internal volume of approximately 5.8 liters. Stainless steel spacers have been placed in the bottom of the gas cell to minimize the internal volume, which reduces sample residence times. The sample inlet and outlet are located on opposite ends of the gas cell, allowing a continuous flow through the system. The inlet is located between the two secondary mirrors to reduce turbulent sample flow. Alignment screws on the two secondary mirrors enable the path length to be modified by changing the number of reflections. The path length can be adjusted by steps of 4 reflections. The allowable path length range is from 4 reflections (2.44 meters) to 32 reflections (19.51 meters, shown in Figure 2.7). Adjustment of the sample path length is achieved by looking into a viewing port and counting the number of reflections on the top of the primary mirror. Fine tuning is achieved by monitoring the

light intensity reaching the detector using the "Align" features in the CMS computer program provided by the manufacturer (See A-DOAS Operation section at the end of this chapter).
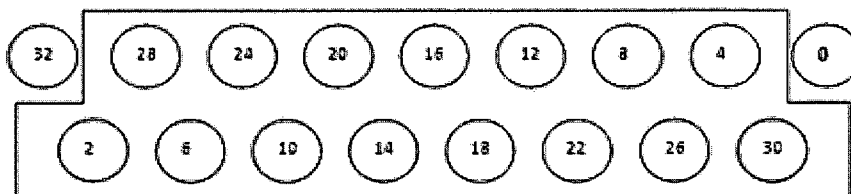
Figure 2.7. An illustration of the path of the light beam on the primary mirror of the multi-pass gas cell at the most commonly used path length (19.51 meters). The beam enters the gas cell at position 0, is reflected for the first time off one of the secondary mirrors, followed by its primary mirror reflection at position 2. This process repeats until the light exits the gas cell at position 32, where a lens focuses the light onto a fiber optic cable. The odd numbered reflections occur on the two secondary mirrors, which are not shown here.

The A-DOAS instrument differs from other laboratory DOAS systems for the measurement of aerosol extinction. This instrument utilizes a closed gas cell that allows for multiple reflections of the incident broadband light through the sample. Other systems have used an open path through the atmosphere with multiple reflections from an array of retroreflectors (Müller et al. 2005), or a single reflection in a closed flow tube (Schnaiter, Schmid et al. 2005; Virkkula, Ahlquist et al. 2005). Aerosol extinction measurements have also been conducted with similar closed White-type multi-pass cells, but these systems have operated at IR wavelengths or use only narrow band light sources such as lasers or LEDs (Schnaiter, Horvath et al. 2003; Langridge, Ball et al. 2006; Najera, Fochesatto et al. 2008; Varma, Venables et al. 2009; Meinen, Thieser et al. 2010).

When designing and testing the A-DOAS, it was important to consider gas phase species that could possibly interfere with the aerosol extinction measurements. Nitrogen is used as the carrier gas for all laboratory studies with the A-DOAS to minimize interferences. Yet, the magnitude of possible atmospheric interferences must be fully

characterized before quantitative extinction measurements of ambient aerosols can be attempted.

Gas Phase Interferences

Based on typical ambient concentrations and measured absorption cross sections, ozone, nitrogen dioxide, sulfur dioxide, and water vapor are known to be the dominant absorbing atmospheric gases in the wavelength range of the A-DOAS instrument (Table 2.1) (Gas phase UV-Vis absorption cross sections are available at http://www.atmosphere.mpg.de/enid/2295.html). However, there are over 40 gaseous species that were found to strongly absorb in this wavelength range. These gases were also considered as possible interferent due to previously reported high mixing ratios. Calculations were performed, using the three-year local maximum concentrations of these gases (1/1/2005 to 1/1/2008), obtained from a local air monitoring site (data from - http://www.airmap.unh.edu/DownloadData), and absorption cross sections from the literature (Horowitz, Meller et al. 2001; Voigt, Orphal et al. 2001; Coheur, Fally et al. 2002; Bogumil, Orphal et al. 2003). The maximum extinction at this site for these gases was determined. It was found that the majority of the 40 trace species will have a negligible effect (less than 10^{-6} cm^{-1}) on aerosol extinction spectra (individual data not shown). The major interferences are shown in Table 2.1.

Table 2.1. The calculated expected maximum absorbance interference for over 40 gases was calculated using the 3-year maximum local concentration (http://www.airpmap.unh.edu) of the gas and its absorption cross section. The three gases with the largest interference at each wavelength are shown.

Wavelength (nm)	Calculated Maximum Extinction (cm^{-1})	Calculated Absorbance (AU) L=2000 cm	Major Interfering Species (order of strength)
230	2.33×10^{-05}	0.02072	O_3, NO_2, PAN
250	3.05×10^{-05}	0.02733	O_3, SO_2, NO_2
270	2.26×10^{-05}	0.02013	O_3, SO_2, NO_2
300	2.38×10^{-06}	0.00207	SO_2, O_3, NO_2
320	3.98×10^{-07}	0.00034	NO_2, O_3, SO_2
400	7.11×10^{-07}	0.00061	NO_2, H_2O, SO_2
532	1.57×10^{-07}	0.00013	NO_2, O_3, H_2O
650	1.71×10^{-06}	0.00148	H_2O, NO_2, O_3
800	7.43×10^{-10}	< DL	NO_2, O_3

Ozone has very broad absorption bands throughout the UV-Vis spectrum and high concentrations can increase the measured extinction at almost all wavelengths (Voigt, Orphal et al. 2001). A spark discharge ozone generator was used to produce an ozone rich sample mixed with room air in a laboratory fume hood. The absorption interference of ozone was observed and the alignment of the linear diode array detector confirmed. A background measurement of room air was collected, followed by sampling of ozone rich air near the outlet of the ozone generator. The absorption spectra obtained at UV wavelengths is comparable to published data (Bogumil, Orphal et al. 2003), as shown in Figure 2.8.
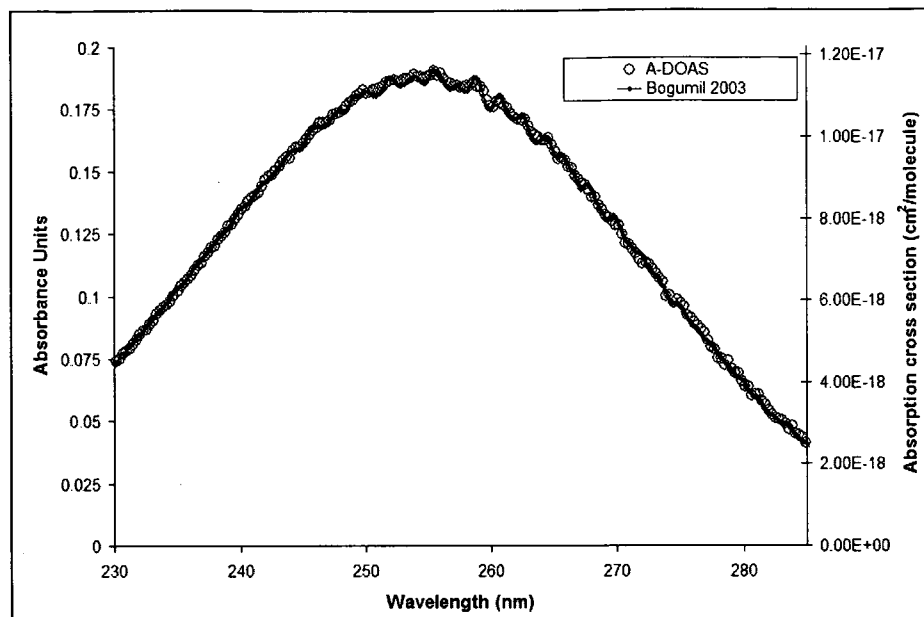
Figure 2.8. The measured UV absorption of ozone at a path length of 9.75 meters, in absorbance units, is located on the left y-axis, corresponding to a concentration of 647 ppbv. This is compared to the absorption cross section of ozone on the right y-axis (Bogumil, Orphal et al. 2003).

The measured ozone absorption and the reference values are in agreement, indicating that the spectrophotometer is properly aligned and that the diodes are measuring the wavelengths they are supposed to be measuring. The A-DOAS measurement of ozone was made at concentrations that are not realistic for the atmosphere, even in the most polluted circumstances. Measurements of ambient air at longer path lengths may contain interferences from ozone, but this should not affect aerosol extinction data if frequent backgrounds are measured and ozone concentrations do not drastically change during a sample measurement.

Comparison between laboratory room air samples indicated that there was an unidentified species interfering with measurements at approximately 275 nm (Figure 2.9). This interference was observed with both room air and filtered room air, indicated that the absorption was due to a gas phase species. A review of the literature and subsequent laboratory experiments showed that the interfering species was likely acetone (Figure 2.9) (Meyrahn, Pauly et al. 1986). Acetone is used in this room to clean

30

mirrors, and interferences may also be seen from other areas of the building as there are working laboratories in close proximity. The acetone concentration in the background air will change from day to day, and this must be monitored if A-DOAS measurements using ambient room air are made.
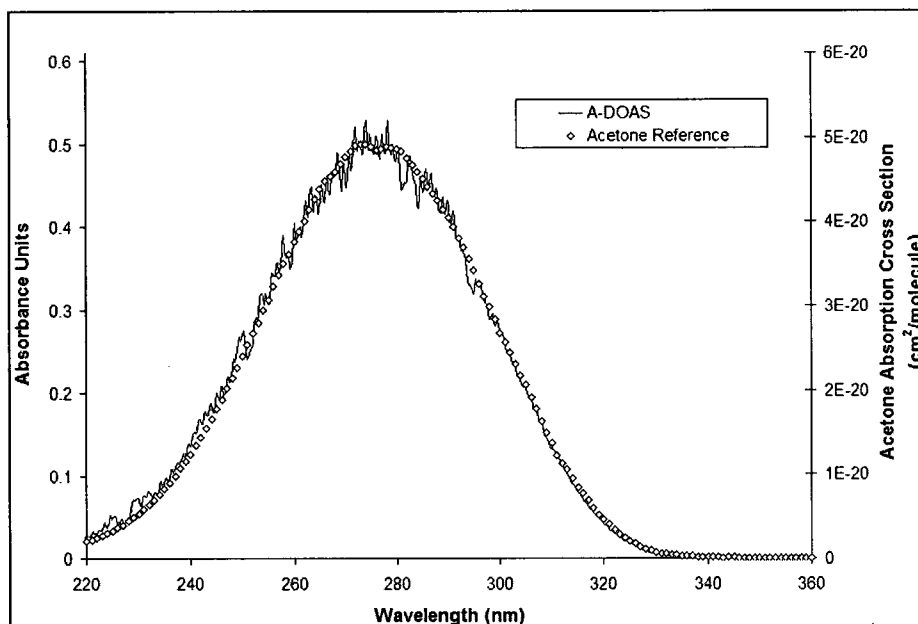
Figure 2.9. A measured acetone sample (L = 19.51 m), smoothed with a 5-point boxcar average is compared to a reference spectrum of gas phase acetone. With the close match it can be concluded that the interfering species observed in a sample of room air is acetone.

A-DOAS Detection Limit

The Xe light source of the A-DOAS is continuous from approximately 220-1000 nm, but the output is not as smooth as a blackbody source. Figure 2.10 shows the output intensity of the lamp as measured by the A-DOAS with filtered nitrogen (Airgas – UN1066) in the gas cell. There is a large broad intensity peak in the UV and visible up to approximately 750 nm. At wavelengths between 780 – 880 nm the lamp intensity is low, and after 900 nm there are sharp emission peaks from the Xe lamp. The spectrum displayed in Figure 2.10 was measured with a sample path length of 19.51 meters and an integration time of 90 seconds. The intensity and shape of the lamp spectrum change when aligning the mirrors. Slight adjustments in the angles of the mirrors alter the path of the beam and can produce large differences in the lamp spectrum.
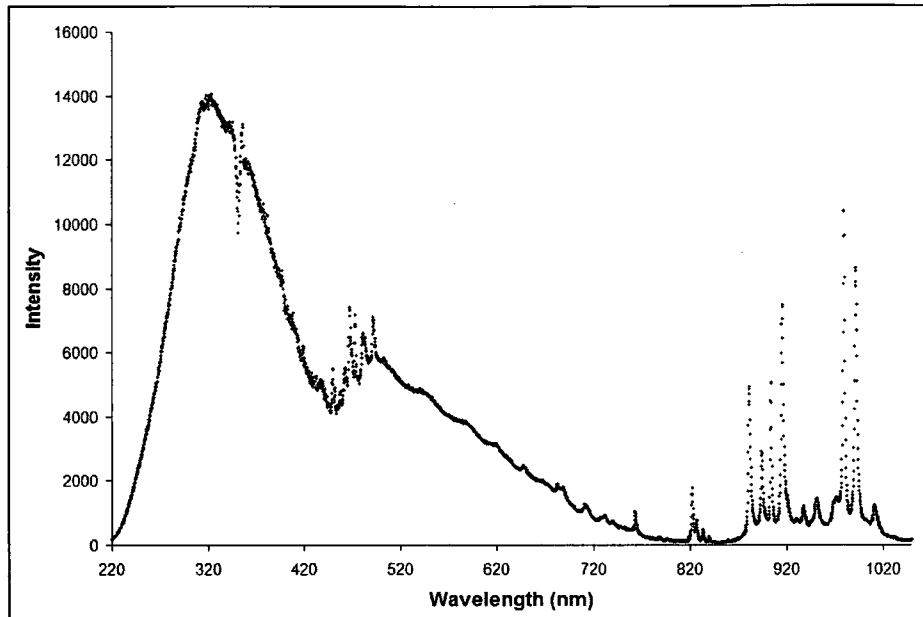
Figure 2.10. Small adjustments to the angle of the secondary mirrors in the gas cell can affect the intensity of light that reaches the detector. As adjustments are made the shape of the lamp spectrum will also change. The example lamp spectrum shown in this figure has been found to be the most stable when performing aerosol extinction measurements.

The lamp spectrum in Figure 2.10 shows the intensity and shape that have been found to work best for extinction measurements. The shape of the lamp spectrum can be adjusted by moving the secondary mirrors and the intensity can be manually adjusted by changing the measurement integration time. Chapters 3 and 4 will discuss the wavelength dependence of the refractive index of materials, and this same principle applies to the lenses used to collimate the light from the Xe lamp. Shorter wavelengths are refracted more than longer wavelengths by the lens. Therefore, by the time the light reaches the exit of the gas cell (spot #32 in Figure 2.7) the wavelengths in the collimated beam of light are separated to a certain degree. This means that slight changes in the alignment of the mirrors can affect certain wavelengths more than others, which has been found to be particularly true for the UV wavelengths of light. Therefore, care must be taken to ensure the lamp spectrum looks like the one displayed in Figure 2.10 before extinction experiments are performed, and the spectrum should be checked between each experiment to ensure it has not changed.

The A-DOAS was found to be susceptible to pressure changes caused by variable sample flow rates through the gas cell. The A-DOAS mirrors are attached to the lid and pressure changes cause the lid of the A-DOAS gas cell to imperceptibly bow, which alters the path of the beam in the gas cell, changing the intensity of light reaching the detector. An extreme example of the phenomenon is shown in Figure 2.11. The nitrogen flows were abruptly changed from 0.3 to 3.0 L/min, causing a pressure change in the gas cell, which resulted in a "pressure peak". Since this experiment, a volume spacer that was located on the lid of the gas cell was removed, and all experiments shown in this work were performed after the removal of this spacer. This has reduced the intensity of the pressure peaks by approximately a factor of 10 as the spacer was too close to the beam path. A-DOAS pressure peaks can be avoided entirely by carefully regulating sample flow rate to ensure it stays constant over the course of an experiment. All data displayed in this work show no signs of a pressure peak unless stated otherwise. It should also be noted that the pressure peaks shown in Figure 2.11 were forced to be large by varying the flows by a substantial amount. Variation in flows during experiments is small (0.01 – 0.05 L/min) and produce small broad pressure peaks from approximately 300-400 nm, typically without negative absorbance peaks at wavelengths less than 300 nm.
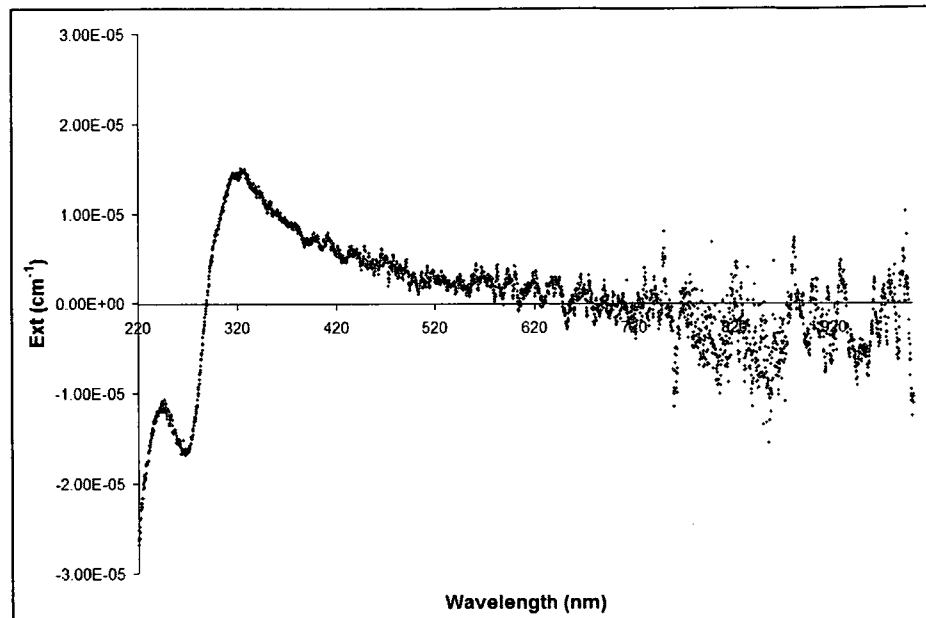
Figure 2.11. A change in sample flow rate through the A-DOAS gas cell can cause a change in pressure. This pressure change moves the lid, altering the path of the light and changing the intensity of light that reaches the detector. This affects the data by producing a positive or a negative pressure peak. This figure was produced by measuring filtered nitrogen at 0.30 L/min, setting this trace as the background, and then measuring filtered nitrogen at 3.00 L/min.

Both determining the best lamp spectrum to use for experiments and eliminating pressure peaks from the extinction data have improved the detection limit of the A-DOAS. Instrumental detection limit is commonly defined as 3σ of the baseline noise of two consecutive measurements, and a typical example of the A-DOAS wavelength dependent detection limit is shown in Figure 2.12. The detection limit shown was calculated using two consecutive measurements of nitrogen with a path length of 19.51 m and an integration time of 180 seconds. Each data point displayed in Figure 2.12 is the average of 5 measured wavelengths; this was done to smooth the data and make the trace clearer.
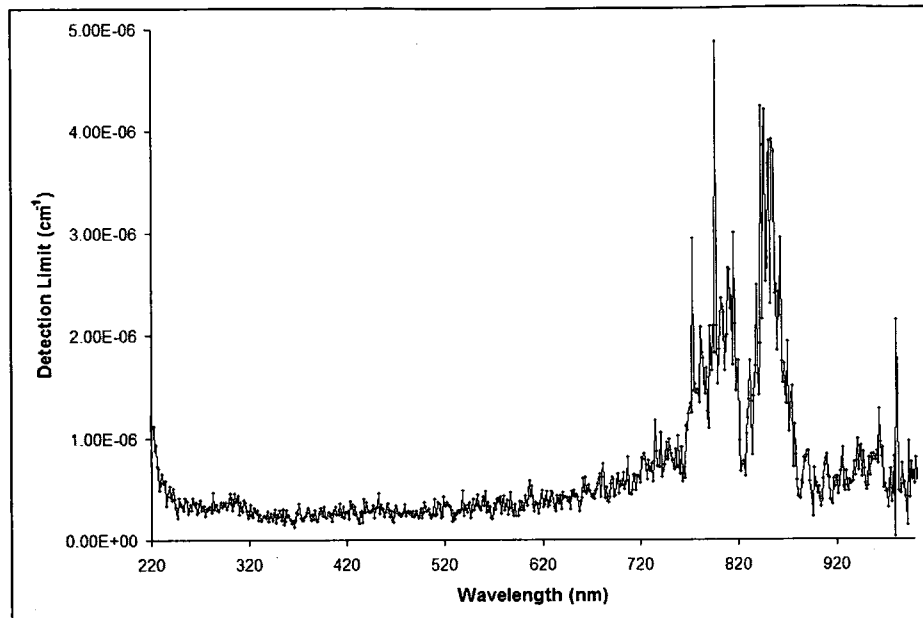
Figure 2.12. The A-DOAS detection limit is steady from approximately 235-700 nm. The detection limit increases at wavelengths less than 235 nm and greater than 700 nm due to the decreased intensity of the lamp.

The average detection limit of the A-DOAS from 235-700 nm is 3.25×10^{-7} cm^{-1}. The *lower* detection limit of the LOPES instrument, the instrument most similar to the A-DOAS discussed in Chapter 1, is given as 2.0×10^{-7} cm^{-1} (Schnaiter, Schmid et al. 2005). However, since this value is quoted as a lower detection limit, there is no way to know what the average or wavelength dependent detection limit of that instrument is; it could be highly variable over the range of wavelengths measured. The lower detection limit of the A-DOAS measurement shown in Figure 2.12 is 1.26×10^{-7} cm^{-1} at 366 nm and has been observed to be as low as 6.2×10^{-8} cm^{-1} at approximately 350 nm for the backgrounds before some experiments. The detection limit of the A-DOAS will change between experiments and can easily be calculated for any experiment by finding 3σ of the baseline of the last two zero measurements before the sample is introduced.

The work in this chapter was performed to show that the A-DOAS is capable of accurately measuring the extinction of aerosol samples. Experiments with ozone and acetone samples showed that the diodes in the LDA are properly aligned at the correct wavelengths. Detection limit calculations showed that the A-DOAS is comparable to

similar techniques. The remainder of this chapter is an A-DOAS operating procedure, which will be useful to future users. Chapters 3 and 4 will focus on experiments to determine the extinction of various aerosol samples was measured; verifying the capability of the A-DOAS to measure both highly scattering and highly absorbing aerosol samples in a controlled laboratory setting.

A-DOAS Operation

This section is meant to be used in conjunction with the A-DOAS folder that includes setup and start-up procedures from Cerex Monitoring Solutions.

A-DOAS Start-up

- Remove blue caps from fiber optic cables and connect FS labeled cable to the "From Source" port on the gas cell, and the TS cable to the "To Spectrometer" port.
- Connect the USB cable from the UV5000 to the A-DOAS computer

- Turn ON UV5000

- Allow 30-45 minutes for the light source to reach the proper temperature and stabilize. When measuring a sample with an expected extinction close to the detection limit of the A-DOAS (e.g. ambient air) a lamp warm-up time of 1 hour is recommended, as this shows the greatest lamp stability.

- Open CMS program to collect data – USB cable must be connected for the program to open properly.

- Go to *Setup* → *Align* to set the integration so the maximum lamp intensity is between 14,000 – 16,000 units. This will change depending on the path length – shorter path lengths will have lower integration times then long path lengths. This should be adjusted before each experiment.

Zero Measurement (Background)

- A blank measurement must be made before each experimental sample trial in order to accurately calculate the extinction of the sample. <u>Example</u> - For atomized samples the blank measurement should be N_2 flowing through the experimental setup with the atomizer pump off. To minimize pressure peaks, the flow rate should be exactly the same as the sample flow rate.

- After allowing adequate lamp warm-up time, flow the blank sample through the gas cell for approximately 10-15 minutes before acquiring data. If there were any particles left in the gas cell from previous measurements, this will remove most of them. The Condensation Particle Counter (CPC) counts should be < 1 particle/cm^3 before sample introduction.

- Monitor particle concentrations while taking blank measurements to ensure that there are no particles in the gas cell when you acquire the final blank measurement, which will be used as the "zero" for your sample.

- Save the "zero" measurement when the particle concentration is less than 1 particle/cm^3 and three consecutive A-DOAS blank measurements show no deviation in the baseline (set each individual measurement as the background for the next until the baseline stops changing *Acquire* → *Background* → *Last Acquisition*). Make note of the file count "FC" number of the zero measurement. Use this as I_0 for extinction calculations. By default all files are saved to C:\\Desktop\savedfiles, and it's best to name them by date and sample.

- Stop the A-DOAS data acquisition after the zero measurement and save it as the background. Name the sample file and restart data acquisition once the sample generation has begun.

- The intensity of the lamp changes slightly over time, so it is best to start the sample measurements as soon after acquiring the zero measurement as

possible. Example – For an atomized sample simply flip the atomizer pump on after measuring the zero the start the aerosol sample measurements.

<u>Sample Measurements</u>

- Samples should be measured the same day they are prepared to limit contamination and/or coagulation of species in the sample.

- The A-DOAS experimental setup will change depending on the type of measurement being made – measuring size selected particles versus measuring a size distribution of particles. Please see Chapters 3 and 4 for explanation of the experimental setups.

- With your zero file set as the background for the sample measurements, you should start to see a positive extinction signal for the sample after approximately 10 minutes for a flow rate of approximately 0.35 L/min. If there is no extinction signal after 15-20 minutes, the particle concentration is likely too low to attenuate light at levels above the detection limit of the A-DOAS, and an alternate experiment should be attempted.

- When an adequate number of sample measurements have been made (approximately 3-5 measurements after particle concentration has leveled off), stop the generation of aerosols. It is recommended that A-DOAS data acquisition continue until the particle concentration is once again below 1 particle/cm^3. This provides the user with an idea of how much the lamp intensity may have changed since the first zero, or if there has been particle build up on the mirrors.

- When the sample measurement is complete, either repeat the zero/sample measurements with a new sample or shutdown the A-DOAS.

A-DOAS Shut-down

- Stop data collection

- Turn UV5000 OFF

- Disconnect fiber optic cables and place blue caps on the ends

- Place fiber optic cables on top of the UV5000 – make sure they are not in an area where they can be bent or crushed

- Disconnect USB cable from the computer

- Disconnect any remaining tubing from the gas-cell

- Power off any additional equipment used in the experiment such as a pump or flow controller

- **If necessary** - See lab door for the proper shut-down procedures for the Atomizer and Scanning Mobility Particle Sizer (SMPS)

Troubleshooting

Absorbance spectrum of blank measurements do not remain stable: If consecutive measurements of a blank sample (with each new measurement being set as the background) keep changing, something is not correct. Most likely the lamp is not warmed up to its operating temperature. However, this may also occur if there are still particles in the gas cell, or if the flow through the gas cell is not constant (see below), therefore these should be checked as well.

Absorbance spectrum of blank (or sample) measurements keeps changing especially around 300-400 nm: If the absorbance measurements of a blank keep changing with a peak growing into positive absorbance, or shrinking into negative absorbance relative to the baseline then it is likely that the flow through the gas cell is not constant. If this happens, find a way to ensure a steady flow rate through the gas cell with the suggestions below. This can also be observed during sample

measurements when an obvious peak in this region forms for no reason. If this happens you may want to follow the suggestions below and start over.

Suggestions for Fixing Problems

- Regulate the flow into the gas cell with a mass flow controller (MFC), unless controlling the flow with the CPC pump.

- Remove the Differential Mobility Analyzer (DMA) impactor from the experimental setup. Build-up of particles on the impactor can restrict flow over time and change the pressure in the gas cell.

- The sample flow rate can change over time when the atomizer pump is on. This will be most obvious when going from a blank with the atomizer pump off to a sample with it on. Over time the flow through the gas cell will decrease, with more flow going into the waste line. To alleviate this problem as much as possible it is suggested that a flow meter be placed on the equilibration filter at the CPC inlet to monitor this flow. The flow meter should indicate that flow out of the equilibration filter decreases over time, meaning the flow through the gas cell decreases. If this happens, place a metering valve on the front of the DMA and adjust it to keep the flow out of the equilibration filter constant. This is the best way to ensure a steady flow through the gas cell without risking over pressurization of the CPC.

- The backing pressure of the pressure gauge on the N_2 tank will change over time. If this happens, the flow rate of N_2 through the experimental setup can change. This should not be a problem if an MFC is placed between the N_2 tank and the atomizer unless the tank is very low. If that is the case, replace the tank. Always check the tank before starting an experiment to make sure there is enough N_2 for the entire experiment. If the N_2 runs out during an experimental

trial, it will most likely need to be restarted from the beginning due to changes in the zero.

Particles concentrations are too low to provide a signal above the detection limit: This is often the case when size selecting an aerosol sample. To increase the concentration of atomized aerosols follow these steps:

- Close the needle valve on the front of the atomizer. This forces all of the N_2 flow to go through the atomizer block, which creates more aerosols and lowers dilution by N_2 that would have flowed through the needle valve.

- Move the tee that splits the aerosol flow into sample and waste flows to the front of the DMA. Splitting the flow farther away from the atomizer increases the concentration of particles farther downstream. Particle concentrations of a sample split to waste at the front of the DMA have been measured to be multiple times higher than a sample split to waste right after the atomizer.

- Increase the speed of the atomizer pump. This increases the sample flow into the atomizer block, which increases the concentration of atomized particles.

- Increase the N_2 flow into the front of the atomizer. An inlet flow of 3.00 L/min (the maximum flow rate of the MFC) has been used to achieve high particle concentrations in the past.

The baseline after a sample isn't the same as it was before the sample: This happens as the lamp intensity changes over time. It can also happen if a sticky sample is used and some particles are deposited onto the mirrors or lenses in the gas cell. If this happens the researcher must decide whether or not to use the sample measurements with the original zero or to correct the data with the blank measurement performed after the sample. If the change in baseline is small you may want to note this difference but not correct the data. If it is large, it is possible to subtract the second zero from the sample data, or use the second zero as I_0. If the

difference is very large, something may have happened during the experiment (i.e. fiber optic cables were bumped, the gas cell was bumped, flow changed, etc.) and the experiment should be repeated.

The intensity of the lamp is lower or higher than it used to be: This can happen if the gas cell was recently moved or bumped, altering the alignment of the mirrors.

To **re-align the mirrors**:

- There are 4 screws on the end of the A-DOAS, the same side as the two secondary mirrors. Remove the two screws on the left hand side.

- The 5/64" Allen wrench will fit into these holes and the screws needed to adjust the mirrors.

- Remove the fittings on the A-DOAS inlet (same side as the screws). This will act as a viewing port. DO NOT look into the A-DOAS without UV eye protection.

- Look into the A-DOAS gas cell and locate the spots of light on the primary mirror. You should see a pattern of spots resembling the top row from Figure 2.7.

- Adjusting the screw inside the top hole will move the line of spots up and down. Adjusting the screw in the bottom hole will move the spots side to side, increasing or decreasing their number. You may need to feel around with the Allen wrench for a couple of minutes to find the screw.

- Adjust these two screws until you have the desired number of spots. Example – Seven spots on the top row equals a path length of 19.51 meters. Each reflection inside the gas cell is 0.61 meters (24 inches).

- When you have the desired number of spots you will need to make small adjustments to both screws to maximize the intensity of light reaching the detector. To do this you will need to have the CMS program open and go to *Setup → Align*.

- Watch the spectrum on the computer screen to maximize the light intensity, focus on the UV range. Adjust the integration time until the maximum intensity is above 14,000 but below 16,000. This ensures that enough light reaches the detector to make an accurate measurement, but not so much light that the detector becomes "overloaded". If too much light reaches the detector at a certain wavelength the absorbance spectrum will display a flat line at zero absorbance units, and this is unusable. It is okay if the peak intensity of the sharp peaks at >800 nm are above 16,000.
- Save the settings, replace the screws and fittings on the inlet, resume measurements.

Maintenance

- Periodically, the DMA and CPC will need to be cleaned and parts changed out. Please follow the individual DMA and CPC manuals for the correct maintenance procedures.
- Check the fittings and tubing connected to the A-DOAS periodically (approximately weekly or between different types of samples) for build-up of aerosol residue. Clean with DI water and methanol by squirting them with the wash bottles. Clean with DI water first, followed by methanol. Let the fittings dry before reassembling.
- The entire atomizer should be disassembled and cleaned between different types of aerosol samples (i.e. nigrosin and PSLs) to avoid contamination. Clean all fittings with DI water and methanol.
- The mirrors and lenses in the A-DOAS gas cell should be clean periodically. This does not have to be done often, approximately every month or two. The timing of this will depend on how heavily used the A-DOAS has been. Heavy use = clean more often. Remove all the screws from the top of the gas cell and

CAREFULLY remove the lid. Place it mirrors up on the lab bench. Use the acetone/methanol drop and drag method to clean the primary mirror and two secondary mirrors. Use a dry optical wipe to clean any dust off of the two lenses located where the fiber optic cable attach. Wipe the interior of the gas cell with a damp Kim Wipe to remove any dust or particles. Carefully replace the lid on the gas cell and tighten all the screws. You will need to re-align the mirrors after this (see above).

The Xe lamp has a lifetime of approximately 2,000 hours. However, the A-DOAS manufacturer expects that the lamp could last upwards of 4,000 hours. The hours of operation of the lamp is displayed on the front of the UV 5000. A layer of dust from the electrodes within lamp will slowly build up, reducing intensity over time. When this happens the lamp should be replaced following the instructions in the CMS A-DOAS folder. At the time this work was completed the total A-DOAS lamp hours of operation was 1081 hours.

CHAPTER 3

EXTINCTION OF HIGHLY SCATTERING AEROSOLS

Optical Constants

The optical properties of a particle, how it will interact with light incident upon it, can be described by the optical constants for that particular particle, as well as its size and shape. All particles in this work are assumed to be spherical, unless indicated otherwise. There are two set of optical constants that are routinely used to describe the optical properties of particles: the complex refractive index and the complex dielectric function. These optical constants are related, but this work will only use the complex refractive index to describe the optical properties of aerosol particles. The complex refractive index is defined as $m(\lambda) = n(\lambda) + ik(\lambda)$, where n is the real part of the refractive index, and k is the imaginary part also known as the extinction coefficient. The complex refractive index can also be written as $m = n - ik$, and both formulas yield the same optical properties. The real part of the refractive index, at a given wavelength λ, is defined as,

$$n(\lambda) = \frac{c}{v} \qquad (3.1)$$

where c is the speed of light in a vacuum (2.99792258×10^8 m/s), and v is the speed of light in the specific material. For example, the speed of light is slower in water than a vacuum, which leads to a measured refractive index of 1.333489 at 587.725 nm at 19°C (Daimon and Masumura 2007). As light propagates from one material into another material with a different refractive index, the light is refracted, which changes the direction of propagation of the light. An example of this process can be seen in Figure

3.1. The relationship between the incident and refracted light is given by Snell's Law,

$$\frac{\sin(\theta_1)}{\sin(\theta_2)} = \frac{n_2}{n_1} = \frac{v_1}{v_2}$$ (3.2)

where θ_1 is the angle of incidence to the normal, the normal is indicated by a dotted line in Figure 3.1, θ_2 is the angle of refraction in medium 2, n_i is the refractive index of medium (i), v_i is the speed of light in medium (i).
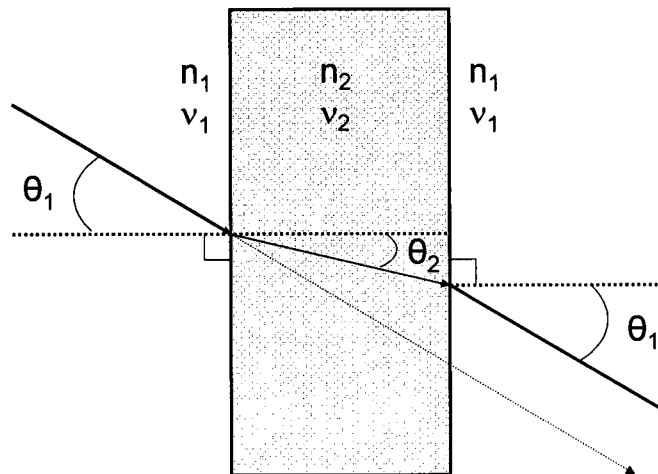
Figure 3.1. Incident light is refracted as it propagates from a material with one refractive index (n_1 = 1) into a material with a different refractive index ($n_2 > 1$). The second angle of refraction, also labeled θ_1, is equal to the angle of incidence because the normal (bold dotted lines) does not change.

If the interface between two materials is flat, and the angle of the normal does not change, light will exit the second material at an angle equal to the incident angle. However, the light exits at a different location than it would have if n_1 was equal to n_2, which is depicted by the finely dotted arrow in Figure 3.1. An example of this phenomenon in everyday life is a straw sitting in a glass of water. Viewed from the side of the glass, the straw appears disconnected below the water line because the light is being refracted by both the glass and the water. The light exiting the glass is in a different location than it would be if there was no difference in refractive index between the materials, giving the viewer a false sense of the straw's location.

The idea of refracted light becomes more complicated when the second material is spherical. The normal to the sphere changes depending on location (Figure 3.2). The lack of parallel interfaces between the two media on a spherical particle (except at 90°) causes the light exiting the particle to propagate in a different direction than the incident light. This process contributes to the overall light scattering by the particle, as mentioned in Chapter 1 and depicted in Figure 1.3 (Bohren and Huffman 1983).
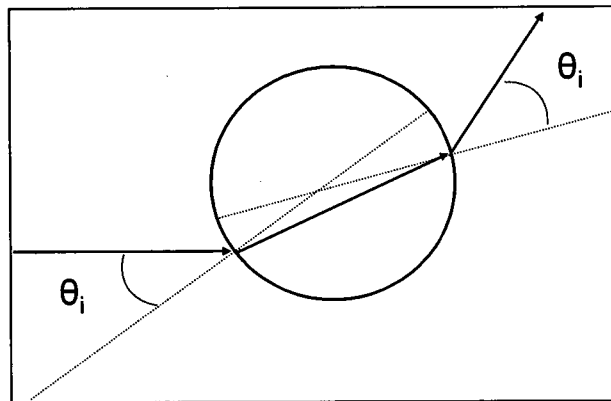
Figure 3.2. The diffraction of light by a sphere is different than diffraction by a material with flat surfaces. The normal to the sphere (finely dotted lines) changes depending on the location of the light-particle interaction on the surface of the sphere. The light exits the particle at an angle equal to the angle of incidence, but it is no longer traveling in the same direction.

The complex refractive index is dependent upon the wavelength of light interacting with the particle. In general, n can be considered the part of the complex refractive index that indicates the extent to which a particle will elastically scatter incoming light, while k, the extinction coefficient, indicates how much light will be attenuated by the particle. Any light that interacts with the particle that is not elastically re-emitted is said to be attenuated. Light absorption is an example of this phenomenon. Visible light can interact with and be absorbed by a particle. The energy of the light is then converted to heat and inelastically re-radiated at a longer wavelength. However, while it is often useful to think of these quantities (n and k) as discretely controlling the optical properties of aerosols, they are not independent of one another. For a given particle, the real part of the refractive index increases with decreasing wavelength,

unless the particle has a high extinction coefficient. The relationship between n and k for highly absorbing aerosols will be discussed further in Chapter 4. The current chapter will focus on aerosols that primarily scatter light.

Scattering of Light by a Sphere

The processes that dominate atmospheric scattering are Rayleigh and Mie scattering, which were briefly mentioned in Chapter 2. The scattering that occurs via these two processes is elastic, the energy of the scattered photons does not change. Raman scattering, where the energy of the scattered photons does change, will not be considered in this work. Rayleigh scattering describes how light is elastically scattered by atmospheric gas molecules. This process can be used to describe the interaction of light with spherical particles that are small compared to the wavelength, typically for particles with diameters less than one tenth the wavelength of light. Rayleigh scattering is wavelength dependent, meaning shorter wavelengths scatter more efficiently. Mie theory provides a more complete description of the interaction of light with spherical particles, and reduces to Rayleigh scattering theory for particles in that size regime. Therefore, Mie theory has been used to characterize the interaction of light with all particles used in this work.

Mie theory, which uses an analytical solution to Maxwell's equations for the interaction of light with a dielectric sphere, describes scattering of light from particles with diameters approaching or exceeding the wavelength of incident light. Unlike Rayleigh scattering, Mie scattering from large particles is not very wavelength dependent. A particle's size parameter (χ), which is defined as $\pi d/\lambda$, is a useful term when considering the scattering of light from a particle. Two spherical particles with the same refractive index and same size parameter will scatter in exactly the same way. For example, a 300 nm water droplet will scatter 300 nm light ($\chi = 3.14$) in exactly the same

way a 700 nm water droplet scatters 700 nm light (χ = 3.14). The size parameter is also

useful in determining the angle of the scattered light; the angular distribution of scattered

light for two cases mentioned above will be the same. Figure 3.3 shows the angle of

scatted light from a water droplet (m = 1.33 + 0i) at a size parameter well within the

Rayleigh scattering regime (χ = 0.1).
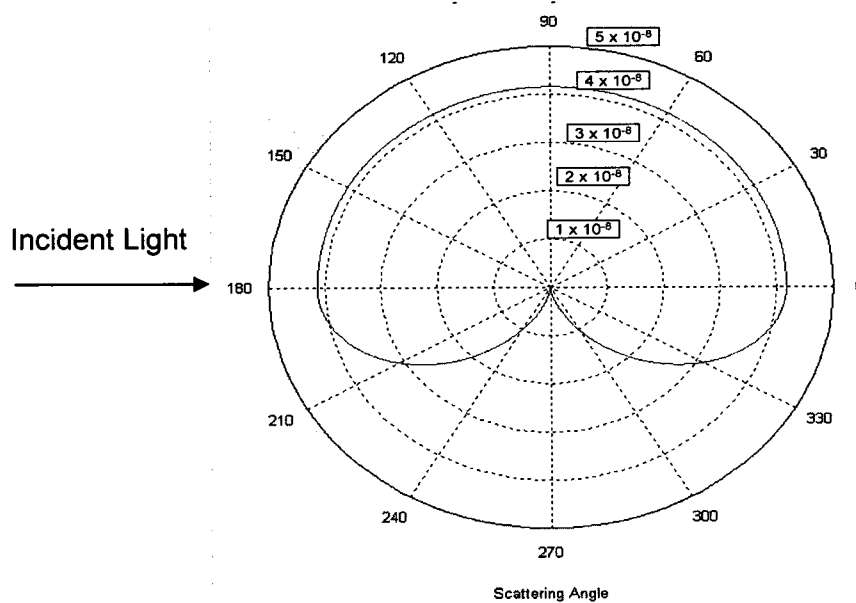
Figure 3.3. The angular dependence of scattering from a water droplet (m = 1.33 + 0i) in the Rayleigh scattering regime (χ = 0.1), as calculated by Mie theory. The intensity of the scattered light is equal in the forward and backward direction. Total scattering from a real particle will occur at all angles, but in this figure the lower half of the figure represents the scattering of light polarized parallel to the scattering plane, while the upper half shows scattering of light perpendicularly polarized to the scattering plane.

Figure 3.3 was created using a Mie theory MATLAB program based on Mätzler,

2002a and 2002b. Unless otherwise indicated, all MATLAB figures depicting scattering

angles display the results of light polarized perpendicularly to the scattering plane in the

upper half plane, and light polarized parallel to the scattering plane in the lower half.

Overall, this gives a good indication of the angular dependence of scattered light.

However, the light source used to obtain experimental measurements in this work emits

un-polarized light. The total scattering of un-polarized light by the same water particle

(m = 1.33 + 0i, χ = 0.1) would look more like the dark solid line in Figure 3.4.
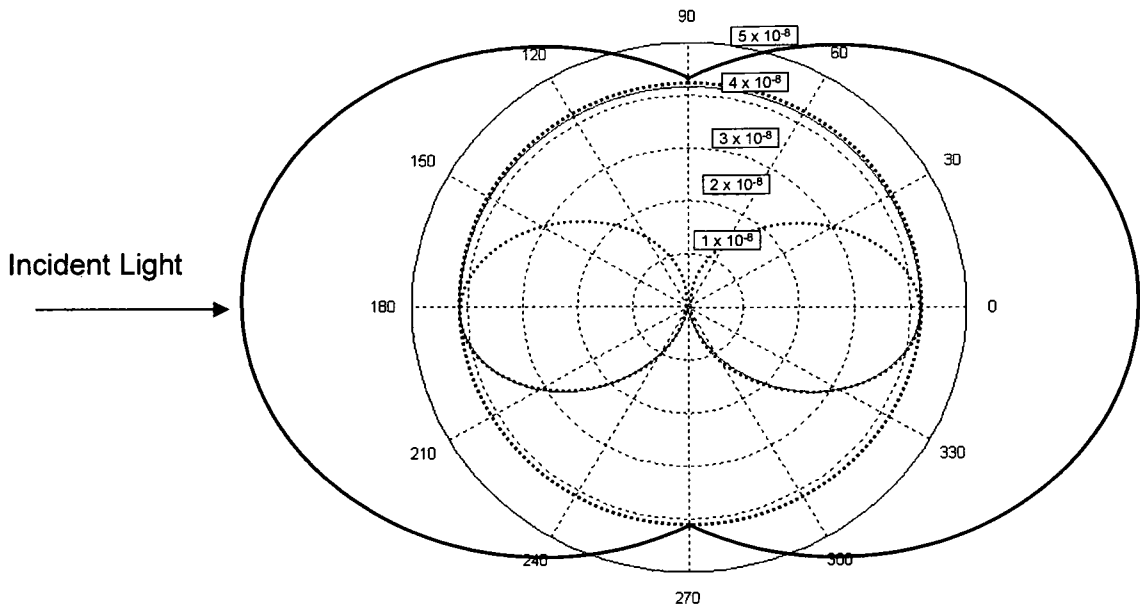
Figure 3.4. The total scattering of light polarized parallel and perpendicular to the scattering plane (heavy dotted lines) is shown as an overlay of the previous figure (m = 1.33 + 0i, χ = 0.1). The total scattering of parallel polarized light has a node in the middle shown by the inner barbell shape with a dotted line. The total scattering of perpendicularly polarized light does not have any nodes and the intensity is the same at all angles, shown by the circular shape outlined with a dotted line. The total scattering of un-polarized light is the sum of these scattering intensities, and is indicated by the solid black line.

The total 3-dimensional scattering profile of un-polarized light from a particle in the Rayleigh scattering regime would appear as the solid black line in Figure 3.4 rotated about the axis corresponding to 0 degrees, the direction of the incident light. The intensity of scattering in the forward and backward direction is the same, and exactly twice as intense as scattering at angles perpendicular to the incident light (90° and 270°). However, as χ increases, the intensity of light scattered in the forward direction increases, which can be seen in Figure 3.5.
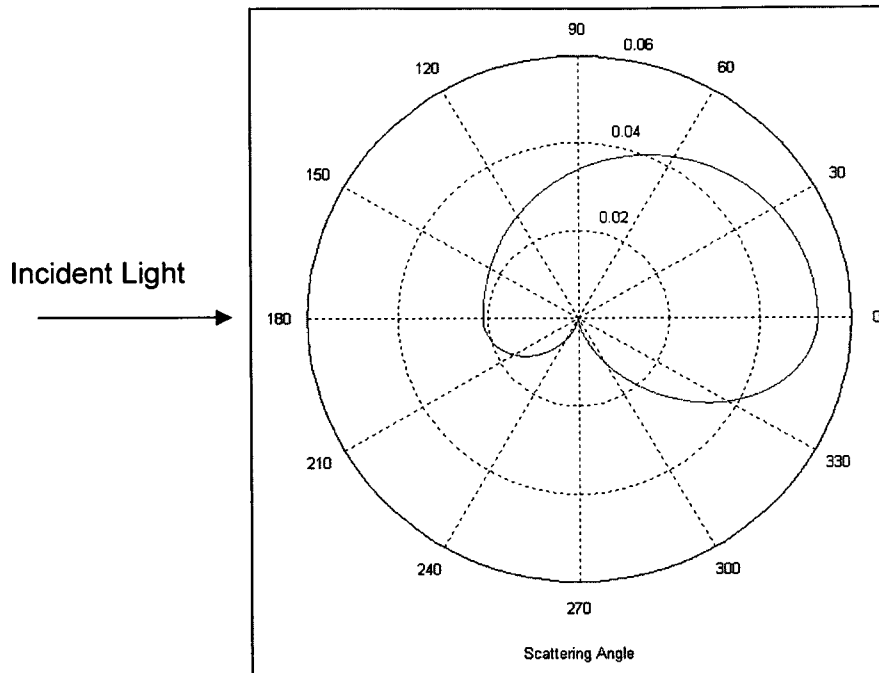
Figure 3.5. Scattering intensity in the forward direction increases as χ increases by an order of magnitude. The particle is no longer displaying the characteristics of Rayleigh scattering. This figure shows how scattering from a larger water droplet (m = 1.33 + 0i, χ =1.0) favors the forward direction.

As the diameter of a particle approaches or exceeds the wavelength of incident light, scattering in the forward direction becomes increasingly favored as shown in Figure 3.6(A). As the size of the particle increases so to does the complexity of the particle-light interaction. Figure 3.6 (B) is a magnification of the origin of 3.6 (A). A highly structured scattering distribution is seen, with discrete scattering lobes visible at multiple angles. This structure can be explained by geometrical optics, which indicates that the pattern is due to light exiting the particle after a number of internal reflections (refer to Figure 1.3). For droplets of water, these smaller scattering lobes are the reason a rainbow is sometimes visible on a rainy day. In this case, sunlight interacts with water droplets and is internally reflected. Most rainbows are the result of a single internal reflection and the wavelength dependence of the refractive index of water causes each wavelength of light to be refracted slightly differently, a phenomenon which manifests itself as the separate visible colors in the rainbow. On rare occasions a secondary

rainbow can be observed in nature when sunlight is internally reflected twice in the same water droplet.
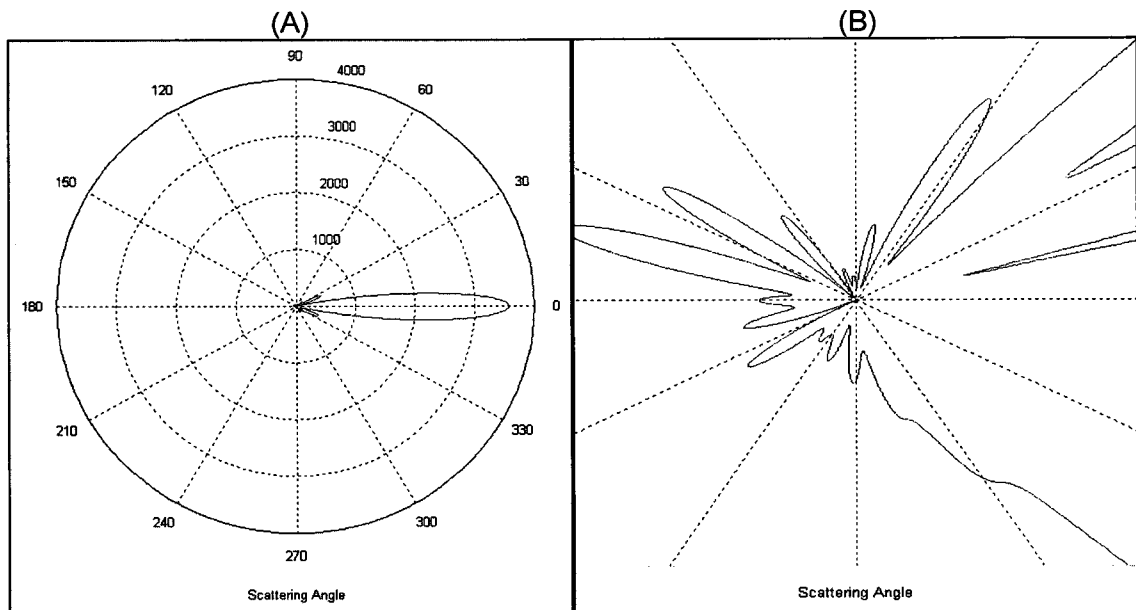
Figure 3.6. The incident light for both panel A and panel B originates at 180°. (A) Scattering in the near forward direction is favored as the diameter of the particle becomes larger than the wavelength of light (m = 1.33 + 0i, χ = 10). As χ increases the forward scattering lobe becomes confined to smaller angles in the forward direction. (B) A magnified version of the origin of panel A displays the structured scattering from a spherical particle larger than the wavelength of light. The result is due to the incident light exiting the particle after a number of internal reflections, as explained by geometrical optics.

Mie theory is also used to calculate the dimensionless efficiency with which particles scatter (Q_{sca}), absorb (Q_{abs}), or attenuate incident light (Q_{ext}). Extinction efficiency is given by,

$$Q_{ext} = \frac{C_{ext}}{G} \tag{3.3}$$

where C_{ext} is the extinction cross section (cm^2/particle), and G is the geometrical cross-sectional area of the particle (πr^2) for a particle of radius r. For particles that primarily attenuate light via scattering, the extinction efficiency is dominated by scattering, as Q_{ext} = Q_{sca} + Q_{abs}. The scattering efficiency of a particle reaches a maximum when the diameter of the particle is approximately the wavelength of light. This explains why accumulation mode aerosols are important when investigating atmospheric aerosol

optical properties. The sizes of these aerosols (~100 – 2500 nm) correspond to the

wavelengths of sunlight that reach the lower atmosphere (~350 – 2000 nm), and will

efficiently interact with sunlight (Bohren and Huffman 1983). An example of this is seen

in Figure 3.7.
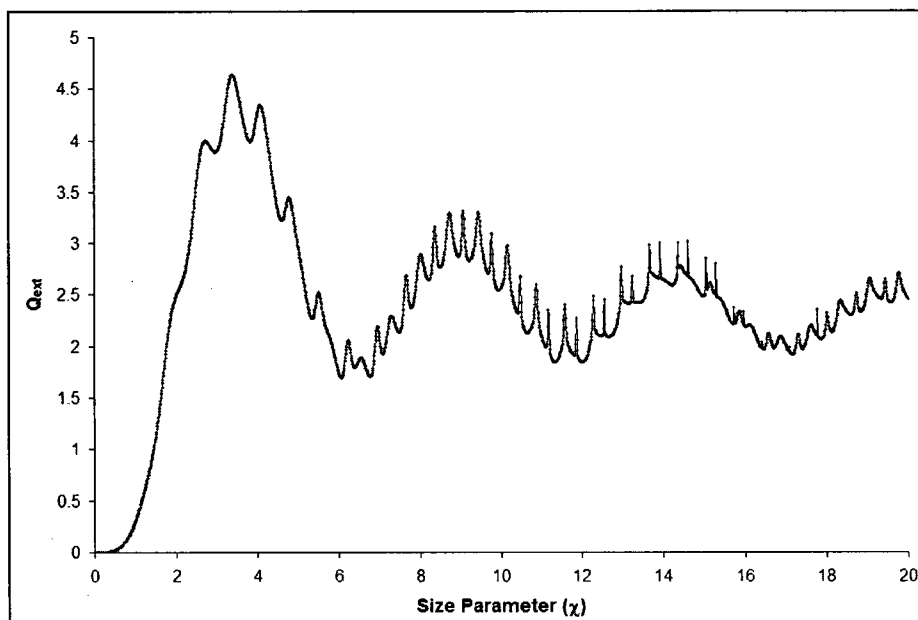
Figure 3.7. The calculation of scattering efficiency for an arbitrary spherical particle (m = 1.6 + 0i) shows that the maximum occurs when the diameter of the particle is approximately the wavelength of light, which corresponds to χ = 3.14. This particle does not absorb any incident light, therefore Q_{ext} = Q_{sca} and they can not be differentiated on this graph.

Particles with a negligible extinction coefficient (imaginary portion of the complex

refractive index), such as the one used in the calculation for Figure 3.7, have extinction

efficiencies equal to the scattering efficiency. Examples of particles with larger extinction

coefficients will be discussed in Chapter 4. The broad maxima and minima are called

interference structure and are due to constructive (maxima) or destructive (minima)

interference between rays of scattered light (Bohren and Huffman 1983). The smaller

sharp peaks in Figure 3.7 are referred to as ripple structure. The ripple structure

disappears for measurements made of a distribution of particle sizes, for particles that

absorb light, or if there is any dispersion in the wavelength of the light source. For these

reasons, ripple structure will not be important to this work, as it is unlikely to be

observed. The MATLAB program used to generate Figure 3.7 can be used at a lower resolution to "smooth" the ripple structure to make the calculations more applicable to this work.

Another feature of scattering efficiency observed in Figure 3.7 is that Q_{ext} and Q_{sca} approach 2 as χ increases to large values. A scattering efficiency of 2 means that the particle scatters twice as much light as is incident upon it. This counterintuitive notion can be explained by investigating how light interacts with the edges of the sphere. Electromagnetic waves passing by the sphere can just graze one of its edges and be deflected ever so slightly, which is still assumed to be scattered light. This is a simplified explanation, but the concept is tangential to this work and will not be discussed further.

Polystyrene Latex Spheres

Polystyrene latex spheres (PSLs) are often used in particle research as a proxy for highly scattering aerosols. PSLs are manufactured to be highly spherical with a very narrow size distribution. These particles are used because they interact with light as predicted by Mie theory, and therefore make a good calibration standard for aerosol measurement techniques (Galli, Guazzotti et al. 2001; Cai, Zelenyuk et al. 2006; Lang-Yona, Rudich et al. 2009; Liu, Romay et al. 2010).

The refractive index of PSLs is quoted by the manufacturer, Duke Scientific Corporation, to be 1.59 + 0.0i at 589 nm. However, this does not give an indication of the wavelength dependence of the complex refractive index of the PSLs, which will be discussed shortly. PSLs absorb very little light at visible wavelengths, but as wavelength decreases into the UV, the refractive index as well as the extinction coefficient of PSLs increases, and this must be taken into consideration when performing Mie calculations at multiple wavelengths (French, Winey et al. 2007).

Mie Calculations. Mie calculations using different sets of complex refractive

indices for PSLs were performed using a Fortran program based on the Mie calculation

program provided in Bohren and Huffman, 1983. The results of these calculations can

be seen in Figure 3.8. The first calculation was performed using a constant complex

refractive index (m = 1.590 + 0i, diamonds) at discrete wavelengths. The lines

connecting the points are used to guide the eye to approximate the extinction pattern

over the entire wavelength range. This calculation displays the variation in extinction

with wavelength, but without taking the wavelength dependence of the complex

refractive index into consideration. In reality, this is not accurate, as the complex

refractive index for most substances should only be constant over a small wavelength

range, but the results of the calculation are shown for the sake of comparison.
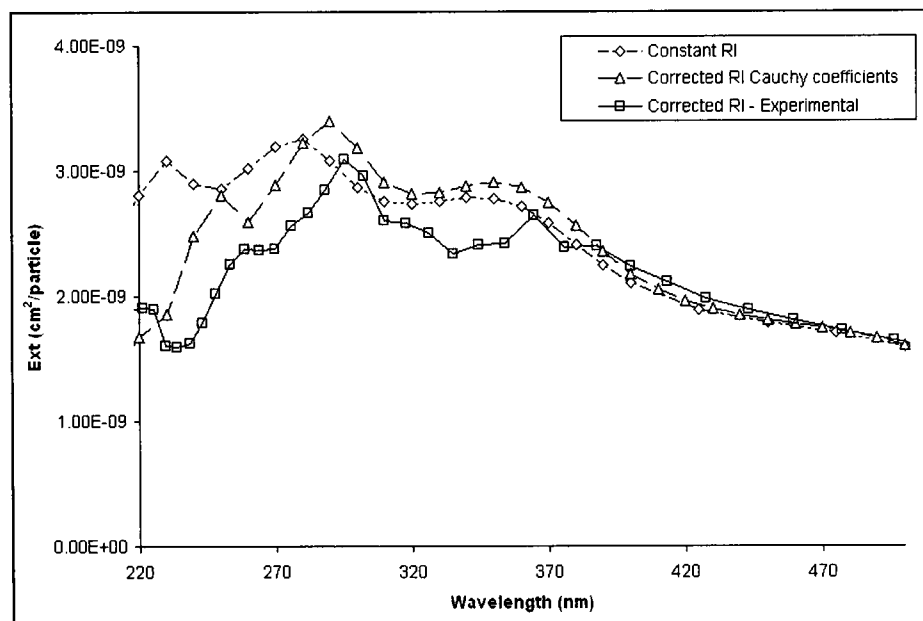
Figure 3.8. The results shown are for Mie calculations of PSLs using three different sets of
complex refractive indices (RI). The open diamonds are the result of calculations using a
constant refractive index (m = 1.590 + 0.0i). The open triangle are the result of calculations using
Cauchy coefficients from (Ma, Lu et al. 2003). The squares represent the result of Mie
calculations using complex refractive indices determined from a least squares fit to experimental
data as calculated in (French, Winey et al. 2007).

In reality, the refractive index increases as the wavelength of light decreases.

This trend is often analyzed with a least-squares fit in order to determine the dispersion

coefficients that fit Cauchy's equation (Nikolov and Ivanov 2000; Ma, Lu et al. 2003).
Cauchy's equation is given by,

$$n(\lambda) = A + \frac{B}{\lambda^2} + \frac{C}{\lambda^4} \qquad (3.4)$$

where n is the real part of the refractive index, λ is the wavelength of light in μm, and for the calculation shown in Figure 3.8 the Cauchy coefficients are A = 1.5725, B = 0.0031080 μm^2, and C = 0.00034779 μm^4 (Ma, Lu et al. 2003). The variation in the real part of the complex refractive index for PSLs using the coefficients listed above can be seen in Figure 3.9 (triangles). For this calculation it was assumed that the imaginary part of the complex refractive index was negligible. The wavelength range the Cauchy coefficients listed above are applicable for is 370-1610 nm. However, the coefficients were used to extrapolate the refractive index into the UV in order to provide data for the entire wavelength range of the A-DOAS.

Also displayed on Figure 3.8 as open squares are the results of Mie theory calculations using experimentally determined complex refractive indices for polystyrene using an ellipsometry technique (French, Winey et al. 2007). These experimental data show that the extinction coefficient of polystyrene is not negligible over the wavelength range of the A-DOAS, and there is part of an absorption peak that tails into this range at wavelengths less than approximately 240 nm. Therefore, the absorption of light by polystyrene in this wavelength range will influence the measured extinction of PSLs and must be considered when performing Mie theory calculations. The experimentally determined complex refractive indices of polystyrene, as measured by French, Winey et al. 2007, are displayed in Figure 3.9. These values were used to perform the PSL Mie theory calculations for the remainder of this work.
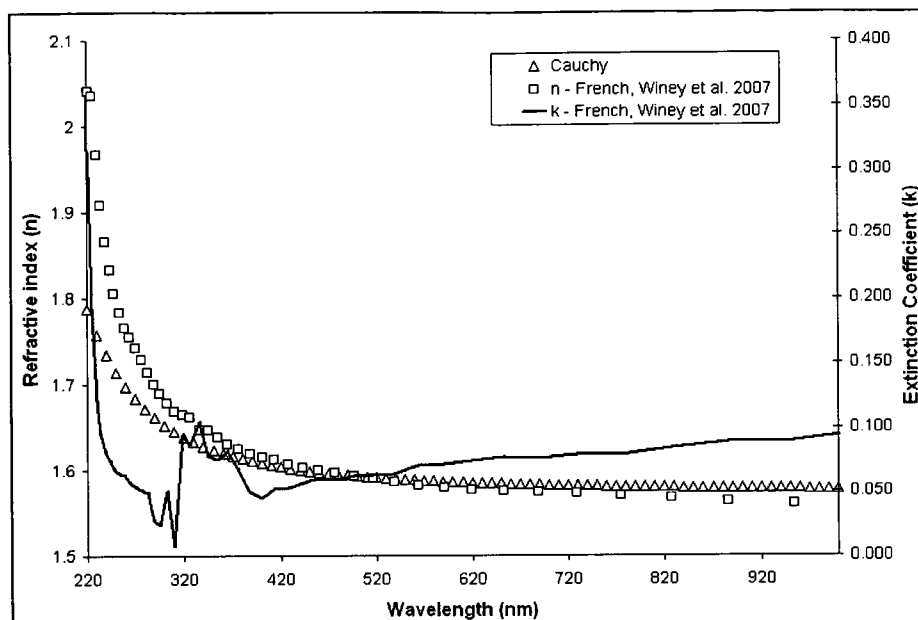
Figure 3.9. The wavelength dependent refractive indices for PSLs (triangles) using Cauchy coefficients determined by (Ma, Lu et al. 2003), and both the real (squares) and imaginary (solid black line) parts of the complex refractive index of polystyrene determined experimentally by (French, Winey et al. 2007). Note that different y-axes are given on the left and right sides of the figure.

PSL Extinction Measurements. All PSL solutions in this work were prepared in test tubes by diluting 15 drops of 10% w/w PSL solution (Duke Scientific Corporation) in 20 mL deionized water (J.T. Baker - HPLC Water). The size distributions of the stock PSL solutions are reported to range from ≤ 3% to ≤ 5%. Once created, the sample solutions were inverted multiple times to ensure adequate mixing, and solutions no more than 12 hours old were used for all experiments. In this work, a "measurement" refers to a single A-DOAS measurement of a sample, while a "trial" indicates a set of measurements of the same sample conducted consecutively on the same day using the same zero. Specific information regarding the PSLs used in this work is listed in Table 3.1, and the polystyrene and surfactant for all PSLs is assumed to be identical.

Table 3.1. All PSLs used in this work were purchased from Duke Scientific Corporation, which is now owned by Thermo Scientific. All stock PSL solutions are 10% w/w with the exception of the 150 nm PSLs (3150A) which are 1% w/w.

PSL Diameter (nm)	Catalogue Number	Lot Number	Size Distribution (CV)
150	3150A	36341	3.4%
220	HF22	36951	≤ 5%
300	HF30	36889	≤ 5%
300	5030A	36210	≤ 3%
430	5043A	36495	≤ 3%
600	5060A	32284	≤ 3%

PSLs solutions provide a very high concentration of spherical particles at one specific size, making it possible to measure the optical properties of a monodisperse PSL aerosol sample with the A-DOAS. It was then possible to compare the experimental data to Mie theory calculations. To measure a monodisperse PSL aerosol sample the setup in Figure 3.10 was used.
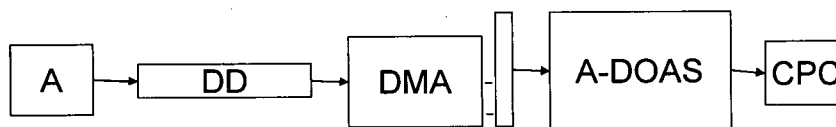
Figure 3.10. A flow diagram depicting experimental setup used to measure the optical properties of a monodisperse PSL sample with the A-DOAS. A = atomizer, DD = diffusion dryer, DMA = differential mobility analyzer, A-DOAS used for optical property measurements was described in detail in Chapter 2, and CPC = condensation particle counter.

The PSL sample was aerosolized with a collision type atomizer (A) (Liu and Lee 1975) with nitrogen as a carrier gas (Airgas – UN1066). To ensure a contamination free sample, the carrier gas was filtered (Swagelok - 0.5 μm filter #578041001) before the atomizer in order to remove any particles that may be in the compressed gas cylinder. The aerosol sample was then dried to a relative humidity of < 3% by flowing it over molecular sieves housed in a cylindrical stainless steel diffusion dryer (DD - residence time ~ 3 seconds). The dried aerosol sample was size selected, at the diameter of the PSLs, by a differential mobility analyzer (DMA – TSI model 3080L). The DMA uses a radioactive source to neutralize charges on the sample aerosols (McMurry 2000). The aerosols exit the neutralizer with a known charge distribution, and enter a column with

an electrode in the center. To create a monodisperse aerosol sample, the charge on the column is held constant and sample flows are controlled so that only particles of the desired mobility size can exit the column. The PSL aerosol exits the column as a monodisperse sample and then enters the A-DOAS gas cell. The A-DOAS continuously makes extinction measurements as the PSL sample flows through the gas cell. Upon exiting the gas cell, the aerosol sample enters the condensation particle counter (CPC - TSI model 3775). The CPC cools the aerosol sample in a chamber with butanol vapor, initiating the condensation of butanol onto the surface of the aerosol. This increases the diameter of the particles, allowing them to be optically counted by the detector. The uncertainty of the counted particle concentrations for size selected particles is ±10% (TSI Model 3775 CPC Operation and Service Manual).

Another likely source of error for PSL experiments is the process of correlating the correct particle concentration to each A-DOAS measurement. The particle concentration varies over time and is not measured at the exact moment the A-DOAS data is recorded. Estimates of the time offset between measurements can be calculated based on the volume of the gas cell and tubing as well as the sample flow rate for each experiment. However, since the internal volume of the gas cell is not exactly known, and the length of tubing used may change between experiments, another method for estimating the particle concentration of each A-DOAS measurement was devised.

All A-DOAS measurements for an experiment are compared and the measurement with the highest extinction is assumed to correspond to the maximum particle concentration for the experimental trial. The time offset is defined as the difference between the start time of the A-DOAS measurement with the highest extinction and the time the maximum concentration was measured by the CPC. For all PSL measurements discussed in this work the time offset from the A-DOAS measurement to the particle concentration measurement was between 8.5-10.5 minutes.

This time offset is then used to determine the particle concentration of the other A-DOAS measurements in the same configuration. For example, if the time offset if found to be 10.5 minutes then a single A-DOAS measurement made from 12:00:00 to 12:01:30 will correlate to the average particle concentration measured by the CPC from 12:10:30 to 12:12:00. The remaining work in the chapter shows that the A-DOAS accurately measures the extinction of highly scattering aerosols despite the possible error associated with correlating the A-DOAS measurements with the correct particle concentration.

Experimentally obtained data for 300 nm PSLs is shown in Figure 3.11, along with the Mie theory calculation results that were given in Figure 3.8. In this case, the A-DOAS data (solid diamonds) is an average of three trials, and the error bars represent one standard deviation of the mean. All experimental data shown in Figure 3.11 were measured at a sample path length of 19.51 meters. Additional PSL extinction measurements performed at multiple path lengths (not shown) yielded similar results. Mie calculations performed using Cauchy coefficients (triangles) fail to accurately represent the measured optical properties of 300 nm PSLs. Mie theory calculations (squares) performed with the experimental complex refractive indices from (French, Winey et al. 2007) and acquired via personal communication with Dr. Roger French correlate more closely with measured extinction cross sections, especially at wavelengths less than 300 nm.
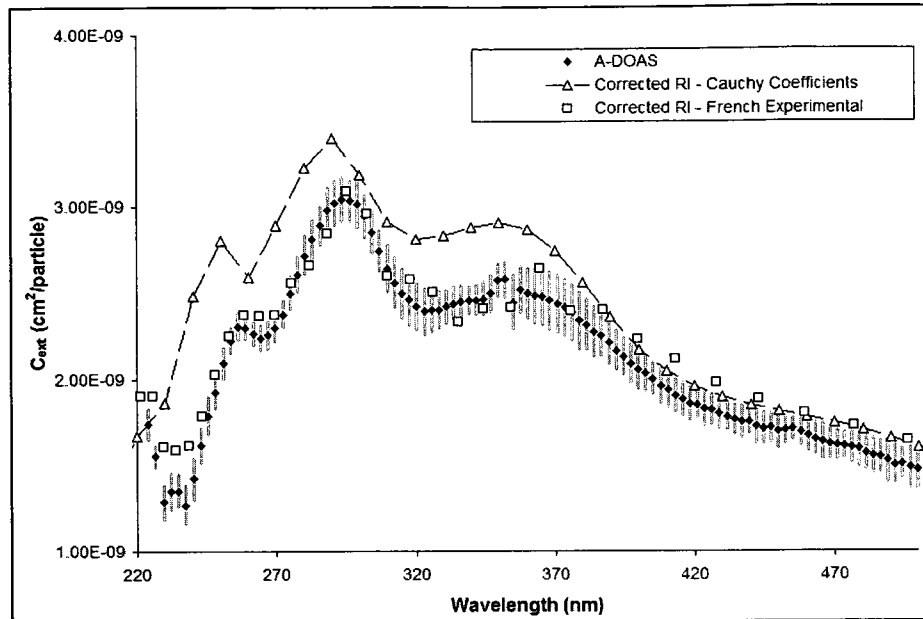
Figure 3.11. Measured 300 nm PSL extinction cross sections are compared to Mie theory calculations. The error bars represent 1σ of the mean for experimentally determined extinction cross section at that wavelength. The calculations converge at wavelengths greater than 500 nm (not shown) where scattering is the major extinction processes and the refractive indices are less variable. Mie theory calculations performed with experimentally measured complex refractive indices (squares) (French, Winey et al. 2007) correlate well with the measurements for wavelengths less than 300 nm, whereas other model attempts do not agree as well.

The A-DOAS data displayed in Figure 3.11 represent the average (N = 11) C_{ext} measured during three different trials over the course of 3 weeks. There was approximately 1 week between each trial and two different varieties of 300 nm PSLs listed in Table 3.1 were used. An average of 10 data points was used to represent each A-DOAS wavelength shown in Figure 3.11 in order to smooth the data. For example, the data at shown at 223.9 nm is the average of 10 measured data points between 222.7011 and 225.1267 nm. This smoothing technique was not used to create all graphs shown in this work. The experimental data appears to be well represented by the Mie calculations conducted with the experimentally measured complex refractive indices of polystyrene from French, Winey et al. 2007. However, there are areas where the theoretical and experimental data vary. The Mie theory calculations predicted higher extinction cross sections from 230-240 nm than were measured by the A-DOAS. Differences between the predicted and measured extinction cross section peak in the

61

wavelength range of approximately 300-370 nm can also be seen. The theoretical 300 nm PSL extinction cross sections also appear to be greater than the experimentally determined values at wavelengths greater than 400 nm, suggesting that more light is reaching the A-DOAS detector than is predicted by Mie theory.

Experiments using PSLs at multiple sizes (other than 300 nm) were performed and the experimentally measured extinction was compared to Mie theory calculations to further investigate the differences seen when comparing experiment and theory for 300 nm PSLs. The smallest PSL diameter measured was 150 nm. It was possible to achieve size-selected particle concentrations of greater than 10,000 particles/cm^3 with these PSLs. As previously mentioned, small particles efficiently attenuate light at short wavelengths, which can be observed in the extinction spectra of the 150 nm PSLs (Figure 3.12). The extinction peak of these particles is in the UV and decreases significantly at longer wavelengths. Figure 3.12 is truncated at a wavelength of 500 nm for clarity because the extinction signal at longer wavelengths is not greater than the noise of the A-DOAS. This is due to low lamp intensity in this region and the small extinction cross section of 150 nm particles at wavelengths much longer than the diameter of the particles. Mie theory calculations correlate well with the experimental data except for the area of approximately 300-360 nm. As discussed in Chapter 2, the light intensities measured by the A-DOAS in this region of the spectrum are susceptible to slight pressure changes, which may account for the difference between the measured and theoretical extinction. However, it is also possible that the complex refractive indices used to perform the Mie theory calculations shown in Figure 3.12 are not completely representative of the PSLs used in this work; this may be due to the specific variety of polystyrene used and/or the surfactant added to PSLs to limit agglomeration, which may cause the optical properties to differ from the sample used by French, Winey

et al. 2007. Pressure peaks have been minimized, so more evidence for the variable complex refractive index will be shown in the following.
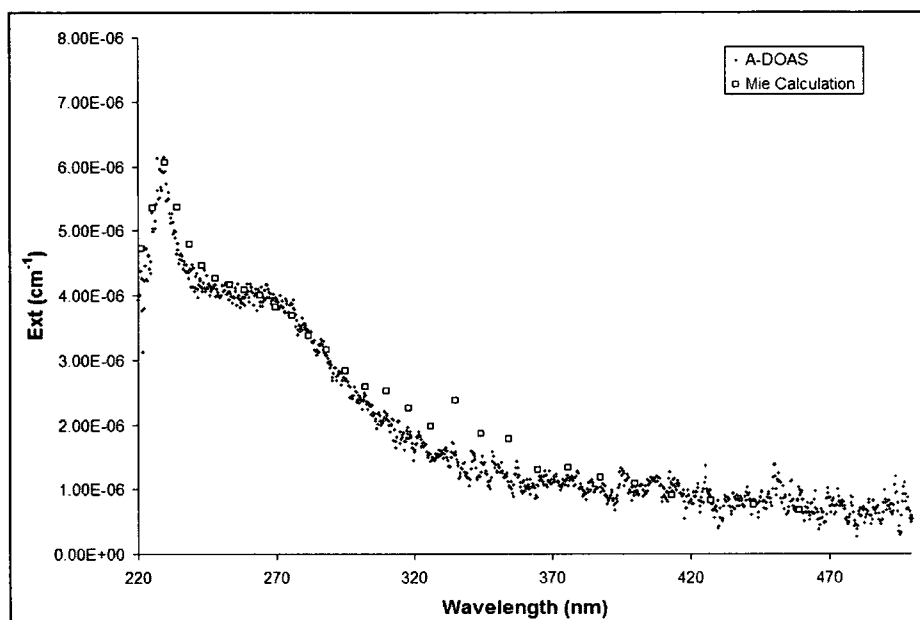
Figure 3.12. Mie theory calculations for a single measurement correlate well with the experimental extinction of 150 nm PSLs (7318 ± 86 particles/cm^3). There is a region from approximately 300-360 nm where the experimental and theoretical extinction deviate from each other. This could be due to one of two reasons: (1) a slight pressure change in the gas cell caused erroneous experimental data in the region or (2) the complex refractive indices used in the Mie theory calculations are not exactly the same as the particular polystyrene used in these experiments.

The next PSL diameter investigated was 220 nm. The results from these measurements are shown in Figure 3.13. The PSL figures from this point forward will display the entire wavelength range of the A-DOAS. The correlation with Mie theory calculations performed using the wavelength dependent complex refractive indices from French et al. 2007 was very good. However, the discrepancy in the wavelength range from 300-360 nm is seen again. The same reasons may cause this difference. In the case of the 220 nm PSLs, there are two additional regions where the measured extinction and Mie theory diverge, specifically at 220 nm and between 280-290 nm. At 220 nm the measured extinction is lower than the calculated extinction, meaning more light of this wavelength reached the detector than was theoretically predicted. Over the range of approximately 280-290 nm the experimentally determined extinction is greater

than the Mie theory predictions. The difference between the experimental and theoretical extinction in these wavelength ranges is not drastic, but enough to suggest that the complex refractive indices previously discussed may not accurately represent this sample of PSLs at all wavelengths. Because the deviations for 220 nm PSLs are not all in the same direction, this is evidence that simple pressure variations are not the cause for the discrepancies between the experimental and theoretical extinction. A pressure peak would cause deviations from Mie theory calculations over a much broader range of wavelengths (see Figure 2.11).
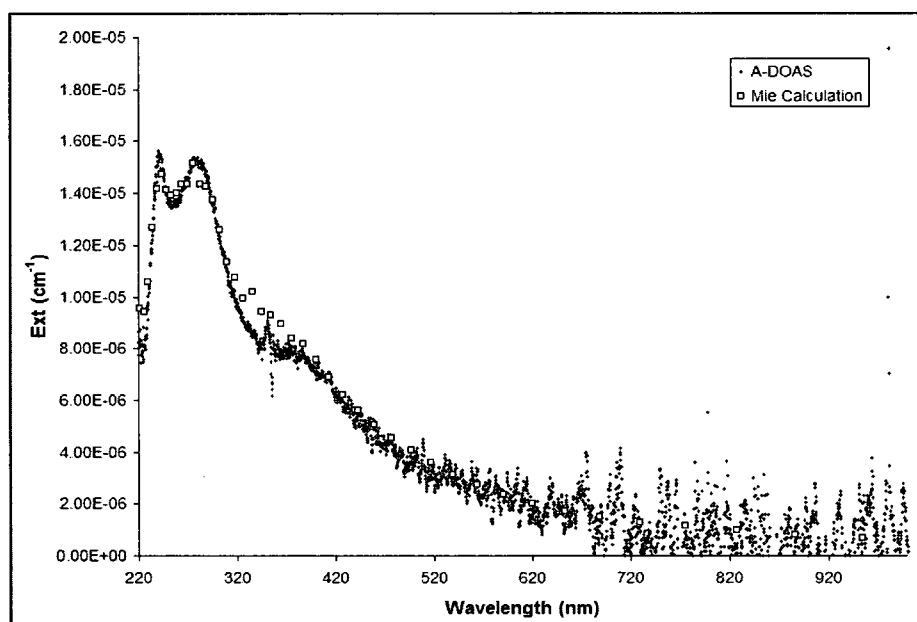
Figure 3.13. Extinction measured for 220 nm PSLs correlate well with Mie theory calculations (9337 ± 97 particles/cm^3). There are discrepancies between the theory and experiment around 300-360 nm, as well as at 220 nm and between 280-290 nm.

The experimental results and comparison to Mie theory calculations for 300 nm PSLs can be seen in previously discussed Figure 3.11. The next largest diameter of PSLs used was 430 nm. The results of this experiment are displayed in Figure 3.14. As the size of the PSLs increases the correlation between the experimental and theoretical data seems to decrease. Once again, the match from 300-360 nm is poor. The difference in this wavelength range in Figure 3.13 can be seen as a broad decrease from 300-360 nm, but the peak in Figure 3.14 is distinct. It is clear that the peak measured by

the A-DOAS at 340 nm (Figure 3.14 - shown within a box) is inverted compared to the peak predicted by Mie theory. This is not likely to be due to a slight pressure change in the gas cell because a pressure change produces a broad increase or decrease in extinction, not a distinct peak. Rather, this suggests that the complex refractive indices for polystyrene used in the model are not representative of the sample used. Figure 3.14 also shows additional discrepancies between the experimental and theoretical extinction at 220 nm, between 250-280 nm, and between 380-420 nm, all of which indicate a difference between the PSLs and the polystyrene sample used by French, Winey et el. 2007.
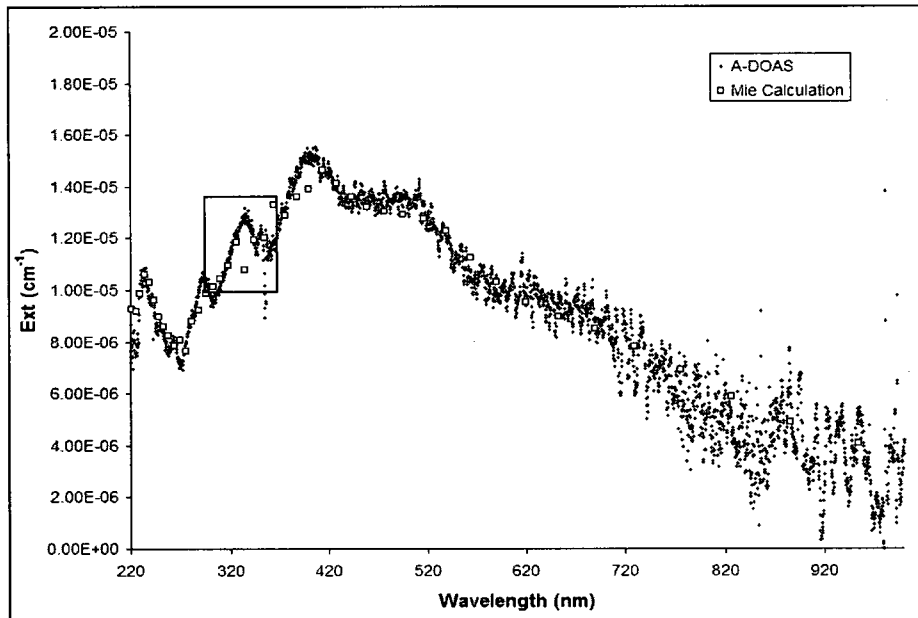
Figure 3.14. The experimentally measured extinction of 430 nm PSLs (2522 ± 50 particles/cm^3) provides further evidence that the complex refractive indices calculated by (French, Winey et al. 2007) for polystyrene may not represent the PSL samples for these experiments. Small discrepancies between Mie theory calculations and measured extinction can be seen from approximately 220-430 nm.

The largest PSLs measured with the A-DOAS were 600 nm in diameter. Figure 3.15 shows how the experimentally measured extinction varies from the results of Mie theory calculations. The most obvious difference is the extinction offset seen at wavelengths less than 400 nm. The measured PSL extinction at approximately 330 nm is significantly less than the extinction predicted by Mie theory. This deviation between

the theoretical and experimental values clearly illustrates the difference between the polystyrene sample used by French, Winey et al. 2007 and the polystyrene spheres used in this work.

Prior to the comparison between the 600 nm PSL experimental and theoretical extinction, the experimental data indicated that the complex refractive indices from French, Winey et al. 2007 that were incorporated into Mie theory for this work were not identical to the optical constants of PSLs used here. However, a specific reason for the difference was not obvious. When comparing the extinction of 600 nm PSLs in Figure 3.15 to the graph of the extinction coefficient used in the Mie calculations (open circles - solid black line) it can be seen that the wavelength range where the greatest deviation between the experimental and theoretical extinction (300-400 nm) occurs corresponds to a secondary absorption peak measured by French, Winey et al. 2007. It is possible that while the polystyrene sample used by French, Winey et al. 2007 absorbs in this wavelength range, but the PSLs used here do not. This would likely result from differences in manufacturing processes of the polystyrene samples.
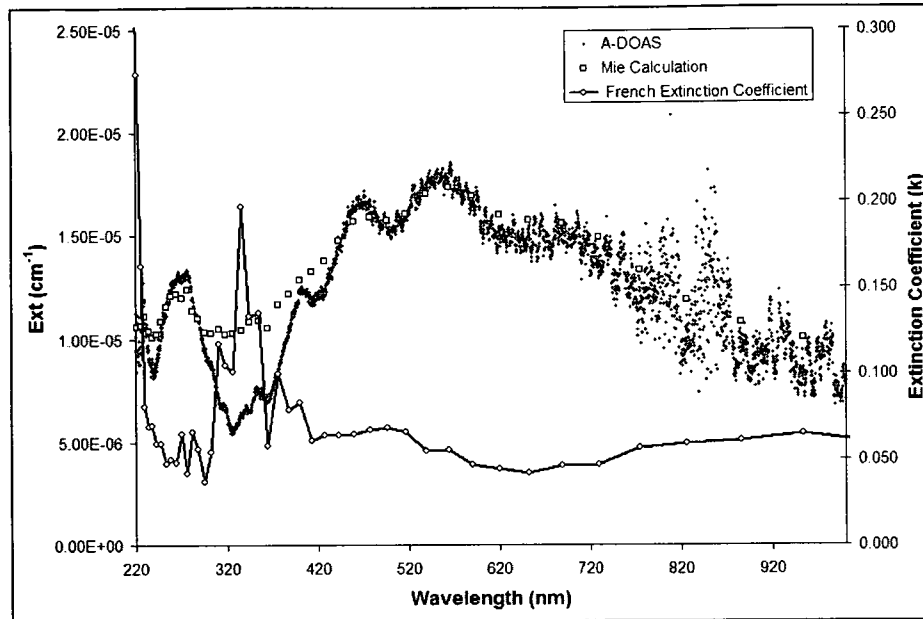
Figure 3.15. Experimental measurements of 600 nm PSLs (915 ± 31 particles/cm^3) indicate that the peaks do not occur in the same places as predicted by Mie theory calculations. This can be seen in the data at wavelengths less than 400 nm where the peaks do not match. The extinction coefficient used to perform the Mie theory calculations is plotted on the right y-axis. This shows that an absorption peak measured for the polystyrene sample used by French, Winey et al. 2007 is located in the same wavelength range as the greatest discrepancy between the experimental and theoretical extinction of 600 nm PSLs.

PSL Extinction Efficiency. It is possible to calculate the extinction efficiency of PSLs using A-DOAS measurements and compare the results to Mie theory. However, a separate Mie calculation of Q_{ext}, Q_{sca}, and Q_{abs}, versus the size parameter must be performed for each wavelength of light due to the frequency dependence of the complex refractive index. An example is shown in Figure 3.16 using the calculated Mie theory efficiency results for PSLs at 248 nm with the French complex refractive index at that wavelength (m = 1.826 + 0.059i) (French, Winey et al. 2007). A wavelength of 248 nm was chosen for this calculation because Mie theory calculations appear to correlate well with the extinction measurements at this wavelength, and there is minimal lamp noise at 248 nm. The A-DOAS results for the average measured Q_{ext} (at 248 nm) for 150, 220, 300, 430, and 600 nm PSLs are shown as open circles. The measured data fall close to the calculated Q_{ext}, and the theoretical trace is within 1σ (error bars) for all cases.
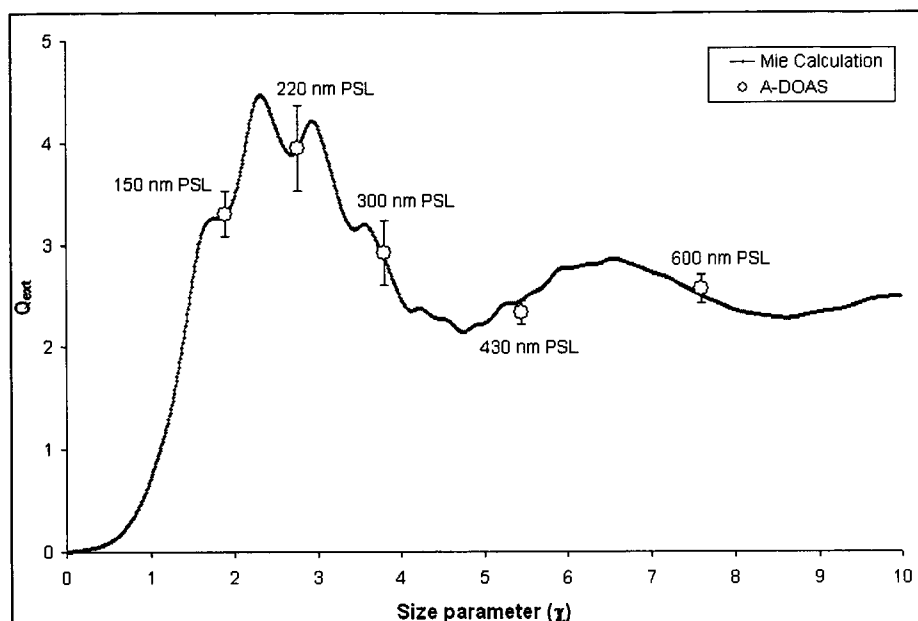
Figure 3.16. The A-DOAS Q_{ext} of PSLs are plotted against Mie theory calculations performed with a complex refractive index obtained from (French, Winey et al. 2007) (m = 1.826 + 0.059i at a wavelength of 248 nm). Calculations were performed in MATLAB and the data were exported to and graphed in Excel. The black line is Q_{abs}, the lightest line is Q_{sca}, and Q_{ext} is the sum of Q_{abs} (lower dark line) and Q_{sca}. All of the A-DOAS extinction efficiency values are within 1σ of theoretical values.

Figure 3.16 shows that the experimental extinction efficiency of PSLs as measured by the A-DOAS correlate well with the extinction efficiency calculated by Mie theory at 248 nm. This was to be expected as Figures 3.11 to 3.15 show that Mie theory using the complex refractive indices reproduce the A-DOAS extinction measurements at wavelengths close to 248 nm. However, Figures 3.11 to 3.15 also show that the complex refractive indices used in Mie theory calculations do not do a good job predicting the measured extinction near 335 nm. Therefore, the experimental and theoretical extinction efficiencies at this wavelength were not expected to coincide (Figure 3.17), and they do deviate more than at 248 nm.
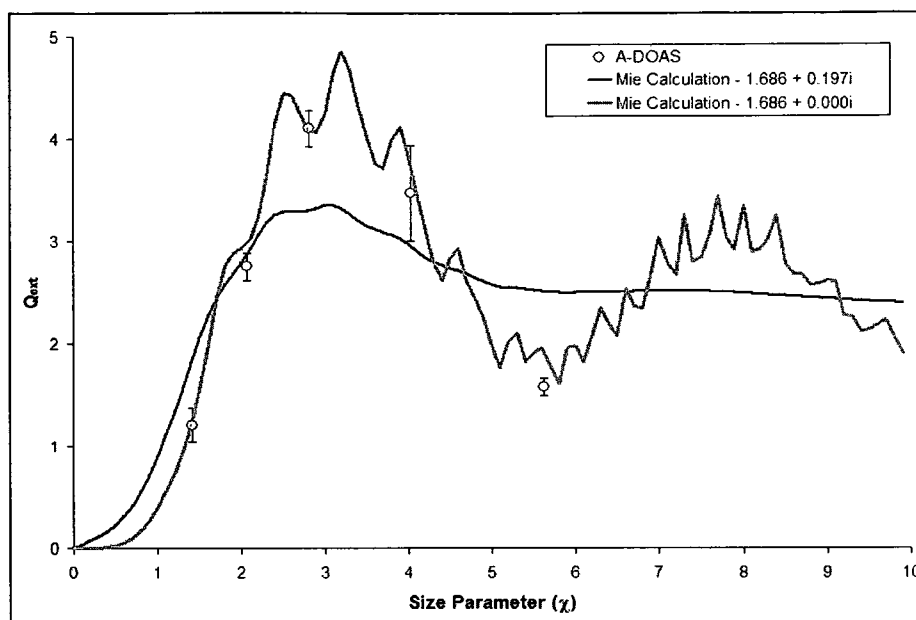
Figure 3.17. The graph of Q_{ext} measured by the A-DOAS (open circles) does not match the Q_{ext} predicted by Mie theory using the complex refractive index measured by French, Winey et al. 2007 at 335 nm, m = 1.686 + 0.197i (Black line), within the errors bars (1σ). However, if the extinction coefficient of this complex refractive index is reduced to zero, the resulting Q_{ext} predicted by Mie theory (gray line) more accurately predicts the experimental Q_{ext} across all size parameters. A smoothing routine was not used for either data set.

Figure 3.17 is further evidence that the polystyrene used by French, Winey et al. 2007 is not identical to the polystyrene used in this work. The Q_{ext} predicted by Mie theory using m = 1.686 + 0.197i (French, Winey et al. 2007) does not correlate well to the experimental Q_{ext} measured by the A-DOAS. Figure 3.15 clearly shows that the wavelength range of greatest deviation between the experimental and theoretical extinction occurs where French, Winey et al. 2007 measured an absorption peak in their polystyrene sample between 300 – 400 nm. This observation motivated a reduction in the extinction coefficient to zero so m = 1.686 + 0.000i, and then the theoretical Q_{ext} calculation was performed again. The results of this calculation are plotted as the gray line in Figure 3.17, and correlate strongly with the experimental Q_{ext}. This suggests that the Duke Scientific PSLs samples do not absorb light at this wavelength as readily as the polystyrene samples measured by French, Winey et al. 2007.

69

Some differences between the optical properties of various polystyrene samples are expected, as the manufacturing process can change. French, Winey et al. 2007 measured two different thin film polystyrene samples in their work, and the calculated complex refractive indices were unique to each sample. The PSLs used in the A-DOAS work are spherical, not thin films, and also contain a proprietary surfactant in the PSL solution to reduce agglomeration. Therefore, it is not unexpected that the complex refractive indices determined in French, Winey et al. 2007 do not completely reproduce the extinction spectrum of the PSLs used in this work. However, these wavelength dependent complex refractive indices are currently the best available and should continue to used, but with caution in the noted wavelength regions.

The work in this chapter shows that the A-DOAS is capable of accurately measuring the extinction of highly scattering laboratory generated PSL aerosols across a wide wavelength range. Figures 3.16 and 3.17 also revealed another valuable use for the A-DOAS. Figure 3.17 in particular shows that the A-DOAS can be used to measure extinction at specific particle sizes and the results can be used to determine the extinction efficiency. Mie theory can then be used to fit a complex refractive index to extinction efficiencies at specific wavelengths (Spindler, Riziq et al. 2007). Existing instruments can do this at a single wavelength, or perhaps a few discrete wavelengths, but not over the wavelength range that the A-DOAS measures (Lack, Lovejoy et al. 2006; Riziq, Erlick et al. 2007; Lang-Yona, Rudich et al. 2009). This concept will be discussed further in Chapter 4.

CHAPTER 4

EXTINCTION OF HIGHLY ABSORBING AEROSOLS

Nigrosin Dye

Soot formed during incomplete combustion processes is responsible for the

majority of atmospheric aerosol absorption, but soot particles are irregularly shaped

(Schnaiter, Horvath et al. 2003; DeCarlo, Slowik et al. 2004; Slowik, Stainken et al.

2004; Moosmuller, Chakrabarty et al. 2009). The aspherical nature and highly variable

composition of soot particles makes it difficult to complete closure studies comparing Mie

theory to aerosol absorption measurements. Nigrosin dye is a water soluble organic

dark purple/black dye that is used as a laboratory proxy for highly absorbing aerosols.

The molecular formula for nigrosin is not well characterized or regulated by

manufacturers but it can be approximated as $C_{48}N_9H_{51}$. Nigrosin forms spherical

particles (Lack, Lovejoy et al. 2006) when atomized and is therefore commonly used to

characterize the capability of aerosol optical measurement techniques.

There are various ways nigrosin can be used to verify instrumental performance.

One method is to measure nigrosin extinction at multiple particles sizes. This method,

similar to that described at the end of Chapter 3, has been used with single wavelength

(532 nm) CRD-AES and PAS measurements (Lack, Lovejoy et al. 2006; Dinar, Riziq et

al. 2008; Lang-Yona, Rudich et al. 2009), as well as with a white light optical particle

counter (400-700 nm) (Flores, Trainic et al. 2009). Mie theory is then used to fit a

complex refractive index to the nigrosin extinction versus particle size data. The results

are normally compared to previous measurements of the complex refractive index of

nigrosin (Garvey and Pinnick 1983) and a refined complex refractive index may be

obtained. This procedure is used to characterize instrumental performance for accurately measuring the extinction of a highly absorbing aerosol, and its ability to determine the optical properties of a homogeneous aerosol sample.

The use of nigrosin dye in this experimental work is more advanced than mentioned above. The necessary concentrations of size selected nigrosin particles for detection with the A-DOAS could not be achieved when nigrosin experiments were first performed. Therefore, the A-DOAS was used to measure the extinction of the entire size distribution of nigrosin particles, where an example of the atomizer generated size distribution is depicted in Figure 4.1. The extinction of the polydisperse nigrosin samples was well above the detection limit of the A-DOAS. However, comparing the extinction measurements for a polydisperse sample of particles over a large range of wavelengths to Mie theory is much more involved than comparing size selected measurements at a single wavelength.
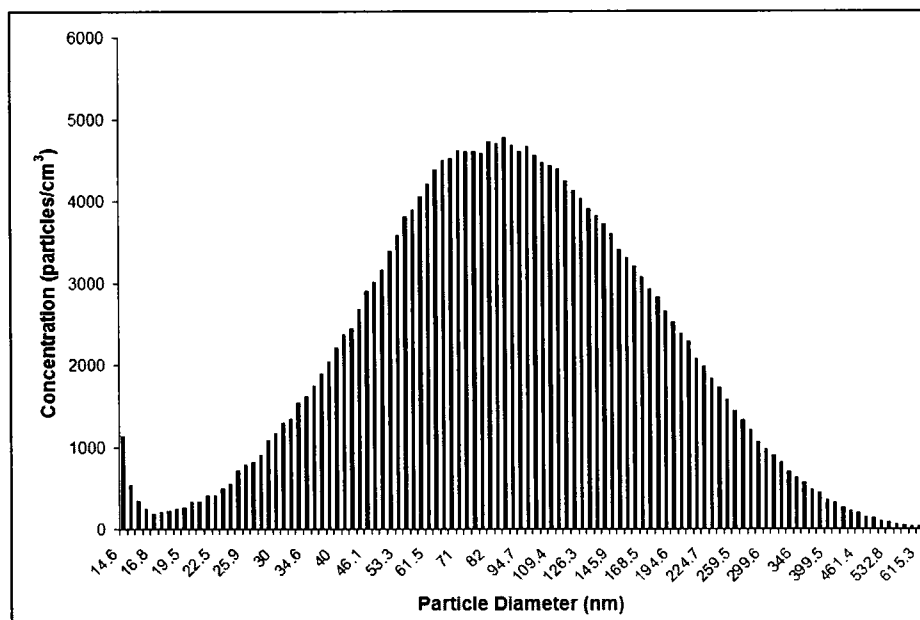
Figure 4.1. An SMPS scan of atomized aqueous nigrosin dye exiting the A-DOAS gas cell shows that the concentration peak of the lognormal distribution occurs at approximately 88 nm. The extinction of the entire size distribution must be measured. Size selecting particles generated in the same manner did not initially provide particle concentrations great enough to exceed the detection limit of the A-DOAS.

Extinction Coefficient Calculation

Experimental nigrosin data can be compared to the exact solutions of Mie theory. This is useful when the instrument used measures extinction of one particle size at a time and at one wavelength. Mie theory calculations for this scenario only require one complex refractive index, and for 532 nm this value is readily available in the literature (Garvey and Pinnick 1983; Lack, Lovejoy et al. 2006; Dinar, Riziq et al. 2008; Flores, Trainic et al. 2009; Lang-Yona, Rudich et al. 2009). As discussed in Chapter 3, the use of a single complex refractive index over a range of wavelengths is not realistic, especially for nigrosin dye which has distinctive absorption peaks as seen in Figure 4.2. Therefore a method for estimating the complex refractive index of nigrosin at many wavelengths was needed.
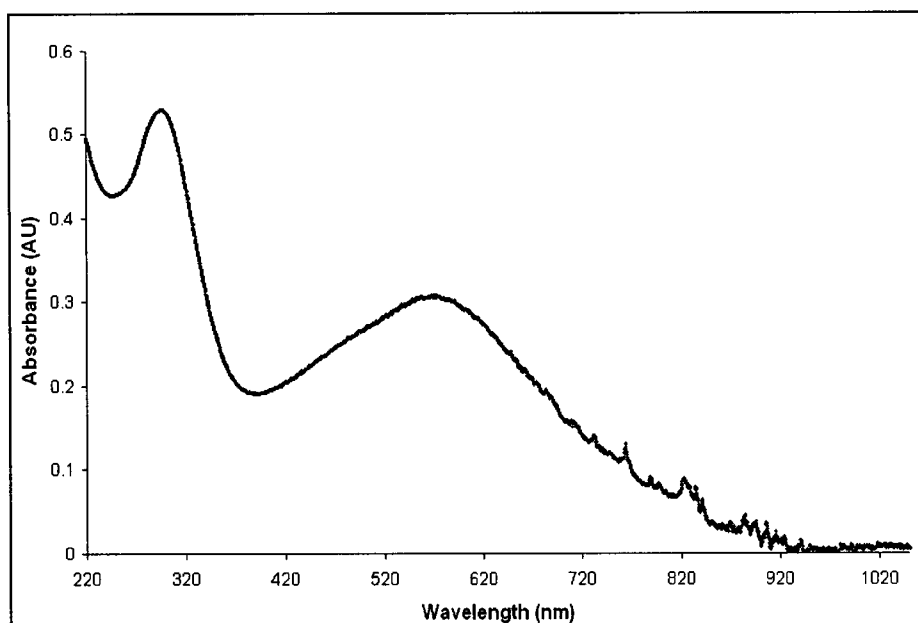
Figure 4.2. The absorbance spectrum of a dilute nigrosin dye solution (2 µg/mL) measured in a 1 cm quartz cuvet with the A-DOAS liquid cell attachment. The fine structure from 700-900 nm is due to lamp noise.

The wavelength dependent extinction coefficient (k) of the complex refractive index can be calculated for a bulk organic liquid using its absorbance spectra. The absorption coefficient is related to the measured absorbance through

$$\frac{\alpha(\lambda)}{\rho} = \frac{1000\ln(10)A(\lambda)}{cL} \tag{4.1}$$

where $\alpha(\lambda)$ is the wavelength dependent absorption coefficient (cm^{-1}), ρ is the density of the dissolved organic species (g/cm^3), $A(\lambda)$ is the measured absorbance at wavelength λ, c is the concentration of the solution (g/L), L is the path length through the sample (cm), and the 1000 is a unit conversion factor (Sun, Biedermann et al. 2007). The extinction coefficient is related to the absorption coefficient by

$$\alpha = \frac{4\pi k}{\lambda} \tag{4.2}$$

where α is the absorption coefficient calculated with equation 4.1, k is the desired extinction coefficient, and λ is the wavelength of light in cm.

This method was used to calculate the wavelength dependent extinction coefficient for nigrosin. However, nigrosin dye is poorly characterized and its density was not available. Therefore, the density of Rhodamine 6G laser dye (1.26 g/cm^3) was used as a starting point to perform the calculation. The extinction coefficient k, the imaginary part of the complex refractive index, calculated at 532 nm was compared to values from the literature, 0.31i (Lack, Lovejoy et al. 2006), 0.28i (Lang-Yona, Rudich et al. 2009), 0.26i (Garvey and Pinnick 1983), and 0.24i (Dinar, Riziq et al. 2008). It was found that the calculated extinction coefficient from the nigrosin absorbance spectra at 532 nm (0.22i) was lower than expected, which indicated the assumed density for the dye was incorrect. A reverse calculation to find the density of nigrosin was performed for 532 nm by setting k equal to the average of the literature values. The calculated density was found to be 1.47 g/cm^3, which was then used to calculate extinction coefficients of nigrosin for the wavelength range of 220-1050 nm.

The accuracy of the calculated nigrosin k values was verified by comparing the average extinction coefficient from 380-780 nm (0.19i) to experimental measurements

over the same wavelength range (0.20i ± 0.03i) (Flores, Trainic et al. 2009). The

technique used by Flores et al. 2009 uses a broadband white light source, but a

wavelength dependent complex refractive index was not determined. Therefore the

complex refractive index reported by Flores et al. 2009 is the "average" complex

refractive over the entire spectrum. These data are in good agreement and it was

concluded that the extinction coefficients calculated using the method described above

are acceptable for use in Mie theory calculations.

<u>Refractive Index Calculation</u>

The real part of the complex refractive index also varies with the wavelength of

light and must be calculated over the entire wavelength range of the A-DOAS. There is

no equation that allows for the direct calculation of this value with the instrumental data

available. Therefore, the Sellmeier coefficients for materials with similar real refractive

indices at 532 nm were used to calculate the real part of the refractive index for nigrosin

dye. The Sellmeier equation, which describes the empirical relationship between the

refractive index and wavelength, is given by

$$n^2(\lambda) = 1 = \frac{B_1\lambda^2}{\lambda^2 - C_1} + \frac{B_2\lambda^2}{\lambda^2 - C_2} + \frac{B_3\lambda^2}{\lambda^2 - C_3} \qquad (4.3)$$

where n is the real part of the complex refractive index, B is a unitless Sellmeier

coefficient, C is a Sellmeier coefficient (μm^2), and λ is the wavelength of light (μm).

Literature vales of n for nigrosin at 532 nm were used as a starting point for this

calculation, 1.72 (Lang-Yona, Rudich et al. 2009), 1.70 (Lack, Lovejoy et al. 2006), 1.67

(Garvey and Pinnick 1983), and 1.65 (Dinar, Riziq et al. 2008). The average of these

values (1.69) was compared to the refractive index of various glass materials in a Schott

Glass catalogue where the closest wavelength for which data was available was 546.1

nm. The Sellmeier coefficients for glass samples with similar refractive indices to

nigrosin are listed in Table 4.1.

Table 4.1. The Sellmeier coefficients of various glass materials (Schott Glass) with similar real refractive indices to nigrosin at 546.1 nm were used to calculate average values (bold). The average values were then used to calculate the wavelength dependent refractive index of nigrosin.

Glass Product	Refractive Index at 546.1 nm	B_1	B_2	B_3	C_1 (μm^2)	C_2 (μm^2)	C_3 (μm^2)
N-LAK8	1.71616	1.33183	0.546623	1.19084	0.006200	0.021646	82.5827
N-SF15	1.70438	1.57055	0.218987	1.50824	0.011650	0.059781	132.7093
KZFS12	1.70055	1.55624	0.239769	0.84788	0.010201	0.046927	69.8370
N-LAK14	1.69987	1.50781	0.318866	1.14287	0.007460	0.024202	80.9565
P-SF8	1.69414	1.55370	0.206332	1.39708	0.011658	0.058208	130.7481
N-SF8	1.69413	1.55075	0.209816	1.46205	0.011433	0.058272	133.2415
N-LAK9	1.69401	1.46231	0.344399	1.55080	0.007242	0.024335	85.4686
N-LAK12	1.68083	1.17365	0.588992	0.97801	0.005770	0.020040	95.4873
SF5	1.67764	1.46141	0.247713	0.94999	0.011182	0.050859	112.0418
N-SF5	1.67763	1.52481	0.187085	1.42729	0.011254	0.058899	129.1416
N-BAF10	1.67341	1.58510	0.143559	1.08215	0.009266	0.042448	105.6135
N-BASF2	1.66883	1.53652	0.156971	1.30196	0.010843	0.056227	131.3399
N-SSK5	1.66152	1.59222	0.103520	1.05107	0.009202	0.042353	106.9273
Average Value	**1.68792**	**1.49284**	**0.270202**	**1.22232**	**0.009489**	**0.043400**	**107.3919**

The average values of the Sellmeier coefficients listed in Table 4.1, and the Sellmeier equation, were used to calculate the wavelength dependent refractive index of nigrosin. It is not expected that any of the 13 glass samples interact with light in exactly the same manner as nigrosin dye, but approximate wavelength dependent refractive indices are more desirable than the use of a constant n value for Mie theory calculations. The data in Table 4.1 is quite variable for some coefficients, but since in the initial selection criteria it was not known which specific colors or types of glasses would best represent the refractive index of nigrosin particles, all values in Table 4.1 were used.

The resulting complex refractive indices for nigrosin are shown in Figure 4.3. The refractive index is plotted on the left y-axis and the extinction coefficient is on the right. The imaginary portion of the complex refractive index for nigrosin is relatively high (greater than 0.1) in the UV and visible wavelengths. However, at wavelengths greater than 900 nm, scattering is expected to dominate the total extinction of nigrosin dye aerosols.
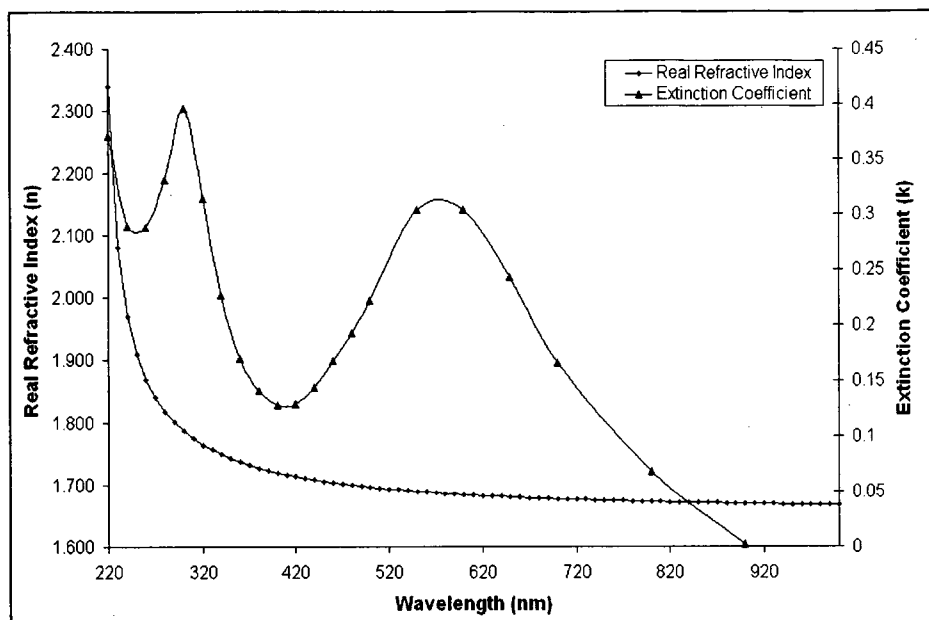
Figure 4.3. The calculated wavelength dependent complex refractive indices for nigrosin (note the different axes). The shape of the curve of the extinction coefficient graph mirrors the absorbance spectra, while the graph of the real refractive index is smooth and increases with decreasing wavelength, with a dramatic increase at wavelengths less than 300 nm.

The complex refractive indices in Figure 4.3 were used with a Mie theory Fortran program, which is separate from the MATLAB program introduced in Chapter 3, to calculate the extinction, absorption, and scattering cross sections (cm^2/particle) for nigrosin dye aerosols. However, since the A-DOAS nigrosin experiments measure the extinction from an entire size distribution of particles, the calculations must be performed at multiple wavelengths for each size particle measured by the SMPS. The calculations were done once and a template Microsoft Excel spreadsheet was created with the Mie theory results to simplify the process of calculating extinction for each experiment, with the only input parameter being the particle concentration at each measured size bin. This allowed the quick comparison between the observed nigrosin extinction spectrum and Mie theory for different experimental trials.

Experimental Setup

Powdered nigrosin dye (Sigma-Aldrich) and HPLC grade water (J.T. Baker) were used to prepare nigrosin solutions with concentrations of approximately 5 mg/mL. These

solutions were thoroughly mixed and visually inspected to ensure all of the nigrosin dye was dissolved and there was no solid material. All nigrosin dye solutions were used the same day they were mixed, and were periodically inspected for agglomerates or other changes during each experiment.

A collision type atomizer was used to generate nigrosin dye particles with nitrogen carrier gas at a flow rate of 2 L/min, which is controlled with a mass flow controller (MFC – Sierra Instruments, FastTrak 800). The experimental setup used to measure the extinction of the nigrosin aerosol is different than the setup discussed in Chapter 3 for PSL measurements. The setup shown in Figure 4.4 does not size select the nigrosin prior to the optical measurements of the sample aerosol, but instead measures the number and size distribution of the sample exiting the gas cell.
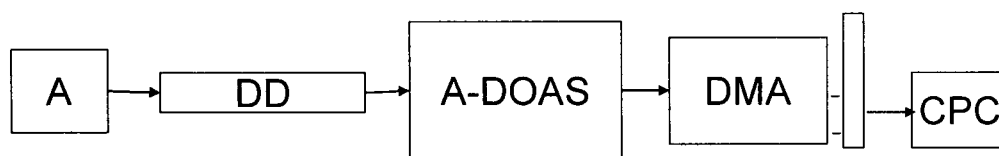
Figure 4.4. The nigrosin solution is atomized in a collision type atomizer and dried in diffusion dryer. The dried aerosol then enters the gas cell of the A-DOAS instrument and the size distribution of the sample is measured by the DMA and CPC upon exiting the gas cell. See Figure 3.11 for the definitions of the abbreviations.

Excess sample flow is vented prior to entering the A-DOAS gas cell. The flow rate through the entire setup (0.35 SLPM) is adjusted to be slightly higher than the rate at which the pump in the CPC pulls (0.30 SLPM). A 1/4" stainless steel ultra-torr tee equipped with a metering valve prior to the entrance to the A-DOAS allows the excess atomizer flow to go through a waste line, which is vented into the laboratory hood. A second ultra-torr tee on the CPC inlet prevents over pressurization by allowing excess flow through an equilibration filter. The sample flow rate through the DMA is recorded at the beginning of each experiment and monitored throughout the course of each trial while the sheath flow rate of the DMA is held constant at 3.0 SLPM.

For each experimental trial, a background zero is measured prior to introduction of the sample. The zero is acquired using the same settings mentioned above, but with the atomizer pump off. Without the nigrosin solution flowing through the atomizer only particle free carrier gas will reach the gas cell. The particle concentration exiting the gas cell is continuously monitored until the concentration reaches a value of less than 1 particle/cm^3. When this concentration is attained, A-DOAS extinction measurements are made until 3 consecutive measurements show very little deviation from the baseline. The final zero measurement set as the background spectrum for the sample measurements. The atomizer pump is then switched on and once the system reaches equilibrium the extinction of the nigrosin aerosol distribution is quantified.

Nigrosin Aerosol Extinction

The extinction of laboratory generated nigrosin aerosols was measured with the A-DOAS instrument and compared to Mie theory calculations. Figure 4.5 shows the result of a Mie theory calculation for the nigrosin particle size distribution data shown in Figure 4.1. The solid diamonds represent the calculated extinction, while the open squares and triangles show the calculated scattering and absorption respectively. The graphs of total scattering and total absorption show distinct features over the wavelength range used for the calculation. The peaks in the calculated absorption data correspond to the peaks in the absorbance measurement made of bulk nigrosin solution, while the peaks in the calculated scattering data are the opposite of the absorption peaks. There are no peaks in the calculated real portion of the refractive index of nigrosin, as can be seen in Figure 4.3. However, when light absorption increases, as it does at the peaks of the calculated absorption in Figure 4.5, there is less light available to be scattered, reducing the intensity of scattered light at those wavelengths. Therefore the total calculated extinction, which is the sum of the calculated scattering and absorption, is relatively featureless.
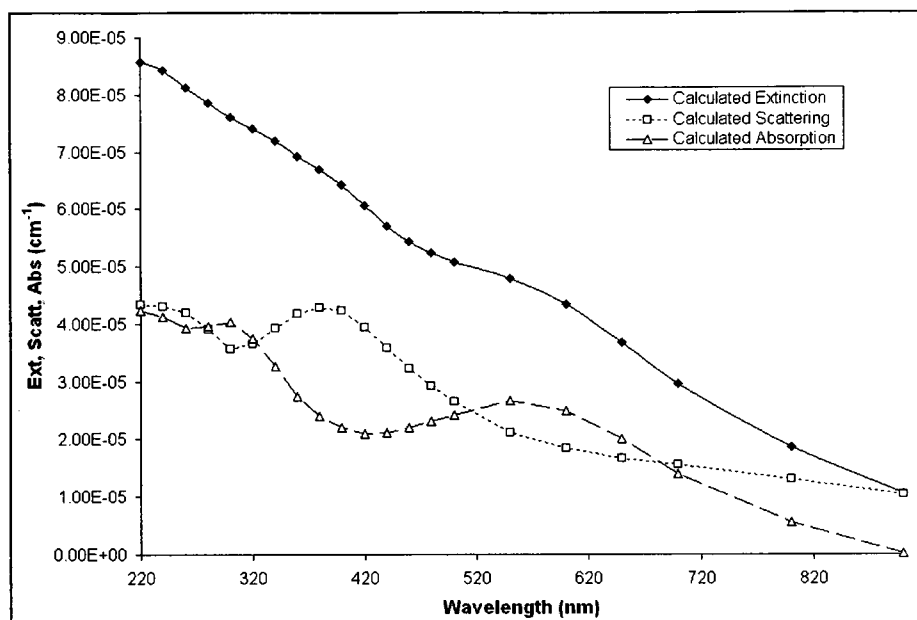
Figure 4.5. The nigrosin size distribution data from Figure 4.1 was used to perform the Mie theory calculations. Scattering and absorption show distinct features with anti-correlated peaks, while the total extinction is largely featureless.

The calculated nigrosin extinction decreases with increasing wavelength, and is relatively flat with a small broad peak at approximately 580 nm. The experimental nigrosin aerosol extinction spectrum (Figure 4.6) contains features that appear to correspond to the absorption peaks in the bulk solution absorbance measurement from Figure 4.2. Also shown in Figure 4.6 are two Mie theory extinction calculations for the measured data. The open squares (solid line) show a Mie calculation using the method described above, while the open triangles (dashed line) show a Mie calculation using the refractive indices calculated using the Sellmeier equation while holding the extinction coefficient constant at 0.31i. This second calculation was performed because the first Mie theory calculation had significant deviations from the measured data at wavelengths greater than 600 nm. The calculation using the larger extinction coefficient at longer wavelengths possibly indicates that nigrosin dye aerosols may absorb (or scatter) more light at these wavelengths than predicted by bulk absorbance measurements or with approximated calculations for the refractive index.
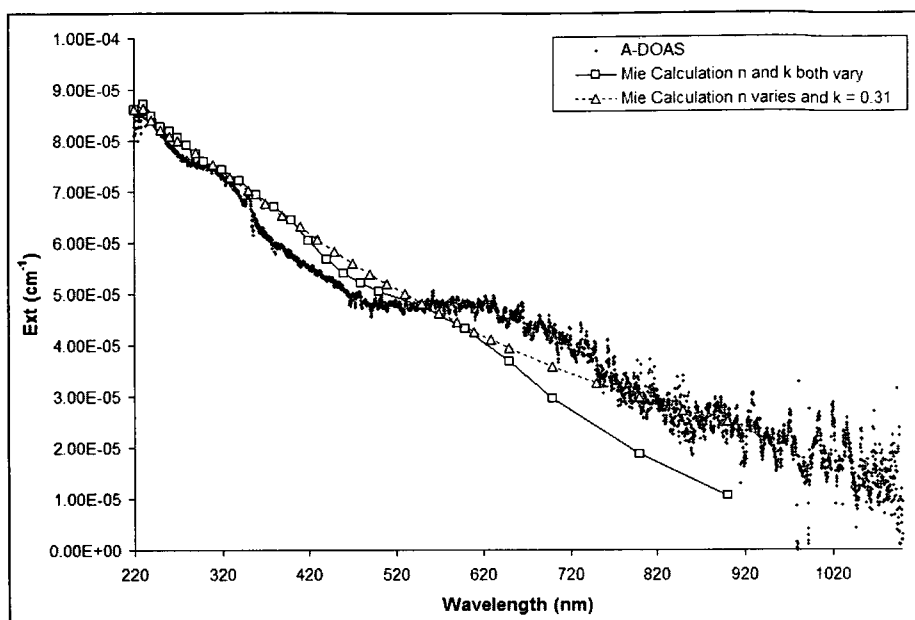
Figure 4.6. The measured nigrosin extinction shows two peaks, one centered at 325 nm and another broader peak at 630 nm. The first peak is absent from both sets of calculated extinction data. There are no peaks in the data calculated with a constant k value, but there is a small peak centered around 575 nm in the calculated data using varying k values. This peak does not match the wavelength of the experimental peak.

The Mie calculations for nigrosin dye aerosols using approximated complex refractive indices, where n and k both vary, do not accurately represent the small scale features observed in the measured data. However, it appears that the overall magnitude and general trend of decreasing nigrosin extinction with increasing wavelength is well represented, with the possible exception of extinction data at wavelengths greater than approximately 600-700 nm. Future work could focus on calculating the complex refractive indices for nigrosin by fitting Mie theory to the experimental results. This will be discussed in greater detail later in this chapter.

A detailed comparison of the A-DOAS spectrum of nigrosin aerosol to the bulk nigrosin absorbance data shows that the two major peaks do not occur at the same wavelengths. The first peak in the bulk solution absorbance data is located at 300 nm, while it is shifted to approximately 325 nm in the nigrosin aerosol data. The second broad peak in the solution phase data centered at 575 nm, while the particle phase data shows it centered at 630 nm. Both of the peaks are red-shifted by approximately 9%.

The red-shifted peaks, if due to absorption, indicate that the nigrosin aerosol is absorbing light at slightly lower energies than it does in an aqueous solution. This could result from the lack of hydrogen bonding in the aerosol phase due to missing water solvation since the particles are dried by molecular sieves in the diffusion dryer. Peaks that result from n → π* transitions shift to shorter wavelengths (blue-shift) as the polarity of the solvent increases. Therefore, the removal of the polar solvent will cause the transition to red-shift (Pavia, Lampman, Kriz 2001).

Relative Humidity Dependence of Nigrosin Aerosol Extinction

The extinction of nigrosin aerosols was measured at different relative humidities (RH) in order to understand how water vapor content affects the extinction of nigrosin aerosol and possibly to better connect bulk measurements to aerosol measurements. To create "dry" particles (RH < 3%) the experimental setup in Figure 4.4 was used, but an RH probe (Varsala – HMP50) was placed on the A-DOAS gas cell inlet to monitor the RH of the sample particles. "Wet" particles (RH ~ 90%) were created by humidifying the sample using a PID controller to control the temperature of a custom water vapor diffusion source located before the A-DOAS gas cell.

As expected, the size distribution of nigrosin aerosols shifts to larger particles at a higher RH due to water uptake. The water vapor present in the humidified air surrounding the nigrosin aerosol samples condenses onto the particles increasing the diameter; essentially growing the small particles into larger particles, as shown in Figure 4.7. Nigrosin samples at high RH contain less small particles (14-35 nm) and more large particles (40-500 nm) than a dry sample created from the same solution, confirming the condensation of water vapor onto the nigrosin aerosols and the resulting particle growth. However, the output of the atomizer is not completely stable over time and the total concentration of particles varies. The result of this phenomenon is that the difference peaks in Figure 4.7 are not equal in magnitude or number between trials. Extinction

measurements of wet and dry nigrosin aerosols cannot be directly compared without taking into account the variation of particle number between samples.
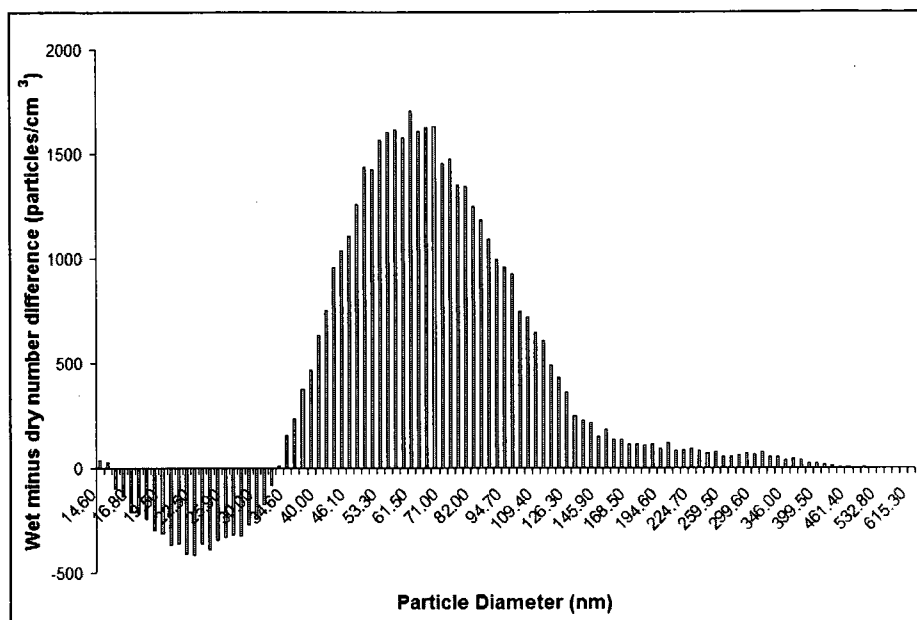
Figure 4.7. The particle size distribution of a dry nigrosin sample was subtracted from a wet nigrosin aerosol sample, created from the same solution, revealing that the wet sample has fewer small particles and a greater number of large particles than the dry sample. The difference in particle size and concentration is largely due to the condensation of water vapor onto the surface of nigrosin aerosol in the humidified sample.

Since the extinction of wet and dry nigrosin aerosol (cm⁻¹) cannot be directly compared, a method to normalize the measured extinction data was utilized. The total aerosol cross sectional area of each sample was calculated by multiplying the cross sectional area of each particle size by the particle number concentration in that size bin. The measured extinction (cm⁻¹) was divided by the summed total aerosol area of all bins for each nigrosin sample (cm² aerosol/cm³ sample volume), yielding the dimensionless quantity used in Figures 4.8 and 4.9 (Q_{ext} – extinction efficiency of the total size distribution). This transformed value allows for the comparison between wet and dry nigrosin samples because it corrects for the variation in the atomizer output.

Figure 4.8 illustrates the difference between the extinction efficiencies for wet and dry nigrosin aerosol samples. The wet nigrosin sample attenuates on average 45% more light per total aerosol area than the dry nigrosin. This value is consistent over the

entire wavelength range. It is unlikely that the increase in extinction is due to dilution of the nigrosin by water because this process should reduce extinction by lowering both portions of the refractive index of the nigrosin particles. The nigrosin particles increase in size at higher RH, but the method of normalizing the data accounts for any increased extinction that is solely due to increased aerosol size. A likely scenario is that water vapor condenses onto the surface of the nigrosin particles creating a coating on the outside of the aerosol (Shiraiwa, Kondo et al. 2010). It has been reported in the literature that coating soot particles with a non-absorbing layer increases measured extinction because the coating layer acts as a lens, focusing the light onto the absorbing material at the center of the particle (Fuller, Malm et al. 1999; Saathoff, Naumann et al. 2003; Schnaiter, Linke et al. 2005; Bond, Habib et al. 2006; Khalizov, Xue et al. 2009; Lack, Cappa et al. 2009; Lack and Cappa 2010). This is possible because nigrosin dye is only slightly water soluble (~5 g/L). Therefore, a dried nigrosin particle would need 200 times its mass in water to completely dissolve. For example, a nigrosin particle with a diameter of 80 nm (3.94×10^{-16} grams) would need 7.88×10^{-14} grams of water, which would be equivalent to a 265 nm water aerosol, to completely dissolve it. Therefore, it is likely that the water taken up by the nigrosin particles adsorbs to the surface of the dye and does not form an internally mixed aerosol.
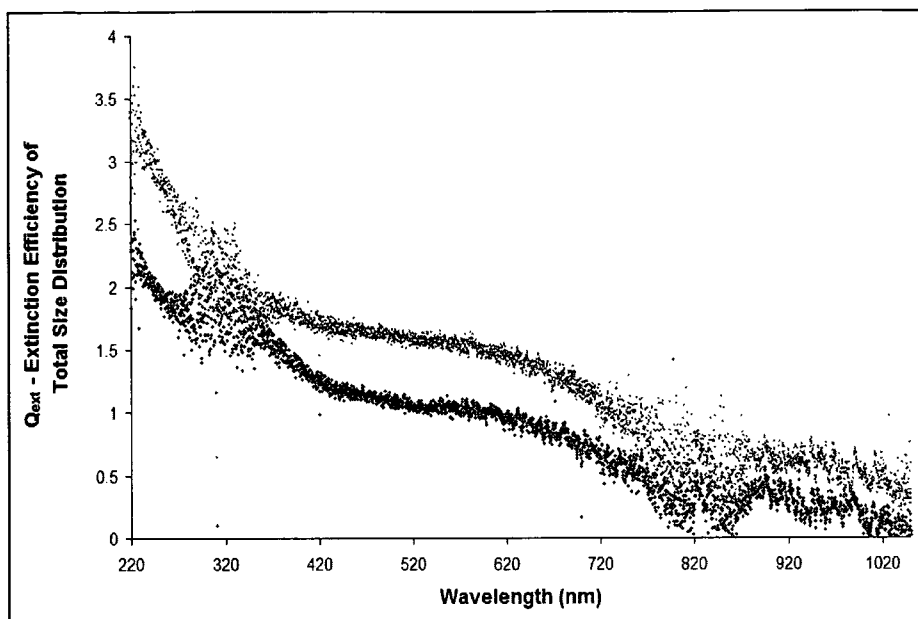
Figure 4.8. The lighter points correspond to wet nigrosin while the darker points correspond to dry nigrosin. Increasing the humidity of the nigrosin aerosol samples enhances the measured extinction efficiency of the entire size distribution by approximately 45%. It is possible that water coating the outside of the particles acts like a lens and focuses light onto the absorbing center of the particle, increasing the attenuation of light.

The reliability of this method of data comparison was determined by comparing the extinction efficiency of the total size distribution of multiple dry samples. Figure 4.9 shows an overlay of five individual spectra from multiple trials of dry nigrosin aerosol. The data for the five samples should theoretically be the same since extinction efficiency area should be an intrinsic value to nigrosin aerosol under constant conditions. The graphed data overlay each other and vary by only a few percent. This was taken as confirmation that the method of normalizing the data using extinction efficiency of the total aerosol size distribution is useful for comparisons between nigrosin samples generated in a consistent manner, even though the concentration in each size bin may vary. This shows that the observed difference between dry and humidified nigrosin aerosols is real and not a product of a change in concentration or size distribution.
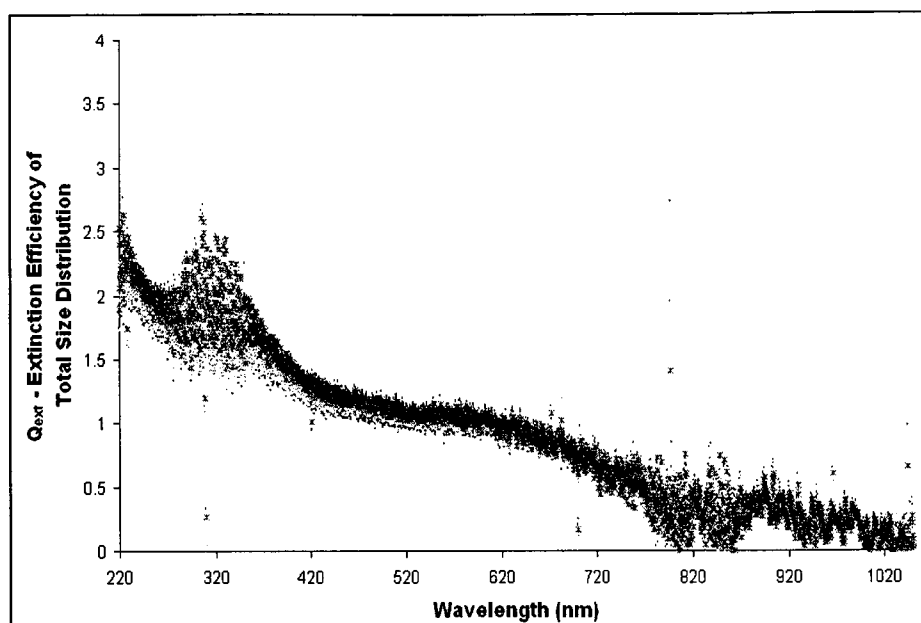
Figure 4.9. The small variation between multiple samples of dry nigrosin aerosol shows that the method of normalizing the extinction data with total aerosol area can be used to compare wet and dry nigrosin samples because the difference in the data will be due to an optical difference between the particle samples.

Further evidence that the extinction difference between wet and dry nigrosin aerosols is real is shown in Figure 4.10 (A) and (B). Mie calculations were performed for both samples, using their respective concentrations and size distributions. In Figure 4.10 (A), Mie theory calculations (open squares) do a good job representing the magnitude and trend of the measured extinction for the dry nigrosin aerosol. However, in Figure 4.10 (B), Mie theory underestimates the extinction of the wet nigrosin sample. This indicates that the optical constants used for the calculation are not representative of the aerosol sample that was measured. The addition of water vapor to the nigrosin aerosol sample clearly alters the physical properties of the particles, changing the way the nigrosin interacts with light. An increase in the extinction predicted by Mie theory for (B) would be expected if a lensing amplification factor were considered in the Mie theory calculation.

(A) DRY

(B) HUMIDIFIED
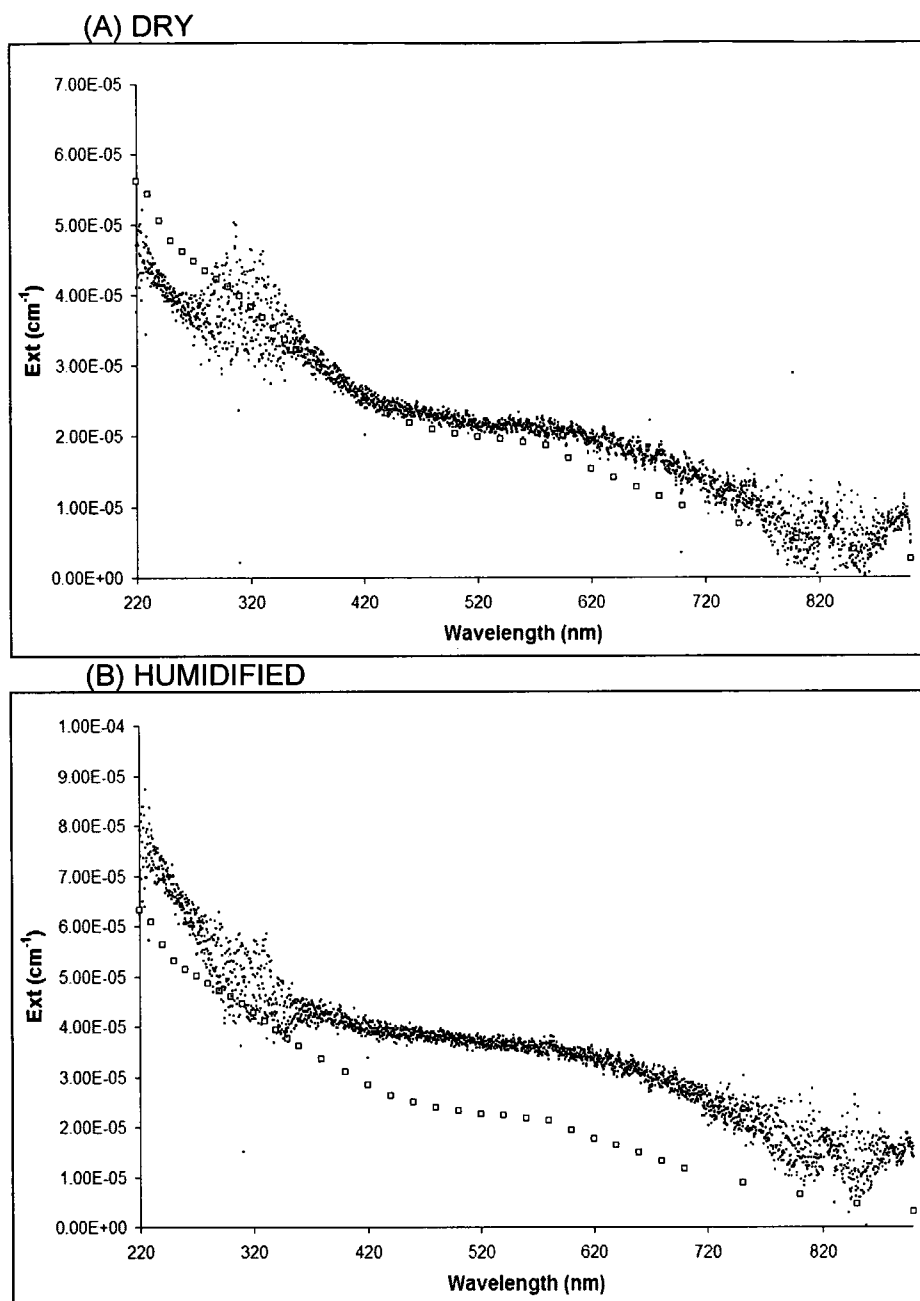
Figure 4.10. A Mie theory calculation for dry nigrosin aerosol is shown in (A). The calculated extinction is close to the measured extinction in both magnitude and the overall wavelength dependent trend. However, the Mie theory calculations for wet nigrosin aerosol in (B) underestimate the extinction of the sample. The optical properties of nigrosin dye aerosols in a humidified sample are clearly not the same as they are for a dry sample.

Measurement of nigrosin dye extinction at two different relative humidities show that the optical properties of these particles change with water vapor concentration. This experiment also highlights the ability of the A-DOAS to measure humidity dependent

aerosol extinction under controlled laboratory conditions. This technique promises exciting results in the future, as the humidity dependence of aerosol extinction is poorly characterized for many types of aerosols (IPCC 2007).

Size Selected Nigrosin

A new method for creating nigrosin aerosol concentrations high enough to measure the extinction of size selected particles was devised in April 2010. The experimental setup used for the measurement of size selected nigrosin was the same as the configuration explained in Chapter 3. The adjustments to produce very high particle concentrations were: the nitrogen flow into the atomizer was set to 3.0 L/min, the valve on the front of the atomizer was closed to force all of the nitrogen flow into the atomizer block, and the waste and sample lines did not diverge until the particles reached the DMA inlet. This provided the high concentrations of size selected nigrosin particles needed to exceed the detection limit of the A-DOAS.

The experimental extinction of nigrosin dye particles was measured at particle sizes corresponding to 70, 100, 200, 300, 400, 450, 600, and 700 nm. An example of a raw extinction spectrum is shown in Figure 4.11 for 100 nm nigrosin particles with a concentration of 33850 particles/cm^3 ± 10%. The extinction is highest at short wavelengths because 100 nm nigrosin particles will most efficiently attenuate light at wavelengths of approximately 100 nm. A small peak at approximately 320 nm can be seen in the data, which correlate to the peak in the extinction spectrum of the entire size distribution of nigrosin (Figure 4.6).
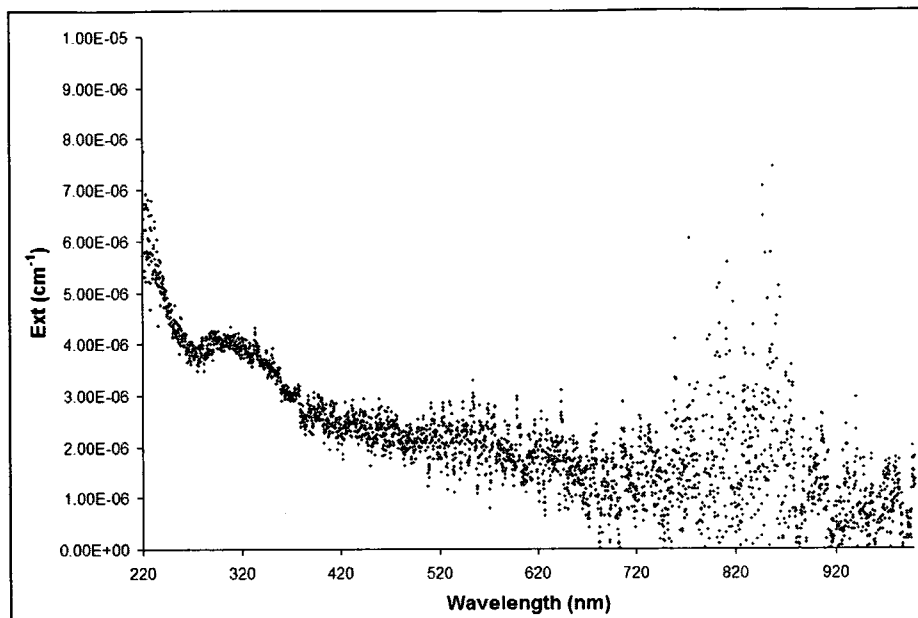
Figure 4.11. 100 nm nigrosin particles attenuate light more efficiently at short wavelengths. The overall extinction trend in this figure was expected based on the size of the particles and the wavelengths of light. However, it also appears that the absorption features seen in the extinction spectrum of a size distribution of nigrosin are preserved in the size selected spectrum as well.

It was possible to create Q_{ext} versus size parameter figures for nigrosin at different wavelengths and compare the results to Mie theory calculations using the complex refractive indices for nigrosin that were discussed earlier in this chapter. Figure 4.12 shows experimentally measured size dependent extinction efficiency of nigrosin (diamonds) and the results of Mie calculations using a complex refractive index of m = 1.692 + 0.2689, which is complex refractive index at 530 nm calculated using the method discussed earlier. This complex refractive index was used because it is very close the literature values known for 532 nm (Garvey and Pinnick 1983; Lack, Lovejoy et al. 2006; Dinar, Riziq et al. 2008; Lang-Yona, Rudich et al. 2009). The experimental data used to calculate Q_{ext} for each size of nigrosin at 530 nm is the average of measured data from 525-535 nm. The experimental Q_{ext} values correlate well with those predicted by Mie theory at this wavelength. This was expected because nigrosin has been studied extensively and the complex refractive index is well characterized at this wavelength.
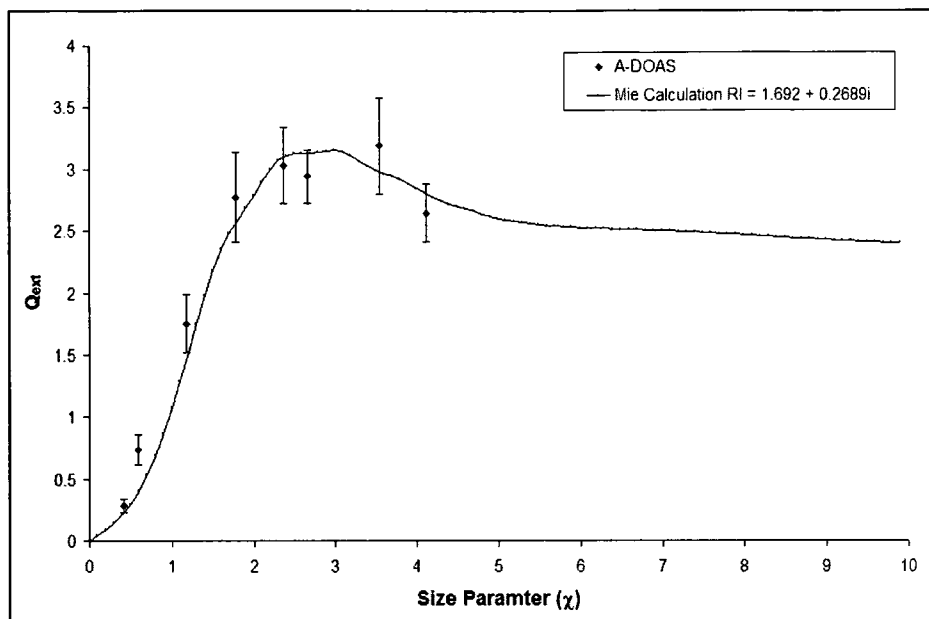
Figure 4.12. The experimental extinction efficiencies (diamonds) correlate well with those predicted by Mie theory at 530 nm (black line). This was expected because the complex refractive index of nigrosin is well known at 532 nm and the calculated complex refractive indices used in this work were adjusted to correspond to average literature values at that wavelength. The line connecting Mie theory calculation data points is to guide the eye for clarity.

The idea expressed at the end of Chapter 3 was that the A-DOAS could be used to find the wavelength dependent complex refractive index of aerosol samples by measuring extinction at various sizes and fitting Mie calculations to the extinction efficiency data. This was briefly attempted at various wavelengths with the size selected nigrosin data and it is recommended that it be refined in the future. Figure 4.13 shows the experimental extinction efficiency versus size parameter for nigrosin at a wavelength of 220 nm (diamonds). The error bars (1σ) for measurements at the highest size parameters are large because the nigrosin particle concentrations for these experiments were low, and the extinction was close to the detection limit of the A-DOAS. The solid black line represents a Mie calculation using the complex refractive index for nigrosin at 220 nm that was calculated using the methods discussed earlier in this chapter, m = 2.339 + 0.3139i. This complex refractive index does not appear to accurately represent the observed nigrosin extinction efficiency at 220 nm. The gray triangles correspond to Mie theory calculations performed by "guessing" at a complex refractive index then

adjusting it to better fit the experimental data. Figure 4.13 shows that a complex

refractive index of 1.9 + 0.15i fits the experimental data better than the complex

refractive index at 220 nm that was determined and used earlier in this Chapter.
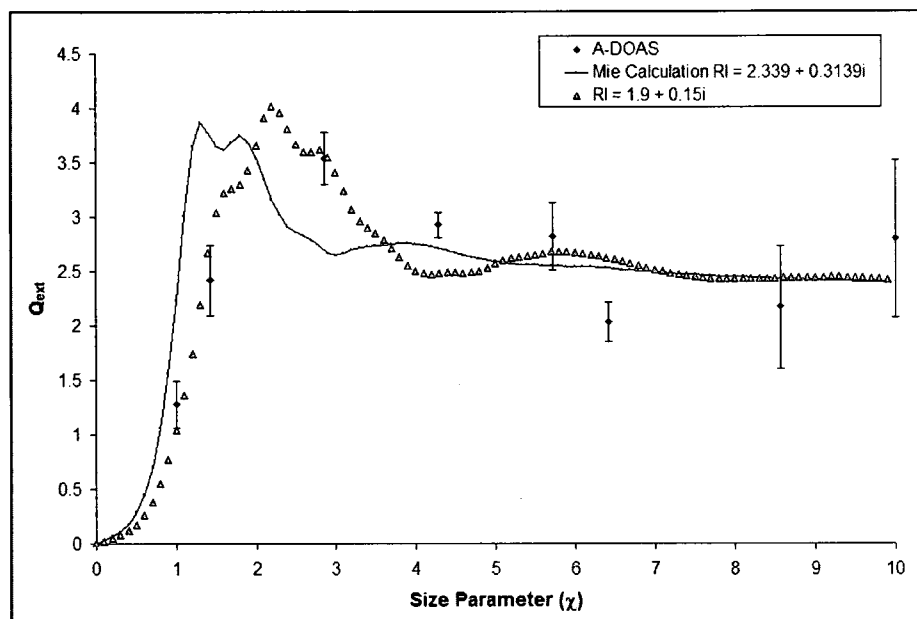
Figure 4.13. A complex refractive index of 1.9 + 0.15i provides a better fit to the experimental Q_{ext} data than a complex refractive index of 2.339 + 0.3139i at a wavelength of 220 nm. This indicates that the complex refractive indices that were calculated using bulk absorption measurements and the Sellmeier coefficients of different glasses do not accurately represent nigrosin aerosols.

The procedure used to produce Figures 4.12 and 4.13 was repeated for light with

wavelengths of 425 and 700 nm, which are shown in Figure 4.14 and 4.15 respectively.

The complex refractive index used in previous Mie calculations at 425 nm appears to

correlate well with the experimental data (Figure 4.14 – black line). However, there is

what appears to be an errant data point for the size parameter corresponding to 600 nm

nigrosin particles, which could not be reconciled by using different complex refractive

indices. The extinction measured for 600 and 700 nm nigrosin particles was close to the

detection limit, which may have lead to incorrect calculations of the extinction efficiency

for these particles. However, this cannot be verified until additional experiments are

conducted in the future. A slight change in the complex refractive index from m = 1.712

+ 0.1150i to m = 1.70 + 0.16i (gray triangles) seems to provide a slightly better fit to the

experimental data especially in the size parameter range from 2-3.5.
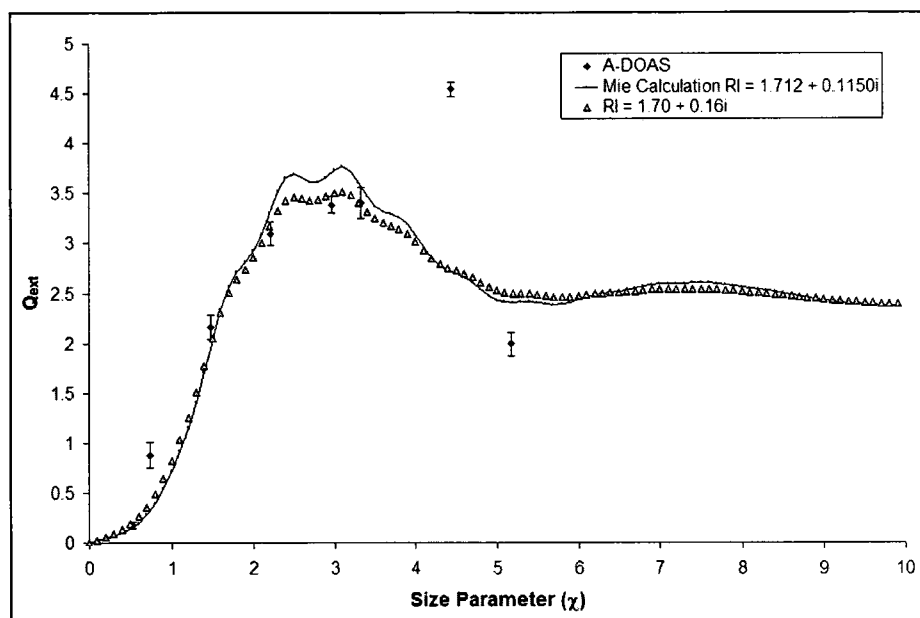
Figure 4.14. A complex refractive index of 1.712 + 0.1150i correlates fairly well with the
measured extinction efficiency of nigrosin at a wavelength of 425 nm except for the data points
corresponding to the extinction of 600 and 700 nm nigrosin particles, which were close to the
detection limit of the A-DOAS. Increasing the extinction coefficient from 0.1150i to 0.16i at 425
nm provides a better fit to the experimental data.

Figure 4.15 displays the extinction efficiency of nigrosin at a wavelength of 700

nm. The Mie calculation using a complex refractive index of m = 1.677 + 0.1667i (black

line) does not correlate well with the measured extinction efficiency, especially at size

parameters less than χ = 2. It was found that a complex refractive index of m = 1.9 +

0.20i (gray triangles) provides a better fit to the experimental Q_{ext} values.
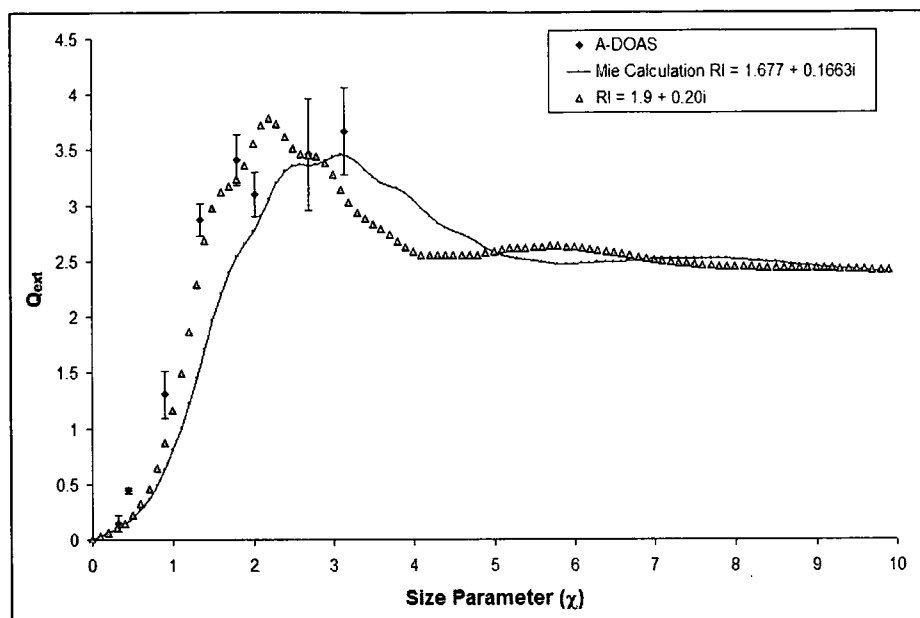
Figure 4.15. The experimental extinction efficiency at size parameters greater than 2 correlate well with Mie calculations performed using a complex refractive index of m = 1.667 + 0.1663i (black line) at a wavelength of 700 nm. However, adjusting the complex refractive index to m = 1.9 + 0.20i yielded a better fit to the experimental data (gray triangles), especially at size parameters less than 2.

The experiments with size selected nigrosin particles provided valuable information on two fronts. First, Figure 4.13 to 4.15 show that the method used for estimating the wavelength dependent complex refractive index of nigrosin is not accurate at all wavelengths. This difference is likely the reason that the absorption features seen in the extinction spectrum of the entire size distribution of nigrosin particles are not predicted well by Mie theory using approximate complex refractive indices. Second, and more importantly, these experiments suggest that it is possible to use the A-DOAS to measure size selected aerosols, calculate Q_{ext}, and determine the wavelength dependent complex refractive index using Mie theory. The complex refractive indices used to fit the data in the above figures were determined by guessing a complex refractive index and adjusting it to provide a visual best fit to the experimental data. Presently, this process is time consuming and inaccurate. Future work should focus on creating a computer program that can quickly find the complex refractive index that best fits the experimental data through iterative methods. The ability to determine

the complex refractive index for aerosol samples of different compositions, at many wavelengths throughout the solar spectrum, can provide invaluable data that can be used to more accurately model the radiative forcing of aerosols by inclusion in GCMs.

Preliminary Carbon Black Results

Carbon black (CB), a product of incomplete combustion, is made almost entirely out of insoluble amorphous elemental carbon. CB, like soot, is highly absorbing and does not contain specific absorption features (like nigrosin). This makes CB an ideal substance to use in order to quantify the ability of the A-DOAS to measure a highly absorbing aspherical aerosol that has a high extinction coefficient throughout the wavelength range of interest (Cataldo 2002; Quinten, Kreibig et al. 2002; Bertocchi, Kribus et al. 2004; Bond and Bergstrom 2006). A carbon black sample was obtained and small amount (0.075 g) was suspended in 20 mL of HPLC grade water. The CB sample coagulated within the peristaltic tubing of the atomizer and therefore could not be atomized in the same manner as previous samples in this work. Dry dispersing the CB was necessary to produce carbon black aerosol samples.

Nitrogen carrier gas (2 SLPM) was used to disperse a sample of CB placed at the bottom of a glass impinger (Figure 4.16). The velocity of the nitrogen carrier gas was increased by stepping down the diameter of the tubing in the impinger from 1/2" to 1/8". As the nitrogen exited the tubing it created a cloud of CB. The CB aerosols that did not quickly re-settle exited through an outlet located at the top of the setup. The experimental sample flow through the system was held constant at 0.40 SLPM. The sample flow was constantly monitored with a flow meter and a metering valve was used to adjust the flow to ensure it remained constant. The flow was vented into a hood.
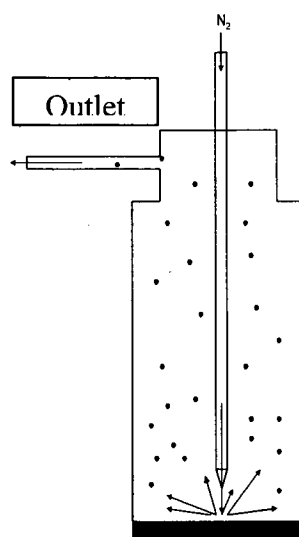
Figure 4.16. Nitrogen carrier gas was used to disperse a carbon black sample within a glass impinger. The aerosol sample exited at the top of the impinger.

This method of dry dispersing the CB produced concentrations that were high enough to measure the extinction of size selected CB. The extinction of CB aerosol with mobility diameters of 80, 100, 200, 300, 400, 500, 600, and 650 nm, was measured. Unlike nigrosin aerosols, which are spherical, CB is irregularly shaped and the mobility diameter of CB will not be the same as the actual diameter (Bertocchi, Kribus et al. 2004). Therefore, Mie theory calculations using these diameters for CB must be viewed as approximations because the Mie theory programs used in this work assume spherical particles.

The process used to dry disperse the CB induced changes in the sample flow rate, which caused the appearance of a large pressure peak in the extinction data from 270-340 nm, as shown in Figure 4.17. This figure displays the experimentally determined extinction of 600 nm CB with a concentration of 921 particles/cm^3 ± 10%. The method described here is promising for dry dispersing aerosols prior to being monitored by the A-DOAS, but future work should focus on reducing the pressure peaks that result from variations in the sample flow rate. The observed pressure peaks in the CB experiments are sharper than those seen in previous experiments, and this

difference in peak shape could be caused by the addition of the impinger to the experimental setup.
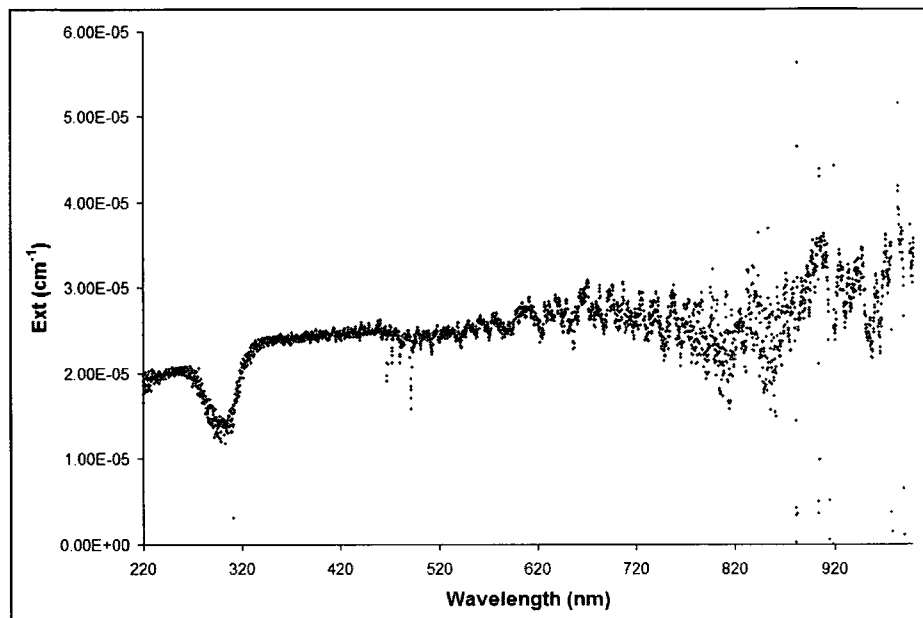
Figure 4.17. The method used to produce high concentration of dry dipersed CB caused changes in the sample flow rate through the gas cell. This change in pressure results in the large inverted peak at approximately 300 nm.

Due to the presence of the pressure peak in the experimental CB data, no data below a wavelength of 500 nm was used for calculations. Figure 4.18 shows the experimental CB extinction efficiency at a wavelength of 500 nm versus size parameter, both of which were calculated using the mobility diameter (open circles). Mie calculations were performed to visually fit a complex refractive index to the experimental extinction efficiency of CB. A complex refractive index of m = 2.3 + 0.50i was input into the Mie program to yield the black line in Figure 4.18 and appears to fit the data (error bars = 1σ, N ≥ 5 measurements).
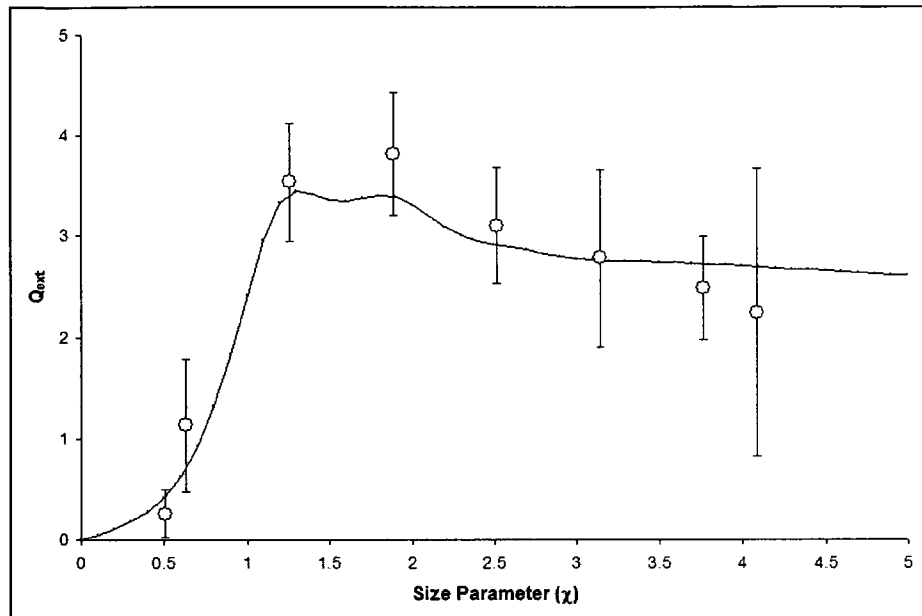
Figure 4.18. The experimental extinction efficiency of CB (open circles) matches the trend produced by a Mie calculation using a complex refractive index of m = 2.3 + 0.50i at a wavelength of 500 nm.

The complex refractive index for carbon black has been approximated as m = 2.0 + 1.0i (Janzen 1979; Taha, Box et al. 2007), and the complex refractive index for a polydisperse cloud of carbon black was calculated with a solar particle receiver to be m = 1.58 + 0.57i at 532 nm by Bertocchi et al. 2004. Bond and Bergstrom et al. 2006 recommend a complex refractive index of 1.95 + 0.79i at 550 nm for highly absorbing carbonaceous aerosols. The complex refractive index for carbon black and similar light absorbing carbonaceous materials can cover a range of values that vary with measurement technique and the source of the sample. Therefore, it is possible that the complex refractive index for CB determined using the A-DOAS data in Figure 4.18 is accurate since it falls within the range of other literature values. However, these results could be improved, and a more accurate value of the complex refractive index obtained, by repeating the experiment with an updated setup that reduces the pressure peak, and a more advanced fitting routine. These improvements should be goals of future work with the A-DOAS.

97

CHAPTER 5

PRELIMINARY EXTINCTION RESULTS FROM AMBIENT AIR MEASUREMENTS AND
SUGGESTIONS FOR FUTURE WORK

Experimental Setup

One of the primary goals in the acquisition of the A-DOAS instrument was to

experimentally determine the broadband extinction of ambient aerosols. Initial work

towards this goal was accomplished with preliminary measurements using the

experimental setup shown in Figure 5.1. The CPC pump was used to pull ambient air

through the equipment at a flow rate of 1.5 L/min. The DMA sheath flow rate was held

constant at the recommended value of 10 times the sample flow rate (15.0 L/min).

There was a small impinger (approximately 0.5 -1 L) placed before the filter. This was

used as a "settling" volume for any large particles that may be present in the ambient

aerosol sample. After the impinger, the air stream encounters a valve which controls the

direction of the sample flow. At one of the valve positions (filter-off), the ambient air

sample flows unobstructed into the A-DOAS gas cell. At the other valve position (filter-

on) the ambient air must flow through a filter (Pall HEPA Capsule – #12144) and the

ambient aerosols are removed. The background (zero) measurement is recorded with

the valve turned to the filter-on position and a particle concentration of less than 1

particle/cm^3 is detected by the CPC. After the zero is recorded, the valve position is

adjusted to filter-off and the ambient aerosols are monitored. The difference between

the zero and the experimental measurements is attributed to aerosol extinction.
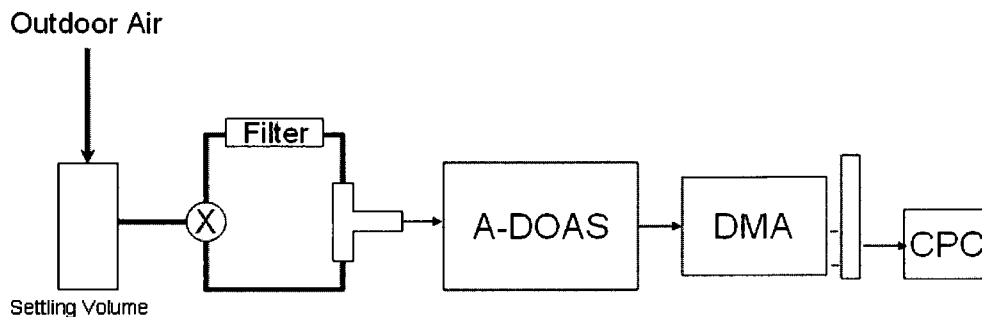
Figure 5.1. The experimental setup used for the determination of ambient aerosol extinction uses a valve (circle with cross) to easily switch between the filtered zero measurement and ambient aerosol samples. The CPC pump pulls through the setup at 1.5 L/min while A-DOAS measurements are made.

There are three assumptions that were made when measuring the experimental extinction of ambient aerosols. First, there is no size cutoff for the sampled ambient aerosols, as an impactor was not used. Therefore, it is possible for large aerosols to enter the A-DOAS gas cell and contribute to the experimentally determined extinction. These large particles will not be counted by the SMPS, which only measures particles with diameters less than 661 nm for these experiments. The flow settings needed to achieve these size distribution measurements are discussed below. For this preliminary work it was assumed that the contribution of these large particles to the measured extinction is negligible, even though that may not always be true, especially on high pollen count days, windy days with blowing dust, and days when wind generated sea spray is coming directly off the ocean. Second, it was assumed that all gas phase species are able to pass through the filter, and that the concentrations of absorbing gas phase species are the same for the experimental measurements and the corresponding zero. Third, when performing Mie calculations it was assumed that the ambient aerosols are spherical and have a constant complex refractive index ($m = 1.5 + 0.001i$) over the wavelength range of the A-DOAS. This final assumption clearly does not agree with previous statements and data from previous chapters of this work, but without any

specific chemical information, there is no easy way to estimate the wavelength dependence of the complex refractive index of the ambient aerosols.

To ensure the SMPS can measure the widest range of particle sizes possible, the CPC flow rate was reduced to 0.30 L/min after approximately 5 or 6 A-DOAS measurements (for this work - 120 second integration/acquisition time). With a CPC flow rate of 1.5 L/min and a DMA sheath flow rate of 15.0 L/min, the largest particle size the SMPS can measure is 228 nm. A large number of accumulation mode aerosols could be uncounted in each experiment. Therefore, the design of an experimental trial typically consisted of the following pattern: 1) an A-DOAS zero is recorded when the particle concentration is less than 1 particle/cm^3 with the CPC flow at 1.5 L/min and the sheath flow at 15.0 L/min, 2) the valve is then adjusted to the filter-off position to allow ambient aerosols to enter the A-DOAS and approximately 5-6 measurements are recorded 3) the CPC and DMA sheath flow rates are decreased to 0.30 L/min and 3.0 L/min respectively (and the A-DOAS recording stopped). The third step in a typical trial allows the SMPS to measure the ambient aerosol sample concentrations at sizes of up to 661 nm. The aerosol size distributions measured by the CPC at the low flow rates are expected to correspond to the A-DOAS data that was recorded a few minutes earlier with the high flow rates. This method provides a faster sampling time than if the CPC was running at 0.30 L/min for the entire experiment, and more complete size distribution measurements than are possible if the higher flow rates were maintained over the course of the experiment.

Preliminary Results

Daytime ambient aerosol extinction measurements were performed from May 14, 2010 to June 07, 2010 from the first floor window of laboratory G134 in Parsons Hall on the University of New Hampshire's Durham campus. During the sampling period the total particle concentrations ranged from less than 1000 particles/cm^3 to greater than

10500 particles/cm^3, with the majority of particles having diameters of less than 150 nm. The small particle diameters and relatively low aerosol concentrations lead to measured extinction values close to the detection limit of the A-DOAS, especially at wavelengths greater than approximately 400 to 500 nm. For visual clarity, twenty individually measured A-DOAS wavelengths were averaged for each extinction data point displayed in the figures included in this chapter (20 pts ~ 5 nm). Figure 5.2(A) shows an example of the measured ambient aerosol extinction on May 20, 2010 (4 pm LST). The extinction is below the detection limit at wavelengths greater than approximately 450 nm, but increases rapidly at wavelengths less than 400 nm. This type of spectrum is expected for a sample of small non-absorbing aerosols. The Mie calculation (open squares) was performed in the same manner as was for the nigrosin calculations in Chapter 4 that used the entire measured size distribution, but with a constant complex refractive index of m = 1.5 + 0.001i. This complex refractive index appears to represent the trend of the measured data fairly well, but underestimates the extinction at shorter wavelengths. However, this was expected because the complex refractive index used does not vary with wavelength. The refractive index of the ambient aerosols likely increases with decreasing wavelength, which would lead to greater extinction at short wavelengths than what is predicted by the Mie theory calculation. Figure 5.2(B) displays the 48 hour back trajectory of the air mass measured in Figure 5.2(A), and was determined using archived meteorological data and the NOAA HYSPLIT Model (data and model found at - http://ready.arl.noaa.gov/HYSPLIT_traj.php). This shows that the measured aerosol sample traveled through clean environments (e.g. marine and clean continental) before reaching Durham, NH. Therefore, the expected aerosol extinction would be low, as the aerosol sample is likely highly scattering and consists of mostly small particles.

(A)

(B)

NOAA HYSPLIT MODEL
Backward trajectory ending at 1700 UTC 20 May 10
GDAS Meteorological Data
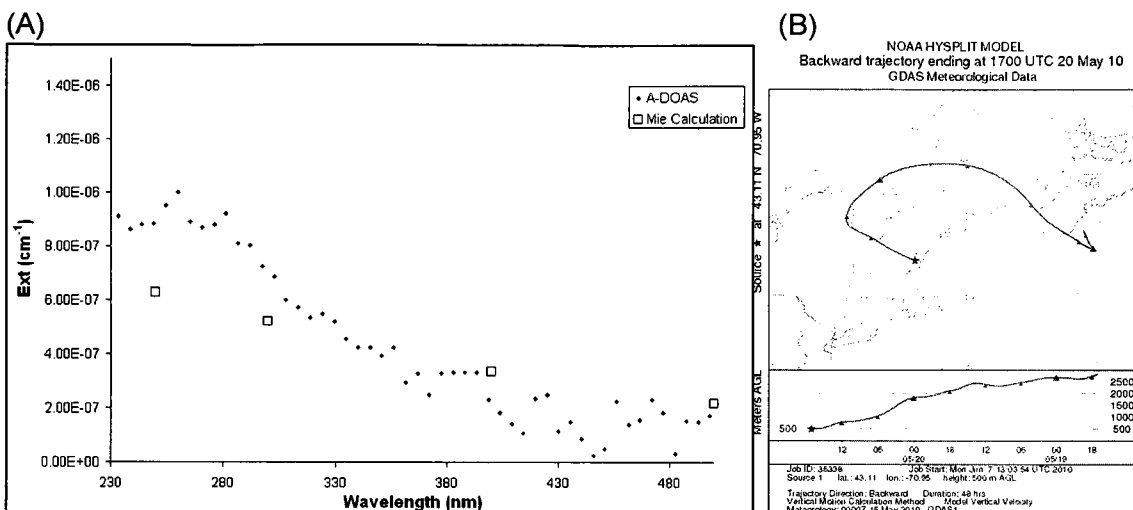
Figure 5.2. (A) The experimentally determined aerosol extinction of an ambient sample (total concentration = 2500 particles/cm^3) on May 20, 2010. Measurements at wavelengths greater than 500 nm are below the detection limit (not shown). The Mie calculation performed using a complex refractive index of m= 1.5 + 0.001i does a good job reproducing the observed overall trend. The extinction rapidly increases at UV wavelengths because small particles (mean sample diameter = 75 nm) more efficiently scatter shorter wavelengths of light. (B) The back trajectory for the aerosol sample shows that the particles were minimally influenced by polluted environments and are likely highly scattering.

Quebec, Canada experienced forest fires at the end of May and beginning of June, 2010 (http://www.wmur.com/news/23738760/detail.html). Figure 5.3(A) shows the back trajectory for 00:00 UTC on June 01, 2010. The air mass depicted originated in Canada and likely transported smoke from the forest fires to Durham, NH. Later that day the wind direction changed and the back trajectory in Figure 5.3(B) for 18:00 UTC (Local time = UTC – 4 hours in the summer) shows the air mass reaching Durham, NH traveled over the polluted East Coast of the U.S. The change in back trajectories occurred between 4:00 and 8:00 UTC.
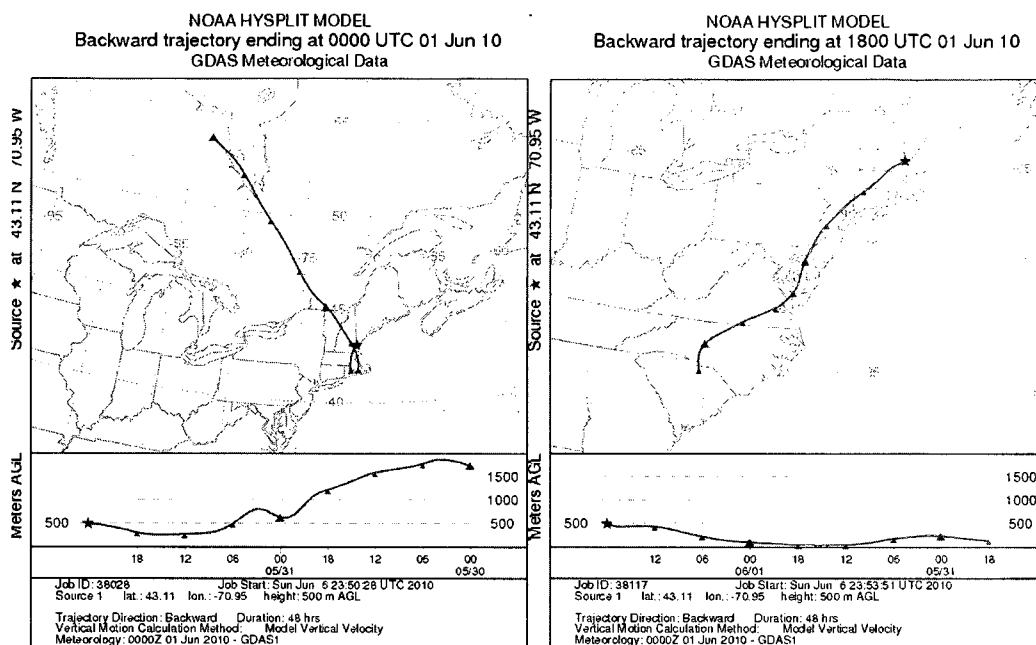
Figure 5.3. (A) The air mass reaching Durham, NH early on June 1, 2010 originated in Canada and may have transported forest fire smoke to New Hampshire. (B) Later that day the back trajectory shows an air mass traveling up the polluted East Coast of the U.S.

The A-DOAS was used to measure ambient aerosol on June 01, 2010. The back trajectories shown in Figure 5.3 indicate that the aerosols sampled on that day could be a mix of smoke from Canadian forest fires and aerosols originating in urban areas on the East Coast. It is impossible to distinguish these aerosols without chemical data, but some interesting observations can be made from the A-DOAS data displayed in Figure 5.4(A). The trend (slope) of the Mie theory calculation performed using the particle size distribution shown in Figure 5.4(B), seems to correlate to the overall trend in the measured extinction. However, unlike Figure 5.2(A), Mie theory calculations underestimate the extinction at all wavelengths by approximately half. The extinction trend represented by the real part of the complex refractive index used in the Mie calculations appears to be accurate ($k = 0.001i$ is negligible), but the difference in magnitude could indicate a highly absorbing aerosol sample. A large extinction coefficient over all wavelengths, as would be expected for an aerosol sample containing smoke, would increase the measured extinction relative to purely scattering aerosols.

There is also an extinction peak at approximately 270 nm. Without any chemical

information this peak cannot be attributed to a specific chemical compound, but PAHs

(e.g. benzene and naphthalene), which absorb in this region (Joblin, Leger et al. 1992),

can be formed during wildfires (Lopes and deAndrade 1996; Kim, Oh et al. 2003;

Galarneau, Makar et al. 2007), and the oxidation of aerosols over time has been shown

to increase absorption at short wavelengths (Horvath 1993; Andreae and Gelencser

2006; Sun, Biedermann et al. 2007; Barnard, Volkamer et al. 2008). The conditions

needed to oxidize aerosols could have been present in the air mass transported up the

polluted East Coast (Atkinson 2000; de Gouw, Middlebrook et al. 2005; Volkamer,

Jimenez et al. 2006), or an identified local source could have contributed to this process.
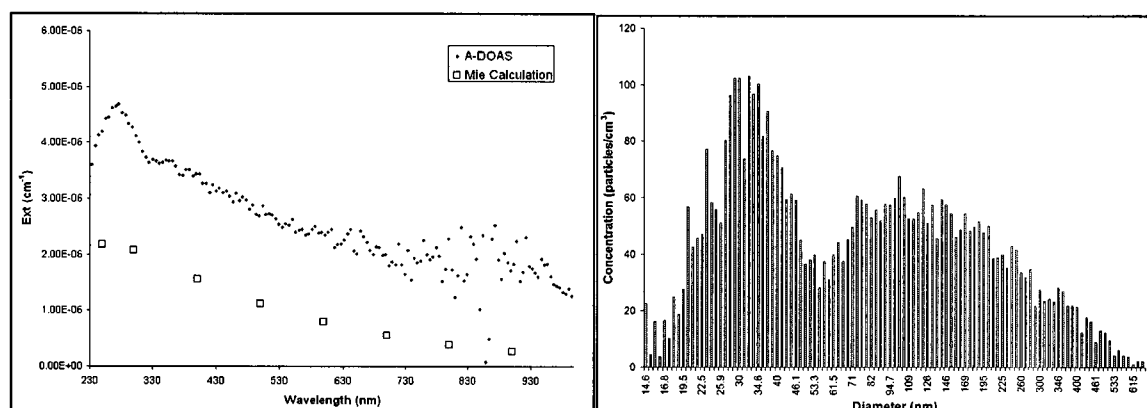
Figure 5.4. (A) The experimentally determined aerosol extinction for June 01, 2010 is greater
than the aerosol extinction predicted by Mie theory (total concentration = 4500 particles/cm^3) by
more than a factor of two at most wavelengths. The measured particle size distribution, shown in
(B), was used to perform the Mie theory calculations.

A-DOAS measurements recorded on June 03, 2010 no longer display a two-fold

underestimation of aerosol extinction by Mie theory at all wavelengths. However, Mie

theory does underestimate the experimental aerosol extinction by approximately three-

fold at wavelengths near 240 nm, as seen in Figure 5.5. The experimental aerosol

extinction is less than the A-DOAS detection limit (not shown) at wavelengths greater

than 420 nm, and cannot be compared to the Mie theory calculation. The rapid increase

of the measured extinction in the UV could be indicative of oxidized aerosols (Myhre and

Nielsen 2004; Kroll, Ng et al. 2005; Barsanti and Pankow 2006). The oxidation of volatile carbon compounds to carboxylic and dicarboxylic acids can lower the vapor pressure of the gas, allowing it to condense onto existing particles. These condensed species typically have a non-zero extinction coefficient, which increases at shorter wavelengths (Myhre and Nielsen 2004). The condensed oxidize material will change the complex refractive index of the particles thus altering its optical properties. These types of chemical changes have been shown to increase UV absorption of aerosols relative to purely scattering aerosols (Myhre and Nielsen 2004; Kanakidou, Seinfeld et al. 2005; Poschl 2005).
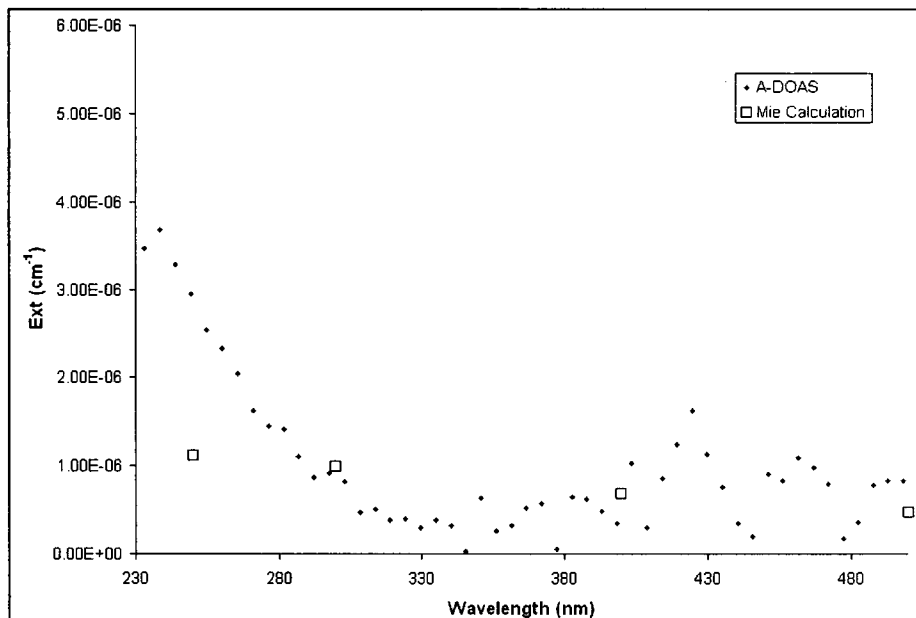
Figure 5.5. The A-DOAS measured extinction of an aerosol sample on June 03, 2010 shows extinction values below the A-DOAS detection limit, except for wavelengths less than approximately 420 nm. For clarity, the figure is truncated at 500 nm.

An extinction comparison, similar to the one performed in Chapter 4 with dry and humidified nigrosin, was completed to quantify differences between aerosol samples thought to be influenced by forest fire smoke or other strongly absorbing species, and those thought to have no forest fire influence. Figure 5.6 shows the extinction per total aerosol cross sectional area for particles influenced by smoke (black – June 1) and particles not influenced by smoke (gray – June 3). It is clear that the aerosol sample

measured on June 1 attenuates more light per total aerosol cross sectional area than the ambient aerosol sample measured on June 3. This is likely due to a large absorption component corresponding to smoke transported from the Canadian forest fires. Both the "Influenced by smoke" and "Not influenced by smoke" data shown in Figure 5.6 are the average of three measurements taken during the same experimental trial.
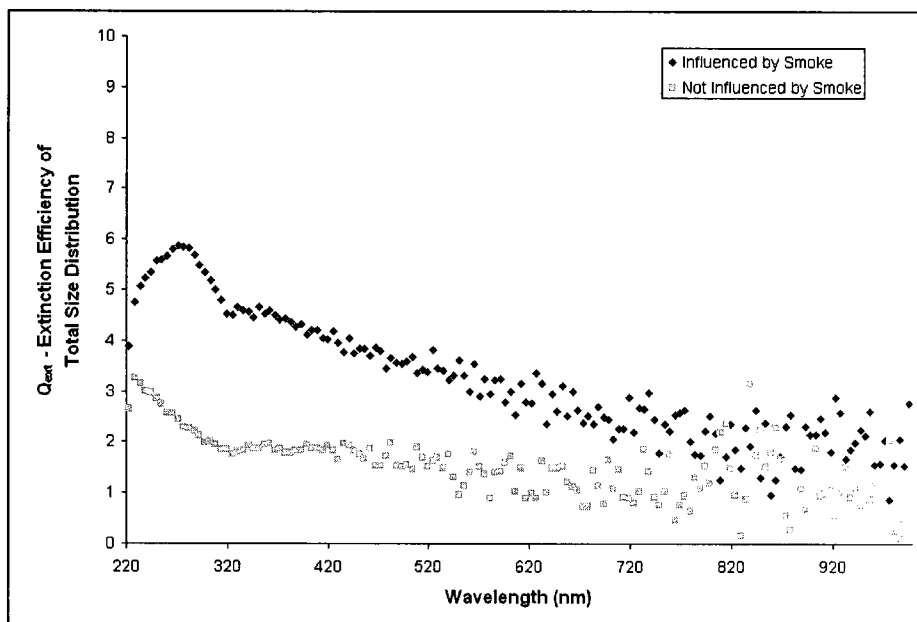
Figure 5.6. The aerosol sample influenced by the Canadian forest fire smoke or other highly absorbing aerosol attenuates approximately twice as much light per total cross sectional area as an aerosol sample measured under clean conditions. Both sets of data are the average of three measurements from the same trial.

The preliminary work in this chapter shows that the A-DOAS is capable of experimentally measuring the extinction of ambient aerosols, especially at wavelengths in the UV to blue spectral range. Some aspects of the chemical composition of the aerosol samples measured in this work can be inferred from the extinction spectra and back trajectories, but coupling these data with chemical composition measurements would help correlate the observed extinction features with specific atmospheric processes. The magnitude of aerosol extinction is largely dependent upon particle size and concentration, meaning that days with high particle concentrations and/or a greater number of large particles will provide more useful extinction data (above the A-DOAS

detection limit) than days with low concentrations. Measured aerosol extinction during rare events, like smoke from forest fires in Canada, can provide invaluable information about the aging and transport processes of aerosols in the lower atmosphere, and effort should be made to use the A-DOAS to measure aerosol extinction during such events in the future.

Suggestions for Future Work

This work has shown that the A-DOAS is a versatile instrument capable of measuring the extinction of highly scattering aerosols (PSLs), highly absorbing aerosols (nigrosin and CB), and aerosol samples that may be a mixture of the two (ambient measurements). However, there are more experiments that can be done both in the laboratory and in the field with the A-DOAS that can contribute to the collective knowledge of the optical properties of atmospheric aerosols necessary to improve climate modeling.

Determination of Complex Refractive Indices. The A-DOAS data in this work (Chapters 3 and 4) may indicate that experimental measurements of size selected aerosols can be used to determine the wavelength dependent complex refractive indices for an aerosol sample. The wavelength dependent complex refractive index for a specific type of aerosol is crucial to determining how the aerosol sample will interact with sunlight and affect the climate. Size selecting aerosol samples in the lab (e.g. mineral dust, sea salt, humic like substances) and measuring the extinction of these aerosols can provide complex refractive index information that is not readily available to the aerosol community for many types of aerosols. There are techniques (e.g. CRD-AES) that can do this at discrete wavelengths, but the A-DOAS is capable of making these measurements at a continuum of wavelengths comparable to the solar spectrum. Aerosols with large uncertainties associated with their optical properties should be targeted for these laboratory experiments with the A-DOAS.

A related area that should be addressed is the creation of a Mie fitting routine that is able to iteratively calculate the best fit complex refractive index for experimentally measured extinction efficiency versus particle size data. This will improve the accuracy of finding the complex refractive index for experimental data in comparison to the time involved in sampling a variety of complex refractive index values to find the best visual fit, as was done in this work.

Measurement of Nigrosin and Carbon Black. Experiments measuring the extinction of size selected nigrosin should be repeated. This experiment was only performed once and should be repeated multiple times to assess the repeatability of A-DOAS experiments with highly absorbing aerosols. The complex refractive index at multiple wavelengths should be determined with a computer program and compared to both previous literature values and solution phase UV-Vis measurements. Nigrosin samples differ with manufacturer so a consistent sample should be used.

The carbon black data discussed in Chapter 4 of this work contained a pressure peak interference that rendered the extinction data at wavelengths less than 500 nm unusable. This experiment should be repeated with a controlled setup that minimizes variations in flow rate. Further, this should be performed without an impactor on the inlet of the DMA, as it was discovered after this experiment that the buildup of particulate matter on the impactor, when using high aerosol concentrations, can affect the flow rates over the course of an experiment. The impinger setup should also be re-examined. There may be a better way to disperse the CB, such as by placing a funnel on the bottom to concentrate the CB in a small area, or by further reducing the diameter of tubing used to increase the velocity of the nitrogen.

Field Studies. A-DOAS measurements of ambient aerosol extinction would benefit from simultaneous measurements of the chemical composition of the aerosol sample. This could be accomplished by collecting aerosol samples on filters, extracting

108

the residue from the filter, and analyzing it using and combination of a number of techniques (e.g. FT-IR, ion chromatography, NMR, solution phase UV-Vis). The chemical information could then be compared to the extinction data and possible chemical contributions to extinction correlated.

It would also be advantageous to make comparisons between the A-DOAS extinction data and measurements of gas phase oxidants. Species such as ozone and hydroxyl radicals oxidize organic species allowing them to condense into the particle phase, increasing extinction in the UV. Analyzing changes in the measured extinction at UV wavelengths, in conjunction with oxidant concentration data, could provide information on the processes that are occurring in the atmosphere on local and regional scales. This analysis could also be performed with meteorological data such as relative humidity or precipitation rates. Aerosols tend to grow as relative humidity increases and it is expected that the A-DOAS would see changes in extinction corresponding to RH changes, as was seen in Chapter 4 with nigrosin. Rain will remove aerosols from the atmosphere and it would be interesting to monitor a decrease in aerosol extinction during a rain storm.

The A-DOAS instrument may provide more valuable extinction information in an urban area than in a rural setting. Many of the aerosol extinction measurements made in Durham, NH were near the detection limit of the A-DOAS. Urban environments are more polluted, with a greater number of soot sources, which would increase the measured aerosol extinction. It is possible that a distinct daily pattern of aerosol extinction would emerge, which may correspond to rush hour traffic or similar expected daily variability. There would also be increase concentration of absorbing gas phase species in a city so care would have to be taken to minimize their effect by recording frequent zeros or otherwise monitoring their interferences.

Chamber Studies. The A-DOAS instrument would be ideal to use in a laboratory setting with a smog chamber, as it could monitor changes in extinction over time as conditions such as precursor and oxidant concentrations were varied. The detection limit of the A-DOAS is low enough that atmospherically relevant concentrations of aerosols could be used, which is not possible with other similar techniques (Chapter 1). The A-DOAS would be especially useful for measuring the extinction of soot in chamber studies. If the soot could be size selected, and Mie theory for aggregate particles used, it would be possible to estimate the complex refractive index of the soot and then attribute it to the specific combustion source and conditions. This signature could then be applied to ambient measurements.

Comparison to CRD-AES Measurements. Aerosol extinction determined experimentally with the A-DOAS should be compared to extinction measurements made with the CRD-AES for the same aerosol sample. The CRD-AES is currently used to measure aerosol extinction at 532 nm, but it also has the ability in the future to measure extinction at 355 nm and 1064 nm, while the A-DOAS can measure extinction from approximately 220-1050 nm. An experiment should be performed where the A-DOAS and CRD-AES sample the same laboratory generated or ambient aerosols, and the experimental data at corresponding wavelengths should be compared. If the two techniques demonstrate they measure comparable aerosol extinction at the similar wavelengths then the validity of future measurements will be strengthened. While not expected, if the results the A-DOAS and CRD-AES used in the experiment are not comparable, then additional experiments should be performed to address the reasons as to why this is, which could lead to new information about the operation of the A-DOAS.

LIST OF REFERENCES

Anderson, T. L., D. S. Covert, et al. (1996). "Performance characteristics of a high-sensitivity, three-wavelength, total scatter/backscatter nephelometer." *Journal of Atmospheric and Oceanic Technology* **13**(5): 967-986.

Andreae, M. O. and A. Gelencser (2006). "Black carbon or brown carbon? The nature of light-absorbing carbonaceous aerosols." *Atmospheric Chemistry and Physics* **6**: 3131-3148.

Andreae, M. O., O. Schmid, et al. (2008). "Optical properties and chemical composition of the atmospheric aerosol in urban Guangzhou, China." *Atmospheric Environment* **42**(25): 6335-6350.

Armerding, W., M. Spiekermann, et al. (1992). "Fast scanning laser DOAS for local monitoring of trace gases, in particular tropospheric OH radicals." *Berichte Der Bunsen-Gesellschaft-Physical Chemistry Chemical Physics* **96**(3): 314-318.

Arnott, W. P., H. Moosmuller, et al. (1999). "Photoacoustic spectrometer for measuring light absorption by aerosol: instrument description." *Atmospheric Environment* **33**(17): 2845-2852.

Arnott, W. P., H. Moosmuller, et al. (2003). "Photoacoustic and filter-based ambient aerosol light absorption measurements: Instrument comparisons and the role of relative humidity." *Journal of Geophysical Research-Atmospheres* **108**(D1): 11.

Arnott, W. P., H. Moosmuller, et al. (2000). "Nitrogen dioxide and kerosene-flame soot calibration of photoacoustic instruments for measurement of light absorption by aerosols." *Review of Scientific Instruments* **71**(12): 4545-4552.

Atkinson, R. (2000). "Atmospheric chemistry of VOCs and NO_x." *Atmospheric Environment* **34**(12-14): 2063-2101.

Barnard, J. C., R. Volkamer, et al. (2008). "Estimation of the mass absorption cross section of the organic carbon component of aerosols in the Mexico City Metropolitan Area." *Atmospheric Chemistry and Physics* **8**(22): 6665-6679.

Barsanti, K. C. and J. F. Pankow (2006). "Thermodynamics of the formation of atmospheric organic particulate matter by accretion reactions - Part 3: Carboxylic and dicarboxylic acids." *Atmospheric Environment* **40**(34): 6676-6686.

Baynard, T., E. R. Lovejoy, et al. (2007). "Design and application of a pulsed cavity ring-down aerosol extinction spectrometer for field measurements." *Aerosol Science and Technology* **41**(4): 447-462.

Bennett, H. S. and R. A. Forman (1977). "Frequency-dependence of photoacoustic spectroscopy - absorption and bulk-absorption coefficients." *Journal of Applied Physics* **48**(4): 1432-1436.

Bertocchi, R., A. Kribus, et al. (2004). "Experimentally determined optical properties of a polydisperse carbon black cloud for a solar particle receiver." *Journal of Solar Energy Engineering-Transactions of the Asme* **126**(3): 833-841.

Bogumil, K., J. Orphal, et al. (2003). "Measurements of molecular absorption spectra with the SCIAMACHY pre-flight model: instrument characterization and reference data for atmospheric remote-sensing in the 230-2380 nm region." *Journal of Photochemistry and Photobiology a-Chemistry* **157**(2-3): 167-184.

Bohren, C.F., and Huffman, D.K., (1983), "Absorption and Scattering of Light by Small Particles." Wiley, New York

Bond, T. C., T. L. Anderson, et al. (1999). "Calibration and intercomparison of filter-based measurements of visible light absorption by aerosols." *Aerosol Science and Technology* **30**(6): 582-600.

Bond, T. C. and R. W. Bergstrom (2006). "Light absorption by carbonaceous particles: An investigative review." *Aerosol Science and Technology* **40**(1): 27-67.

Bond, T. C., G. Habib, et al. (2006). "Limitations in the enhancement of visible light absorption due to mixing state." *Journal of Geophysical Research-Atmospheres* **111**(D20): 13.

Brauers, T., U. Aschmutat, et al. (1996). "Intercomparison of tropospheric OH radical measurements by multiple folded long-path laser absorption and laser induced fluorescence." *Geophysical Research Letters* **23**(18): 2545-2548.

Buchwitz, M., V. V. Rozanov, et al. (2000). "A near-infrared optimized DOAS method for the fast global retrieval of atmospheric CH_4, CO, CO_2, H_2O, and N_2O total column amounts from SCIAMACHY Envisat-1 nadir radiances." *Journal of Geophysical Research-Atmospheres* **105**(D12): 15231-15245.

Cai, Y., A. Zelenyuk, et al. (2006). "A high resolution study of the effect of morphology on the mass spectra of single PSL particles with Na-containing layers and nodules." *Aerosol Science and Technology* **40**(12): 1111-1122.

Cappa, C. D., D. A. Lack, et al. (2008). "Bias in filter-based aerosol light absorption measurements due to organic aerosol loading: Evidence from laboratory measurements." *Aerosol Science and Technology* **42**(12): 1022-1032.

Cataldo, F. (2002). "An investigation on the optical properties of carbon black, fullerite, and other carbonaceous materials in relation to the spectrum of interstellar extinction of light." *Fullerenes Nanotubes and Carbon Nanostructures* **10**(2): 155-170.

Charlson, R. J., S. E. Schwartz, et al. (1992). "Climate forcing by anthropogenic aerosols." *Science* **255**(5043): 423-430.

Clarke, A., C. McNaughton, et al. (2007). "Biomass burning and pollution aerosol over North America: Organic components and their influence on spectral optical properties and humidification response." *Journal of Geophysical Research-Atmospheres* **112**(D12): 13.

Coheur, P. F., S. Fally, et al. (2002). "New water vapor line parameters in the 26000-13000 cm(-1) region." *Journal of Quantitative Spectroscopy & Radiative Transfer* **74**(4): 493-510.

Cornu, A. (1879). "Observation de la limite ultraviolette du spectre solaire a diverses altitudes." C.R. Academy of Sciences, **89**, 808

Daimon, M. and A. Masumura (2007). "Measurement of the refractive index of distilled water from the near-infrared region to the ultraviolet region." *Applied Optics* **46**(18): 3811-3820.

de Gouw, J. A., A. M. Middlebrook, et al. (2005). "Budget of organic carbon in a polluted atmosphere: Results from the New England Air Quality Study in 2002." *Journal of Geophysical Research-Atmospheres* **110**(D16): 22.

DeCarlo, P. F., J. G. Slowik, et al. (2004). "Particle morphology and density characterization by combined mobility and aerodynamic diameter measurements. Part 1: Theory." *Aerosol Science and Technology* **38**(12): 1185-1205.

Dinar, E., A. A. Riziq, et al. (2008). "The complex refractive index of atmospheric and model humic-like substances (HULIS) retrieved by a cavity ring down aerosol spectrometer (CRD-AS)." *Faraday Discussions* **137**: 279-295.

Doussin, J. F., D. Ritz, et al. (1997). "Design of an environmental chamber for the study of atmospheric chemistry: New developments in the analytical device." *Analusis* **25**(7): 236-242.

Fan, J. W., R. Y. Zhang, et al. (2008). "Effects of aerosol optical properties on deep convective clouds and radiative forcing." *Journal of Geophysical Research-Atmospheres* **113**(D8): 16.

Finlayson-Pitts, B.J., Pitts, J.N., (1999). "Chemistry of the Upper and Lower Atmosphere: Theory, Experiments, and Applications." Academic Press, New York.

Flores, J. M., M. Trainic, et al. (2009). "Effective broadband refractive index retrieval by a white light optical particle counter." *Phys Chem Chem Phys* **11**(36): 7943-50.

Frankenberg, C., U. Platt, et al. (2005). "Iterative maximum a posteriori (IMAP)-DOAS for retrieval of strongly absorbing trace gases: Model studies for CH_4 and CO_2 retrieval from near infrared spectra of SCIAMACHY onboard ENVISAT." *Atmospheric Chemistry and Physics* **5**: 9-22.

French, R. H., K. I. Winey, et al. (2007). "Optical properties and van der Waals-London dispersion interactions of polystyrene determined by vacuum ultraviolet spectroscopy and spectroscopic ellipsometry." *Australian Journal of Chemistry* **60**(4): 251-263.

Frins, E., N. Bobrowski, et al. (2006). "Tornographic multiaxis-differential optical absorption spectroscopy observations of Sun-illuminated targets: a technique providing well-defined absorption paths in the boundary layer." *Applied Optics* **45**(24): 6227-6240.

Fuller, K. A., W. C. Malm, et al. (1999). "Effects of mixing on extinction by carbonaceous particles." *Journal of Geophysical Research-Atmospheres* **104**(D13): 15941-15954.

Galarneau, E., P. A. Makar, et al. (2007). "Estimation of atmospheric emissions of six semivolatile polycyclic aromatic hydrocarbons in southern Canada and the United States by use of an emissions processing system." *Environmental Science & Technology* **41**(12): 4205-4213.

Galli, M., S. A. Guazzotti, et al. (2001). "Improved lower particle size limit for aerosol time-of-flight mass spectrometry." *Aerosol Science and Technology* **34**(4): 381-385.

Garvey, D. M. and R. G. Pinnick (1983). "Response characteristics of the particle measuring systems active scattering aerosol spectrometer probe (ASASP-X)." *Aerosol Science and Technology* **2**(4): 477-488.

Gong, S. L., L. A. Barrie, et al. (2002). "Canadian Aerosol Module (CAM): A size-segregated simulation of atmospheric aerosol processes for climate and air quality models - 2. Global sea-salt aerosol and its budgets." *Journal of Geophysical Research-Atmospheres* **107**(D24): 14.

Grieshop, A. P., J. M. Logue, et al. (2009). "Laboratory investigation of photochemical oxidation of organic aerosol from wood fires 1: measurement and simulation of organic aerosol evolution." *Atmospheric Chemistry and Physics* **9**(4): 1263-1277.

Hansen, J., M. Sato, et al. (1997). "Radiative forcing and climate response." *Journal of Geophysical Research-Atmospheres* **102**(D6): 6831-6864.

Hartley, W.N., (1881). "On the absorption spectrum of ozone." *J. Chem. Soc.*, **39**, 57-60

Haywood, J. M. and K. P. Shine (1995). "The effect of anthropogenic sulfate and soot aerosol on the clear-sky planetary radiation budget." *Geophysical Research Letters* **22**(5): 603-606.

Heland, J., J. Kleffmann, et al. (2001). "A new instrument to measure gaseous nitrous acid (HONO) in the atmosphere." *Environmental Science & Technology* **35**(15): 3207-3212.

Honninger, G., C. von Friedeburg, et al. (2004). "Multi axis differential optical absorption spectroscopy (MAX-DOAS)." *Atmospheric Chemistry and Physics* **4**: 231-254.

Horowitz, A., R. Meller, et al. (2001). "The UV-VIS absorption cross sections of the alpha-dicarbonyl compounds: Pyruvic acid, biacetyl and glyoxal." *Journal of Photochemistry and Photobiology a-Chemistry* **146**(1-2): 19-27.

Horvath, H. (1993). "Atmospheric light-absorption - A review." *Atmospheric Environment Part a-General Topics* **27**(3): 293-317.

IPCC Fourth Assessment Report (2007), Solomon, S., D. Qin, M. Manning, Z. Chen, M. Marquis, K.B. Averyt, M. Tignor and H.L. Miller (eds.). "Contribution of Working Group I to the Fourth Assessment Report of the Intergovernmental Panel on Climate Change, 2007. Cambridge University Press, Cambridge, United Kingdom and New York, NY

Jacob, D. J. (1999). "Introduction to Atmospheric Chemistry." Princeton University Press, Princeton, NJ

Jacob, D. J. (2000). "Heterogeneous chemistry and tropospheric ozone." *Atmospheric Environment* **34**(12-14): 2131-2159.

Jacobson, M. Z. (2001). "Strong radiative heating due to the mixing state of black carbon in atmospheric aerosols." *Nature* **409**(6821): 695-697.

Jaenicke, R. (2005). "Abundance of cellular material and proteins in the atmosphere." *Science* **308**(5718): 73-73.

Janzen, J. (1979). "Refractive index of colloidal carbon." *Journal of Colloid and Interface Science* **69**(3): 436-447.

Jayaraman, A., M. V. Ratnam, et al. (2010). "Study of Atmospheric Forcing and Responses (SAFAR) campaign: overview." *Annales Geophysicae* **28**(1): 89-101.

Jimenez, J. L., M. R. Canagaratna, et al. (2009). "Evolution of Organic Aerosols in the Atmosphere." *Science* **326**(5959): 1525-1529.

Joblin, C., A. Leger, et al. (1992). "Contribution of polycyclic aromatic hydrocarbon molecules to the interstellar extinction curve." *Astrophysical Journal* **393**(2): L79-L82.

Kanakidou, M., J. H. Seinfeld, et al. (2005). "Organic aerosol and global climate modelling: a review." *Atmospheric Chemistry and Physics* **5**: 1053-1123.

Khalizov, A. F., H. X. Xue, et al. (2009). "Enhanced Light Absorption and Scattering by Carbon Soot Aerosol Internally Mixed with Sulfuric Acid." *Journal of Physical Chemistry A* **113**(6): 1066-1074.

Kim, E. J., J. E. Oh, et al. (2003). "Effects of forest fire on the level and distribution of PCDD/Fs and PAHs in soil." *Science of the Total Environment* **311**(1-3): 177-189.

Kiehl, J. T., and H. Rodhe (1995). "Modeling geographical and seasonal forcing due to aerosols." *Aerosol Forcing of Climate*, R. J. Charlson and J. Heintzenberg, Eds., John Wiley.

Kotzick, R., U. Panne, et al. (1997). "Changes in condensation properties of ultrafine carbon particles subjected to oxidation by ozone." *Journal of Aerosol Science* **28**(5): 725-735.

Kroll, J. H., N. L. Ng, et al. (2005). "Chamber studies of secondary organic aerosol growth by reactive uptake of simple carbonyl compounds." *Journal of Geophysical Research-Atmospheres* **110**(D23): 10.

Kuang, Z. M. and Y. L. Yung (2000). "Reflectivity variations off the Peru Coast: Evidence for indirect effect of anthropogenic sulfate aerosols on clouds." *Geophysical Research Letters* **27**(16): 2501-2504.

Kulmala, M., H. Vehkamäki, et al. (2004). "Formation and growth rates of ultrafine atmospheric particles: a review of observations." *Journal of Aerosol Science* **35**(2): 143-176.

Lack, D. A. and C. D. Cappa (2010). "Impact of brown and clear carbon on light absorption enhancement, single scatter albedo and absorption wavelength dependence of black carbon." *Atmospheric Chemistry and Physics* **10**(9): 4207-4220.

Lack, D. A., C. D. Cappa, et al. (2009). "Absorption Enhancement of Coated Absorbing Aerosols: Validation of the Photo-Acoustic Technique for Measuring the Enhancement." *Aerosol Science and Technology* **43**(10): 1006-1012.

Lack, D. A., E. R. Lovejoy, et al. (2006). "Aerosol absorption measurement using photoacoustic spectroscopy: Sensitivity, calibration, and uncertainty developments." *Aerosol Science and Technology* **40**(9): 697-708.

Lang-Yona, M., Y. Rudich, et al. (2009). "Complex Refractive Indices of Aerosols Retrieved by Continuous Wave-Cavity Ring Down Aerosol Spectrometer." *Analytical Chemistry* **81**(5): 1762-1769.

Lang-Yona, N., A. Abo-Riziq, et al. (2010). "Interaction of internally mixed aerosols with light." *Physical Chemistry Chemical Physics* **12**(1): 21-31.

Langridge, J. M., S. M. Ball, et al. (2006). "A compact broadband cavity enhanced absorption spectrometer for detection of atmospheric NO_2 using light emitting diodes." *Analyst* **131**(8): 916-922.

Li, X., T. Brauers, et al. (2010). "MAX-DOAS measurements in southern China: retrieval of aerosol extinctions and validation using ground-based in-situ data." *Atmospheric Chemistry and Physics* **10**(5): 2079-2089.

Liu, B. Y. H. and K. W. Lee (1975). "Aerosol generator of high stability." *American Industrial Hygiene Association Journal* **36**(12): 861-865.

Liu, B. Y. H., F. J. Romay, et al. (2010). "A Wide-Range Particle Spectrometer for Aerosol Measurement from 0.010 mu m to 10 mu m." *Aerosol and Air Quality Research* **10**(2): 125-139.

Lopes, W. A. and J. B. deAndrade (1996). "Sources, formation, reactivity and quantification of polycyclic aromatic hydrocarbons (PAH) in atmosphere." *Quimica Nova* **19**(5): 497-516.

Ma, X. Y., J. Q. Lu, et al. (2003). "Determination of complex refractive index of polystyrene microspheres from 370 to 1610 nm." *Physics in Medicine and Biology* **48**(24): 4165-4172.

Mallet, M., P. Tulet, et al. (2009). "Impact of dust aerosols on the radiative budget, surface heat fluxes, heating rate profiles and convective activity over West Africa during March 2006." *Atmospheric Chemistry and Physics* **9**(18): 7143-7160.

Massoli, P., D. M. Murphy, et al. (2009). "Uncertainty in Light Scattering Measurements by TSI Nephelometer: Results from Laboratory Studies and Implications for Ambient Measurements." *Aerosol Science and Technology* **42**(11): 1064-1074.

Mätzler, Christian, (2002a). "MATLAB Functions for Mie Scattering and Absorption." Research Report (No. 2002-08), Institut für Angewandte Physik.

Mätzler, Christian, (2002b). "MATLAB Functions for Mie Scattering and Absorption - Version 2." Research Report (No. 2002-11), Institut für Angewandte Physik.

McMurry, P. H. (2000). "A review of atmospheric aerosol measurements." *Atmospheric Environment* **34**(12-14): 1959-1999.

Meinen, J., J. Thieser, et al. (2010). "Technical Note: Using a high finesse optical resonator to provide a long light path for differential optical absorption spectroscopy: CE-DOAS." *Atmospheric Chemistry and Physics* **10**(8): 3901-3914.

Meyrahn, H., J. Pauly, et al. (1986). "Quantum yields for the photodissociation of acetone in air and an estimate for the life time of acetone in the lower atmosphere." *Journal of Atmospheric Chemistry* **4**(2): 277-291.

Mogili, P. K., K. H. Yang, et al. (2007). "Environmental aerosol chamber studies of extinction spectra of mineral dust aerosol components: Broadband IR-UV extinction spectra." *Journal of Geophysical Research-Atmospheres* **112**(D21): 12.

Moosmuller, H. and W. P. Arnott (2003). "Angular truncation errors in integrating nephelometry." *Review of Scientific Instruments* **74**(7): 3492-3501.

Moosmuller, H., W. P. Arnott, et al. (1998). "Photoacoustic and filter measurements related to aerosol light absorption during the Northern Front Range Air Quality Study (Colorado 1996/1997)." *Journal of Geophysical Research-Atmospheres* **103**(D21): 28149-28157.

Moosmuller, H., R. K. Chakrabarty, et al. (2009). "Aerosol light absorption and its measurement: A review." *Journal of Quantitative Spectroscopy & Radiative Transfer* **110**(11): 844-878.

Muller, T., D. Muller, et al. (2005). "Particle extinction measured at ambient conditions with differential optical absorption spectroscopy. 1. System setup and characterization." *Applied Optics* **44**(9): 1657-1666.

Murphy, D. M. (2009). "The Effect of Water Evaporation on Photoacoustic Signals in Transition and Molecular Flow." *Aerosol Science and Technology* **43**(4): 356-363.

Myhre, C. E. L. and C. J. Nielsen (2004). "Optical properties in the UV and visible spectral region of organic acids relevant to tropospheric aerosols." *Atmospheric Chemistry and Physics* **4**: 1759-1769.

Najera, J. J., J. G. Fochesatto, et al. (2008). "Infrared spectroscopic methods for the study of aerosol particles using White cell optics: Development and characterization of a new aerosol flow tube." *Review of Scientific Instruments* **79**(12): 12.

Nenes, A., W. C. Conant, et al. (2002). "Black carbon radiative heating effects on cloud microphysics and implications for the aerosol indirect effect - 2. Cloud microphysics." *Journal of Geophysical Research-Atmospheres* **107**(D21): 11.

Nikolov, I. D. and C. D. Ivanov (2000). "Optical plastic refractive measurements in the visible and the near-infrared regions." *Applied Optics* **39**(13): 2067-2070.

Notholt, J., J. Hjorth, et al. (1992). "Formation of HNO₂ on aerosol surfaces during foggy periods in the presence of NO and NO₂." *Atmospheric Environment Part a-General Topics* **26**(2): 211-217.

Park, R. J., M. J. Kim, et al. (2010). "A contribution of brown carbon aerosol to the aerosol light absorption and its radiative forcing in East Asia." *Atmospheric Environment* **44**(11): 1414-1421.

Pavia, D.L., Lampman, G.M., Kriz, G.S., (2001). "Introduction to Spectroscopy." Brooks/Cole, Belmont, CA

Penner, J. E., D. Hegg, et al. (2001). "Unraveling the role of aerosols in climate change." *Environmental Science & Technology* **35**(15): 332A-340A.

Peters, C., S. Pechtl, et al. (2005). "Reactive and organic halogen species in three different European coastal environments." *Atmospheric Chemistry and Physics* **5**: 3357-3375.

Pettersson, A., E. R. Lovejoy, et al. (2004). "Measurement of aerosol optical extinction at 532nm with pulsed cavity ring down spectroscopy." *Journal of Aerosol Science* **35**(8): 995-1011.

Pfeilsticker, K., H. Bosch, et al. (2001). "First atmospheric profile measurements of UV/visible O-4 absorption band intensities: Implications for the spectroscopy, and the formation enthalpy of the O₂-O₂ dimer." *Geophysical Research Letters* **28**(24): 4595-4598.

Platt, U. (1999). "Modern methods of the measurement of atmospheric trace gases." *Physical Chemistry Chemical Physics* **1**(24): 5409-5415.

Platt, U. and M. Hausmann (1994). "Spectroscopic measurement of the free-radials NO₃, BrO, IO, and OH in the troposphere." *Research on Chemical Intermediates* **20**(3-5): 557-578.

Platt, U., Stutz, J., (2008). "Differential Optical Absorption Spectroscopy: Principles and Applications." Springer, New York.

Poschl, U. (2005). "Atmospheric aerosols: Composition, transformation, climate and health effects." *Angewandte Chemie-International Edition* **44**(46): 7520-7540.

Quinten, M., U. Kreibig, et al. (2002). "Wavelength-dependent optical extinction of carbonaceous particles in atmospheric aerosols and interstellar dust." *Applied Optics* **41**(33): 7102-7113.

Ramanathan, V. and G. Carmichael (2008). "Global and regional climate changes due to black carbon." *Nature Geoscience* **1**(4): 221-227.

Riziq, A. A., C. Erlick, et al. (2007). "Optical properties of absorbing and non-absorbing aerosols retrieved by cavity ring down (CRD) spectroscopy." *Atmospheric Chemistry and Physics* **7**(6): 1523-1536.

Rompp, A., R. Winterhalter, et al. (2006). "Oxodicarboxylic acids in atmospheric aerosol particles." *Atmospheric Environment* **40**(35): 6846-6862.

Saathoff, H., K. H. Naumann, et al. (2003). "Coating of soot and (NH₄)₂SO₄ particles by ozonolysis products of alpha-pinene." *Journal of Aerosol Science* **34**(10): 1297-1321.

Saiz-Lopez, A., J. M. C. Plane, et al. (2004). "Bromine oxide in the mid-latitude marine boundary layer." *Geophysical Research Letters* **31**(3): 4.

Schnaiter, M., H. Horvath, et al. (2003). "UV-VIS-NIR spectral optical properties of soot and soot-containing aerosols." *Journal of Aerosol Science* **34**(10): 1421-1444.

Schnaiter, M., C. Linke, et al. (2005). "Absorption amplification of black carbon internally mixed with secondary organic aerosol." *Journal of Geophysical Research-Atmospheres* **110**(D19): 11.

Schnaiter, M., O. Schmid, et al. (2005). "Measurement of wavelength-resolved light absorption by aerosols utilizing a UV-VIS extinction cell." *Aerosol Science and Technology* **39**(3): 249-260.

Seinfeld, J.H., and Pandis, S.N., (2006). "Atmospheric Chemistry and Physics - From Air Pollution to Climate Change." (2nd edition) Wiley, New York

Sempere, R. and K. Kawamura (2003). "Trans-hemispheric contribution of C-2-C-10 alpha, omega-dicarboxylic acids, and related polar compounds to water-soluble organic carbon in the western Pacific aerosols in relation to photochemical oxidation reactions." *Global Biogeochemical Cycles* **17**(2): 15.

Sheridan, P. J., W. P. Arnott, et al. (2005). "The Reno Aerosol Optics Study: An evaluation of aerosol absorption measurement methods." *Aerosol Science and Technology* **39**(1): 1-16.

Shiraiwa, M., Y. Kondo, et al. (2010). "Amplification of Light Absorption of Black Carbon by Organic Coating." *Aerosol Science and Technology* **44**(1): 46-54.

Si, F. Q., P. H. Xie, et al. (2010). "Determination of the atmospheric aerosol optical density by multi axis differential optical absorption spectroscopy." *Acta Physica Sinica* **59**(4): 2867-2872.

Slowik, J. G., E. S. Cross, et al. (2007). "An inter-comparison of instruments measuring black carbon content of soot particles." *Aerosol Science and Technology* **41**(3): 295-314.

Slowik, J. G., K. Stainken, et al. (2004). "Particle morphology and density characterization by combined mobility and aerodynamic diameter measurements. Part 2: Application to combustion-generated soot aerosols as a function of fuel equivalence ratio." *Aerosol Science and Technology* **38**(12): 1206-1222.

Smith, J. D. and D. B. Atkinson (2001). "A portable pulsed cavity ring-down transmissometer for measurement of the optical extinction of the atmospheric aerosol." *Analyst* **126**(8): 1216-1220.

Smith, N., J. M. C. Plane, et al. (1995). "Nighttime radical chemistry in the San-Joaquin valley." *Atmospheric Environment* **29**(21): 2887-2897.

Spindler, C., A. A. Riziq, et al. (2007). "Retrieval of aerosol complex refractive index by combining cavity ring down aerosol spectrometer measurements with full size distribution information." *Aerosol Science and Technology* **41**(11): 1011-1017.

Strawa, A. W., R. Castaneda, et al. (2003). "The measurement of aerosol optical properties using continuous wave cavity ring-down techniques." *Journal of Atmospheric and Oceanic Technology* **20**(4): 454-465.

Sun, H. L., L. Biedermann, et al. (2007). "Color of brown carbon: A model for ultraviolet and visible light absorption by organic carbon aerosol." *Geophysical Research Letters* **34**(17): 5.

Swietlicki, E., S. Puri, et al. (1996). "Urban air pollution source apportionment using a combination of aerosol and gas monitoring techniques." *Atmospheric Environment* **30**(15): 2795-2809.

Taha, G., G. P. Box, et al. (2007). "Black carbon measurement using laser integrating plate method." *Aerosol Science and Technology* **41**(3): 266-276.

Takashima, H., H. Irie, et al. (2009). "Atmospheric aerosol variations at Okinawa Island in Japan observed by MAX-DOAS using a new cloud-screening method." *Journal of Geophysical Research-Atmospheres* **114**: 10.

Turpin, B. J., P. Saxena, et al. (2000). "Measuring and simulating particulate organics in the atmosphere: problems and prospects." *Atmospheric Environment* **34**(18): 2983-3013.

Twomey, S. (1991). "AEROSOLS, CLOUDS AND RADIATION." *Atmospheric Environment Part a-General Topics* **25**(11): 2435-2442.

Varma, R. M., D. S. Venables, et al. (2009). "Long optical cavities for open-path monitoring of atmospheric trace gases and aerosol extinction." *Applied Optics* **48**(4): B159-B171.

Virkkula, A., N. C. Ahlquist, et al. (2005). "A three-wavelength optical extinction cell for measuring aerosol light extinction and its application to determining light absorption coefficient." *Aerosol Science and Technology* **39**(1): 52-67.

Voigt, S., J. Orphal, et al. (2001). "The temperature dependence (203-293 K) of the absorption cross sections of O_3 in the 230-850 nm region measured by Fourier-transform spectroscopy." *Journal of Photochemistry and Photobiology a-Chemistry* **143**(1): 1-9.

Volkamer, R., T. Etzkorn, et al. (1998). "Correction of the oxygen interference with UV spectroscopic (DOAS) measurements of monocyclic aromatic hydrocarbons in the atmosphere." *Atmospheric Environment* **32**(21): 3731-3747.

Volkamer, R., L. T. Molina, et al. (2005). "DOAS measurement of glyoxal as an indicator for fast VOC chemistry in urban air." *Geophysical Research Letters* **32**(8): 4.

Volkamer, R., U. Platt, et al. (2001). "Primary and secondary glyoxal formation from aromatics: Experimental evidence for the bicycloalkyl-radical pathway from benzene, toluene, and p-xylene." *Journal of Physical Chemistry A* **105**(33): 7865-7874.

Volkamer, R., J. L. Jimenez, et al. (2006). "Secondary organic aerosol formation from anthropogenic air pollution: Rapid and higher than expected." *Geophysical Research Letters* **33**(17): 4.

Wagner, T., B. Dix, et al. (2004). "MAX-DOAS O_4 measurements: A new technique to derive information on atmospheric aerosols - Principles and information content." *Journal of Geophysical Research-Atmospheres* **109**(D22): 21.

Wangberg, I., T. Etzkorn, et al. (1997). "Absolute determination of the temperature behavior of the $NO_2+NO_3+(M)<->N_2O_5+(M)$ equilibrium." *Journal of Physical Chemistry A* **101**(50): 9694-9698.

White, J. U. (1942). "Long Optical Paths of Large Aperture." *J. Opt. Soc. Am.* **32**(5): 285-285.

Yang, M., S. G. Howell, et al. (2009). "Attribution of aerosol light absorption to black carbon, brown carbon, and dust in China - interpretations of atmospheric measurements during EAST-AIRE." *Atmospheric Chemistry and Physics* **9**(6): 2035-2050.

Zender, C. S., H. S. Bian, et al. (2003). "Mineral Dust Entrainment and Deposition (DEAD) model: Description and 1990s dust climatology." *Journal of Geophysical Research-Atmospheres* **108**(D14): 19.

Zhang, L. M., S. L. Gong, et al. (2001). "A size-segregated particle dry deposition scheme for an atmospheric aerosol module." *Atmospheric Environment* **35**(3): 549-560.